STUDY ON MULTIPLE ANGLE POLARIMETRIC RADAR IMAGE

Takuma Watanabe

Doctoral Program in Electrical and Information Engineering
Graduate School of Science and Technology
Niigata University

Contents

List of Figures

List of Tables

Abstract

This thesis deals with the analysis of multiple angle polarimetric synthetic aperture radar (PolSAR) images in the sense that the radar acquires the data from multiple incidence angles as well as azimuthal angles. The radar images are known to have strong dependence on these angular parameters and target physical or geometric characteristics such as the dielectric properties, roughness, shape, orientation, and so forth. Therefore, the multiple angle observation and analysis are necessary to aid the understanding of the PolSAR images. We carry out multiple angle PolSAR observation under well-controlled conditions in an anechoic chamber, and several characteristics of the multiple angle PolSAR images are revealed.

The major contributions of this thesis are summarized as follows:

1. Experimental investigation on how soil moisture affects the polarimetric backscattering from forested terrain using the multiple angle measurement data.

2. Comparison of model-based polarimetric decomposition algorithms applied for PolSAR and tomographic SAR (TomoSAR) images.

3. Introduction of polarimetric concepts to circular synthetic aperture radar (CSAR) observation and image reconstruction.

In the first contribution, we examine the effects of soil moisture on the double-bounce scattering occurred between the ground surface and trunks. We conduct simple model experiments in an anechoic chamber, and show that the co-polarization ratio and phase difference can be used to estimate the moisture condition of forested terrain.

The second contribution is the comparison of model-based polarimetric decomposition algorithms which are used to decompose a mixture of several scattering mechanisms into some simple scattering components. Although a number of decomposition algorithms have been developed, the physical interpretation of the decomposed results are still under investigation. To

help the understanding of the decomposed results, we provide the qualitative comparison of these algorithms using the anechoic chamber measurement data. Also the introduction to the polarimetric decomposition schemes to TomoSAR data reveals the possibility of recovering the three-dimensional structure and scattering mechanisms of the observing targets.

The last contributions are related to CSAR image analysis. Apart from the conventional SAR systems which have a linear flight path, CSAR has a circular trajectory to acquire the scattering of the observing scene for high-resolution radar image reconstruction. The introduction of polarimetric concepts to CSAR data becomes challenging due to the diversity of the polarization basis. In this thesis, we deal with this problem by introducing polarization basis transformation to CSAR reconstruction algorithm. It is shown that the building structure can be recovered by this novel CSAR image reconstruction processing.

Acknowledgment

This dissertation is composed of my doctoral work at Niigata University. Many people helped me to fulfill my degree during the life at the laboratory.

First and foremost, I would like to express the deepest respect and appreciation to the committee chair Professor Hiroyoshi Yamada who guided and encouraged me throughout my doctoral work. I was often astonished by his outstanding ideas and knowledge which taught me what a research should be and moreover what a researcher should be. I remember when I was taking his electromagnetics course as an undergraduate student. I was surprised that this complex subject was taught by him clearly, and this interesting class was one of the main reasons to enter his laboratory. I was very happy to be a doctoral student under his guidance, and my memories in his laboratory is surely the treasure of my life.

I express my warm thanks to Professor Yoshio Yamaguchi for his precious comments on my research work. As he is recognized as a famous researcher in the polarimetric radar community, I had a lot of chance to meet various specialists in my research field, which broaden my knowledge and communication skills to be a successful researcher. Also his financial support made my experiments, conference presentation, and publishing success.

I should express my gratitude to Dr. Motofumi Arii at Mitsubishi Space Software, Co., Ltd. for his unlimited collaboration on many of my research work. The work related to soil moisture estimation presented in this thesis was started as a joint research with him. As a specialist in radar science, he gave me a lot of valuable advice related to radar polarimetry and guided me to successfully complete my doctoral work. Also I am respectful to his enthusiastic attitude toward his research work.

I would like to thank Professor Ryoichi Sato at the Faculty of Education. He gave me many comments as a specialist in electromagnetic theory. In addition, he told me the measurement techniques for dielectric properties of material, which was an important part of my laboratory

experiments.

I also would like to thank Professor Hirokazu Kobayashi at Osaka Institute of Technology, a former specially appointed professor at the Niigata University. As a professional in high frequency electromagnetic theory and radar engineering, he gave me many advice which broaden my horizons to understand the physics of electromagnetic wave and radar. I equally would like to thank Dr. Sang-Eun Park, a former assistant professor at Niigata University, who told me a lot of things related to not only the theory of electromagnetic modeling, but also my research itself. I am also thankful for the other committee members Associate Professor Kentaro Nishimori and Professor Keisuke Nakano for giving me valuable comments on my dissertation and final defense presentation.

A special thanks to Yasuo Fukushima and Toru Adachi, the technical staffs at the Faculty of Engineering, who developed several tools to lead my laboratory experiments success. Without their kind collaboration, many of my experiments would not be done successfully. I would like to extend my gratitude to Dr. George O'Neil, an Assistant Professor at the university, who kindly checked on my written English. His worthful comments as a specialist in linguistics polished my first peer-reviewed paper and conference papers. Also I was lucky to find and join his nice English classes.

Many thanks for the students at the laboratory who helped with my experiments and data analysis, and of course for all the students and staffs for providing me the comfortable research environment. Finally, I am grateful to my family for allowing me to study at the university and supporting my private life.

March 2015, TAKUMA WATANABE.

To my beloved parents Ryuichi and Mari Watanabe

and

in memory of Minori Kobayashi

Chapter 1

Introduction

Background

Retrieval of structure or physical parameters of the earth surface over wide area is one of the main interests in various areas of geophysics such as meteorology, hydrology, geodesy, and so on. For this purpose, remote sensing from an aircraft or satellite have been widely studied and utilized with several types of onboard sensors. One of the most widely used sensor is the *synthetic aperture radar* (SAR) which has been successfully demonstrated for the capability of the earth observation, being able to provide an all-weather day-and-night supply of the high-resolution images of the ground surface. With the introduction of the advanced signal processing algorithms as well as the operational concepts, SAR is expected to be a powerful tool to retrieve the earth environment or dynamics.

The measured quantity of the SAR is the backscattered wave from ground surface, which contains physical or geometric information of the targets. Unfortunately, the interpretation of the SAR images is not always straightforward. Though the backscattering coefficient measured by SAR has a certain relationship to the physical and geometric parameters of the targets, the diversity and interaction of these parameters result in the complex variation of the measured SAR images. Thus, the discrimination of such a complex phenomena into some simple scattering mechanisms is necessary to well understand SAR images. This can be achieved via utilizing additional information, namely, the polarization of electromagnetic wave. The technique which utilizes the polarization for SAR data analysis is called *radar polarimetry*, and such a SAR system is referred to as *polarimetric* synthetic aperture radar (PolSAR).

The other well-known extension of the SAR system is *interferometric* SAR (InSAR) or *tomo-*

graphic SAR (TomoSAR). The InSAR is used to recover the topographic information of terrain, and two independent SAR images at slightly different sensor locations for the same observation area are acquired for this purpose. The height information can be retrieved by interfering these SAR signals. The TomoSAR is an extension of InSAR in the sense that the acquisition is made at three or more sensor locations or flight paths. The high resolution volumetric imaging of the backscattering is possible by employing direction-of-arrival (DOA) estimation techniques for array antennas. Needless to say, the combination of radar polarimetry and interferometric or tomographic SAR is possible.

Although the many algorithms and operational concepts are developed, the actual application of the SAR data in practical situation is still limited, because of the lack of quantitative validation of the information derived from SAR image analysis. The SAR images depend on not only the physical parameters of the targets, but also the geometric parameters such as target orientation, radar incidence angle, flight path direction, and so forth. Thus, to quantitatively relate physical parameters to obtained SAR image, it is essential to validate the data extraction algorithms with various terrain and radar conditions. To do this, the SAR experiments under well-controlled situation is essential. The objective of this thesis is to establish the relationship between the physical and geometric parameters to observed SAR images by laboratory experiments. We carried out indoor and outdoor experiments using simplified terrain models for this purpose. The SAR measurements are made at multiple incidence and azimuthal angles, and it is revealed that the multiple angle measurements provide additional information for SAR image analysis.

The Thesis

This thesis is structured as shown in Figure 1.1. In Chapter 2, an introduction to SAR image formation algorithm based on wavefront reconstruction theory is given. Also we describe the experimental system used in this research. Chapter 3 describes the basic principles of polarimetric radar image processing, and the experimental results are presented. Chapter 4 gives an analysis of multiple angle SAR images. Using the multiple angle SAR images, we discuss the effects of moisture variation in forested areas, and show that a simple polarimetric parameter called co-polarization ratio can be used to infer the moisture variation of forested terrain. Chapter 5 gives a basic concept of tomographic SAR (TomoSAR) data processing, and we propose an application of polarimetric decomposition schemes to three-dimensional tomographic data. In Chapter 6, polarimetric CSAR image analysis is shown. In the CSAR system, the diversity of the polarization basis makes the image analysis challenging, however, this means that the image

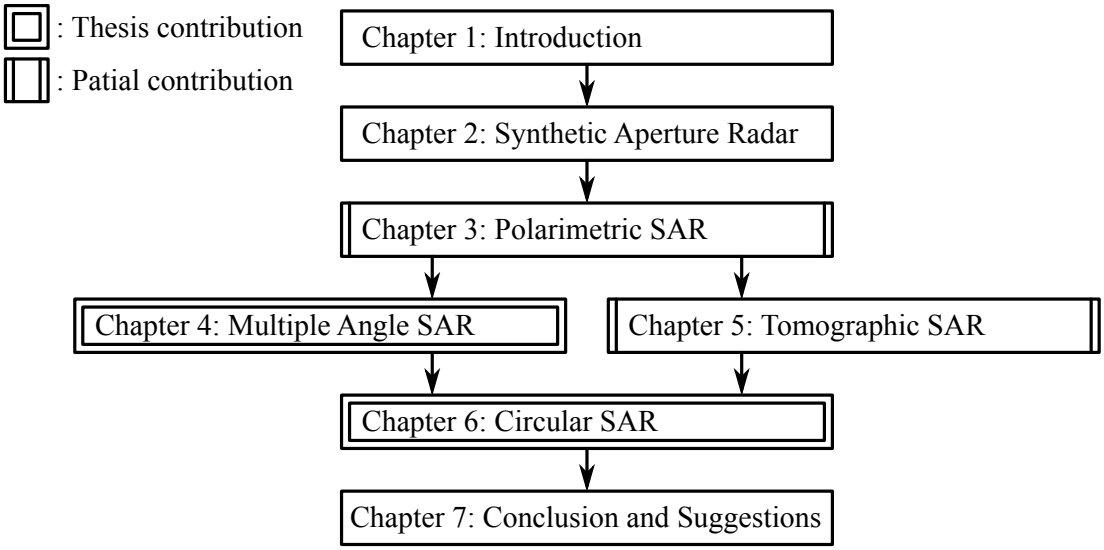

Figure 1.1: Thesis structure.

is expected to contains an additional information which does not exist in the conventional SAR images. Finally, Chapter 7 concludes the overall discussion and makes suggestion for further study.

The major contributions of this thesis are summarized as follows:

1. Experimental investigation on how soil moisture affects the polarimetric backscattering from forested terrain using the multiple angle measurement data.

2. Comparison of model-based polarimetric decomposition algorithms applied for PolSAR and tomographic SAR (TomoSAR) images.

3. Introduction of polarimetric concepts to circular synthetic aperture radar (CSAR) observation and image reconstruction.

In the first contribution, we examine the effects of soil moisture on the double-bounce scattering occurred between the ground surface and trunks. We conduct simple model experiments in an anechoic chamber, and show that the co-polarization ratio and phase difference can be used to estimate the moisture condition of forested terrain.

The second contribution is the comparison of model-based polarimetric decomposition algorithms which are used to decompose a mixture of several scattering mechanisms into some simple scattering components. Although a number of decomposition algorithms have been developed, the physical interpretation of the decomposed results are still under investigation. To

help the understanding of the decomposed results, we provide the qualitative comparison of these algorithms using the anechoic chamber measurement data. Also the introduction to the polarimetric decomposition schemes to TomoSAR data reveals the possibility of recovering the three-dimensional structure and scattering mechanisms of the observing targets.

The last contributions are related to CSAR image analysis. Apart from the conventional SAR systems which have a linear flight path, CSAR has a circular trajectory to acquire the scattering of the observing scene for high-resolution radar image reconstruction. The introduction of polarimetric concepts to CSAR data becomes challenging due to the diversity of the polarization basis. In this thesis, we deal with this problem by introducing polarization basis transformation to CSAR reconstruction algorithm. It is shown that the building structure can be recovered by this novel CSAR image reconstruction processing.

Chapter 2

Synthetic Aperture Radar

Introduction

Synthetic aperture radar (SAR) is an imaging radar of which the platform such as an aircraft or satellite travels along a linear or non-linear trajectory to synthesize a large antenna aperture for high-resolution image formation. In this thesis, the two kinds of SAR imaging techniques are dealt with, namely, *linear* and *circular SAR*. The term "linear SAR" is used to indicate so-called stripmap or spotlight mode SAR systems which possess a linear radar trajectory. The linear SAR is the most widely recognized and used imaging technique, and the majority of SAR image processing and analysis algorithms assume this type of observation. The circular SAR (CSAR) literally has a circular radar trajectory, and its antenna beam points toward the center of the circular path during the acquisition. The CSAR has the capability of produce a high-resolution image compared to the linear SAR, however, the imaged area is restricted to the antenna beam swath. In addition, the interpretation of CSAR images is more challenging than that of the linear SAR images.

As the groundwork for SAR image analysis, this chapter briefly presents the reconstruction algorithms for the data acquired by the linear SAR systems. Using the results of linear SAR image analysis obtained until Chapter 5, we try to understand the image measured using the CSAR system. Unless confusion arises we simply refer to linear SAR as "SAR" in this thesis.

Outline

The outline of this chapter is as follows. In Section 2.1, SAR observation scenario is introduced, and the global coordinate system is defined for subsequent discussion. We show that, though SAR measurement is done in three-dimensional space, the formulation of image reconstruction algorithm only requires two-dimensional representation of the signal. Section 2.2 describes the reconstruction algorithm for one-dimensional range domain. The commonly used signal models, that is, pulsed, frequency-modulated continuous-wave (FMCW), and stepped-frequency waveforms are presented and the relationships of these signal models are established. Then, two-dimensional image formation based on the *wavefront reconstruction theory* [1] is given in Section 2.3. The images formed via this reconstruction algorithm are the basis of our polarimetric radar image analysis. For the discussion on the radar image in the later chapters, Section 2.4 summarizes the experimental system used in this research, and Section 2.5 describes the collected data. Finally, Section 2.6 concludes the chapter.

Mathematical Notations

The notations related to the Fourier transform with respect to time or spatial domain are summarized. We denote the time variable as t and its Fourier counterpart temporal frequency as ω, where the units of t and ω are *seconds* (s) and *radians* (rad./s). The frequency can be represented by $\omega/2\pi$ that has the unit of *Hertz* (Hz).

The forward Fourier transform of a time domain signal $s(t)$ with respect to the time t is defined as

$$\begin{aligned} S(\omega) &= \mathcal{F}_{(t)}\left[s(t)\right] \\ &= \int_{-\infty}^{\infty} s(t)\exp(-j\omega t)dt. \end{aligned} \tag{2.1}$$

The inverse Fourier transform of Equation (2.1) with respect to the temporal frequency ω is

$$s(t) = \mathcal{F}^{-1}_{(\omega)}\left[S(\omega)\right] \tag{2.2}$$

$$= \frac{1}{2\pi}\int_{-\infty}^{\infty} S(\omega)\exp(j\omega t)d\omega. \tag{2.3}$$

As well as the time domain signal, we can define the forward Fourier transform of a spatial

variable function $f(x)$, where the unit of the spatial variable x is *meters* (m), that is,

$$F(k_x) = \mathcal{F}_{(k_x)}\left[f(x)\right] \tag{2.4}$$

$$= \int_{-\infty}^{\infty} f(x)\exp(-jk_x x)dx, \tag{2.5}$$

where k_x is called the *spatial frequency* or *wavenumber* domain, the unit of which is *radians/meter* (rad./m). The inverse Fourier transform of a spatial frequency domain signal of Equation (2.5) is

$$f(x) = \mathcal{F}^{-1}_{(k_x)}\left[F(k_x)\right] \tag{2.6}$$

$$= \frac{1}{2\pi}\int_{-\infty}^{\infty} F(k_x)\exp(jk_x t)dk_x. \tag{2.7}$$

For digital implementation, the above Fourier transforms are computed by the *discrete Fourier transform* (DFT) and the *inverse discrete Fourier transform* (IDFT). For a discrete sequence f_n which contains N evenly spaced samples, where $n \in [-N/2, N/2-1]$ is the sample index, DFT is defined via

$$F_m = \sum_{n=-N/2}^{N/2-1} f_n \exp\left(-j\frac{2\pi}{N}mn\right), \tag{2.8}$$

where $m \in [-N/2, N/2-1]$, and then IDFT is defined by

$$f_n = \frac{1}{N}\sum_{m=-N/2}^{N/2-1} F_m \exp\left(j\frac{2\pi}{N}mn\right). \tag{2.9}$$

The sample spacing in the time and frequency domain is related via

$$N\Delta_x\Delta_{k_x} = 2\pi, \tag{2.10}$$

where Δ_x and Δ_{k_x} are the sample spacing of the original sequence f_n and its Fourier counterpart domain, respectively. The above Equation (2.10) is important for digital implementation of the SAR data acquisition and reconstruction algorithms since it dictates *alias-free* region of the sampled signal.

The Fourier transform of a two-dimensional signal can similarly be defined. For example, the

Fourier transform pair of a signal $s(t,u)$, where u represents spatial domain, is

$$\begin{aligned} S(\omega, k_u) &= \mathcal{F}_{(t,u)}[s(t,u)] \\ &= \int_u \int_t s(t,u) \exp\left(-j\omega t - jk_u u\right) dt\, du \end{aligned} \tag{2.11}$$

and

$$\begin{aligned} s(t,u) &= \mathcal{F}^{-1}_{(\omega,k_u)}[S(\omega,k_u)] \\ &= \frac{1}{(2\pi)^2} \int_u \int_t s(t,u) \exp\left(j\omega t + jk_u u\right) d\omega\, dk_u \end{aligned} \tag{2.12}$$

where k_u is spatial frequency for u. The two-dimensional DFT and IDFT can be defined as well.

2.1 Observation Scenario

The SAR observation scenario is depicted in Figure 2.1. In linear SAR systems such as stripmap or spotlight SAR, a radar carrying platform (aircraft or satellite) moves along a linear path during the data acquisition. At a fixed platform location, the radar transmits a pulse and records the echoed signal. Although the platform has a certain velocity, we assume that the radar stops during one sequence of its transmission and reception, and then the aircraft moves to the next observation point. This model is called the *stop-and-go assumption*.

The high-resolution two-dimensional radar image of the targets is formed via subsequent signal processing. The target space is represented by (x', y', z'), and the resultant two-dimensional image space is identified by (x, y) in Figure 2.1. The distance in x domain is called *slant-range*, while x'-direction is the *ground-range*. The domain y' or y is called *cross-range* or *azimuth*.

This image, referred to as *slant-range* image, is a two-dimensional mapping of the three-dimensional target space (x', y', z'). Consider the target located at (x'_t, y'_t, z'_t), and the radar has its altitude of z'_c. In this case, this target is projected in the image plane at the location (x_t, y_t) identified by

$$(x_t,\, y_t) = \left(\sqrt{x_t'^2 + (z'_c - z'_t)^2},\, y'_t\right). \tag{2.13}$$

Thus, the height information of the target is lost by this projection; the height information is *transparent* to the user who has only a single-path SAR image. As it is discussed in Chapter 5, the height information can be recovered from multiple path or multi-angular SAR images. Also one can infer the target height by using a single-path CSAR measurement which is discussed in

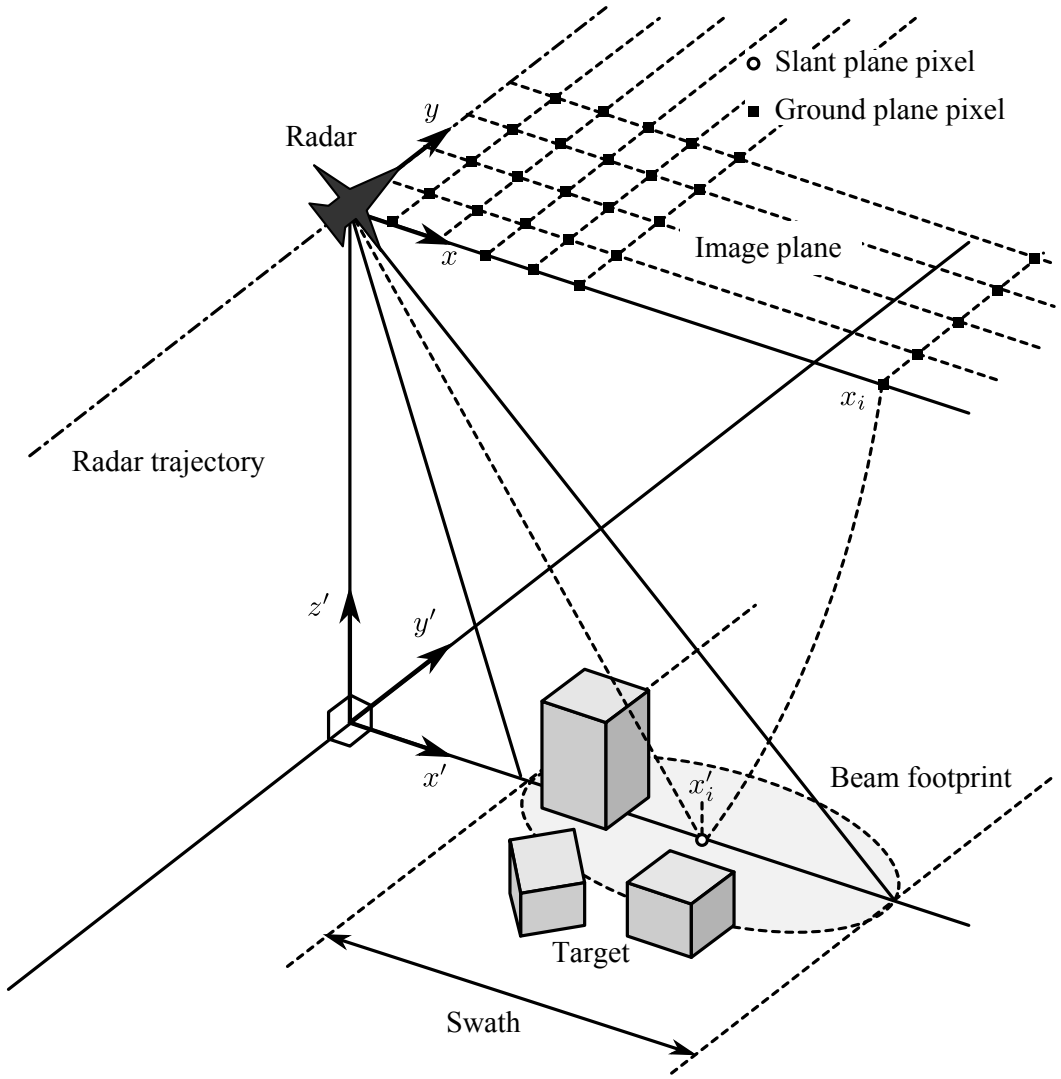

Figure 2.1: SAR observation scenario.

Chapter 6.

From the above discussion, one can formulate SAR reconstruction problem as the two-dimensional signal processing without loss of generality. We assume that all the observing targets are confined into the two-dimensional image plane (x, y), and we just call slant-range as "range" in this chapter.

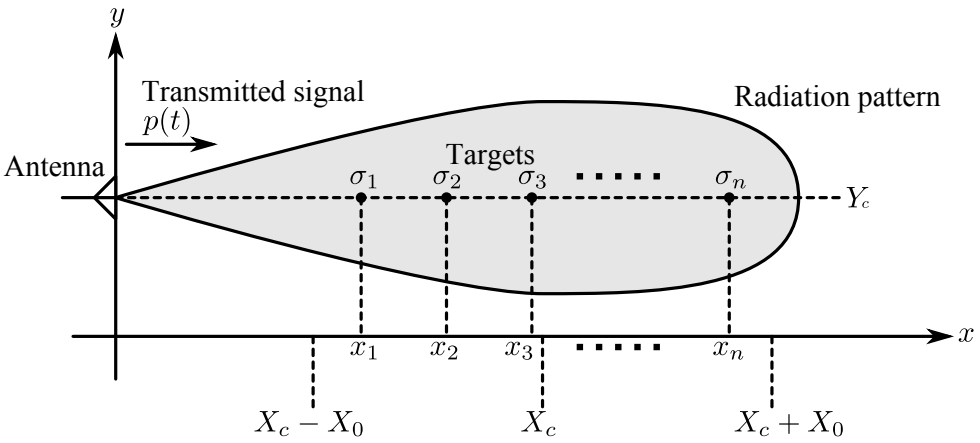

Figure 2.2: Range reconstruction system geometry.

2.2 Range Reconstruction

Before moving on to the two-dimensional image formation, we examine the one-dimensional target reconstruction in the range domain x in this section. The main purpose of this section is to provide range reconstruction algorithm for various signal waveforms using the Fourier transformation, that is, pulsed, FMCW, and stepped frequency ones. Also we establish the relationship of these signal models and show that the contained information is equivalent each other.

2.2.1 System model

The system model for range reconstruction is shown in Figure 2.2. In this problem, we assume that a set of targets are located at a known fixed range Y_c. The targets are assumed to be within a finite spatial region $[X_c - X_0, X_c + X_0]$, where X_c is the center range of the target area, and X_0 is the half-width of radar swath. The range x_n and the target reflectivity or radar cross section (RCS) σ_n are unknown constants to be recovered. Our problem here is to reconstruct or estimate these unknown constants from the measured signal.

2.2.2 Generic Signal Model

Let $p(t)$ be the transmitted signal waveform, where t is time variable, and $f(x)$ be the reflectivity function at the range x. The echoed signal model for the range imaging system can be described

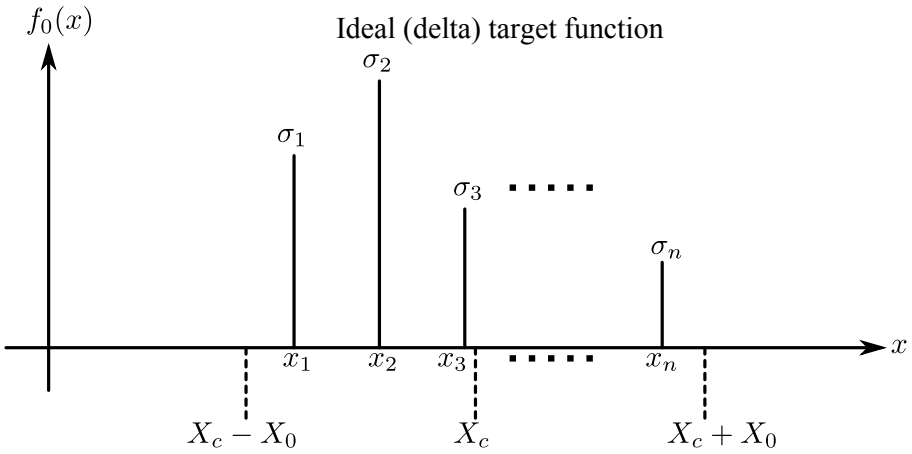

(a) Ideal target function.

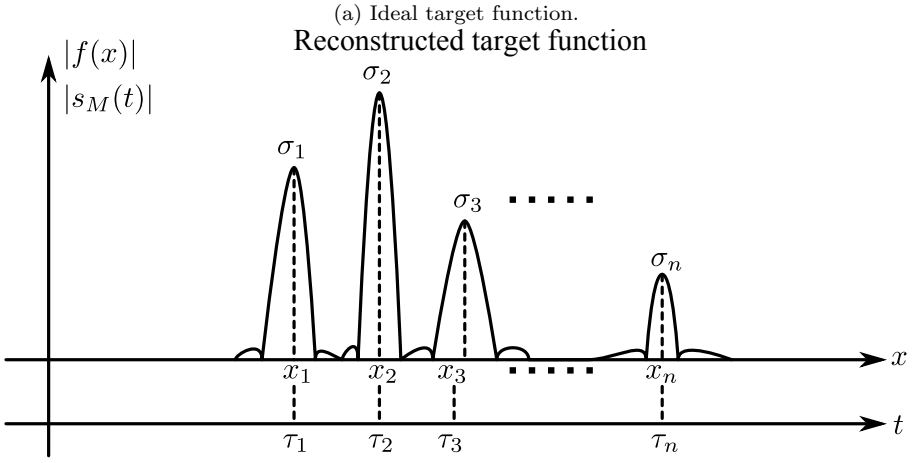

(b) Reconstructed target function.

Figure 2.3: (a) Ideal target function; (b) matched-filtered signal $s_M(t)$ and reconstructed target function $f(x)$.

as

$$\begin{aligned} s(t) &= \int_x f(x) p\left[t - \frac{2x}{c}\right] dx \\ &= f\left(\frac{ct}{2}\right) * p(t) \end{aligned} \tag{2.14}$$

where $*$ denotes convolution operation with respect to the fast-time t. For ideal point scatterer model, we can define the reflectivity function via

$$f_0(x) = \sum_n \sigma_n \delta(x - x_n), \tag{2.15}$$

where $\delta(\cdot)$ is the Dirac delta (impulse) function. The example of the above model of Equation (2.15) is depicted in Figure 2.3 (a). Substituting the above ideal target function into Equation (2.14), we have the following echoed signal model for the point scatterers:

$$\begin{aligned} s(t) &= f_0\left(\frac{ct}{2}\right) * p(t) \\ &= \sum_n \sigma_n p\left(t - t_n\right), \end{aligned} \tag{2.16}$$

with

$$t_n = \frac{2x_n}{c}. \tag{2.17}$$

2.2.3 Theoretical reconstruction

Let $P(\omega)$ be the Fourier transform of the transmitted waveform $p(t)$, that is,

$$P(\omega) = \mathcal{F}_{(t)}[p(t)], \tag{2.18}$$

where ω represents the fast-time frequency. Then, the Fourier transform of Equation (2.16) can be denoted by

$$\begin{aligned} S(\omega) &= \mathcal{F}_{(t)}[s(t)] \\ &= P(\omega) \sum_n \sigma_n \exp\left(-j\omega t_n\right). \end{aligned} \tag{2.19}$$

Provided that $P(\omega)$ has nonzero values for all fast-time frequency ω (i.e. infinite bandwidth), one can readily reconstruct the ideal target function via

$$\begin{aligned} \mathcal{F}^{-1}_{(\omega)}\left[\frac{S(\omega)}{P(\omega)}\right] &= \sum_n \sigma_n \delta\left(t - t_n\right) \\ &= f_0\left(\frac{ct}{2}\right). \end{aligned} \tag{2.20}$$

This operation is also known as the *deconvolution*. The spatial variable representation of the above target function is a linear mapping of the fast-time t defined via

$$f_0(x) = \sum_n \sigma_n \delta(x - x_n), \tag{2.21}$$

where

$$x = \frac{ct}{2}. \tag{2.22}$$

However, this theoretical reconstruction is practically unavailable because realistic radar systems have finite bandwidth.

2.2.4 Reconstruction via Matched Filtering

In realistic situations, infinite bandwidth is unavailable and Equation (2.20) cannot be used to reconstruct the target function from a bandlimited signal. For practical reconstruction, one can utilize the operation called matched- filtering which also appears in classical communication problems. The matched filter is designed to recover desirable information from a received signal corrupted with an additive white noise. In other words, the matched filtering operation maximizes signal-to-noise ratio (SNR) of the filter output. The matched filtering operation is achieved via

$$\begin{aligned} s_M(t) &= \mathcal{F}^{-1}_{(\omega)} \left[S(\omega) P^*(\omega) \right] \\ &= \mathcal{F}^{-1}_{(\omega)} \left[\sum_n \sigma_n |P(\omega)|^2 \exp\left(-j\omega t_n\right) \right] \\ &= \sum_n \sigma_n \mathrm{psf}_t \left(t - t_n\right), \end{aligned} \tag{2.23}$$

where $[\cdot]^*$ is the complex conjugate operation, and

$$\mathrm{psf}_t(t) = \mathcal{F}^{-1}_{(\omega)} \left[|P(\omega)|^2 \right], \tag{2.24}$$

is called the point spread function (PSF) of the imaging system. The example of the matched-filtered signal $s_M(t)$ is displayed in Figure 2.3 (b). The matched filtered signal of Equation (2.23) can also be expressed using the time domain convolution as follows:

$$\begin{aligned} s_M(t) &= s(t) * p^*(-t) \\ &= f_0\left(\frac{ct}{2}\right) * \mathrm{psf}_t(t). \end{aligned} \tag{2.25}$$

Recalling that the ideal target function is expressed as Equation (2.15), one can consider that the PSF describes how ideal delta target function spreads out due to the effect of bandlimited imaging system.

For example, we consider the following transmitted radar signal spectrum:

$$P(\omega) = \begin{cases} 1 & \text{for } \omega \in [\omega_c - \omega_0, \omega_c + \omega_0], \\ 0 & \text{otherwise,} \end{cases} \tag{2.26}$$

where ω_c and ω_0 are the carrier (center) frequency and the half-size of baseband bandwidth, respectively. Then, PSF can be represented by

$$\text{psf}_t(t) = \exp(j\omega_c t)\text{sinc}\left(\frac{\omega_0 t}{\pi}\right), \tag{2.27}$$

where

$$\text{sinc}(t) = \frac{\sin(\pi t)}{\pi t} \tag{2.28}$$

is the sinc function. From Equation (2.27), PSF becomes sharper with the radar bandwidth $2\omega_0$ increases; the better resolution can be achieved by the wider bandwidth.

The above assumption of the radar signal spectrum of Equation (2.26) can be considered as the model which describes FMCW and stepped frequency waveform described below.

2.2.5 Reconstruction for FMCW Signaling

The other well-known radar waveform is frequency modulated continuous wave (FMCW), which is also known as a chirp or linear frequency modulated (LFM) signal. The FMCW radar signal is defined via

$$p(t) = \exp(j\beta t + j\alpha t^2), \tag{2.29}$$

where β and α respectively represent the initial phase and chirp rate of the FMCW signal, and both variables are assumed to be real quantities. The FMCW signal of Equation (2.29) continues during the chirp duration T_p. For the FMCW radar measurement, we assume that all the responses form the targets are observable within this chirp duration.

The instantaneous frequency of Equation (2.29) can be calculated by the following derivative.

$$\begin{aligned} \omega &= \frac{d}{dt}(\beta t + \alpha t^2) \\ &= \beta + 2\alpha t. \end{aligned} \tag{2.30}$$

The above Equation (2.30) is a linear function of the fast-time t, and thus, Equation (2.29)

represents a LFM signal; the frequency is linearly swept, starting from β to the end of the sweep. A positive α means *up-chirp* that the frequency is increased as time elapses, while decreasing frequency sweep called *down-chirp* is described by a negative α. The following discussion assumes the up-chirp case of positive α. The frequency is within the interval

$$\omega \in [\beta, \beta + 2\alpha T_p]. \tag{2.31}$$

The carrier (center) frequency ω_c is then,

$$\omega_c = \beta + \alpha T_p, \tag{2.32}$$

and the baseband bandwidth ω_0 is

$$\pm\omega_0 = \pm\alpha T_p. \tag{2.33}$$

The baseband bandwidth of the FMCW signal depends on the two variables of the chirp rate α and the chirp duration T_p. For a given α, the bandwidth of a FMCW signal increases with the chirp duration T_p.

The echoed signal model of FMCW radar for the case of point scatterers defined in Equation (2.16) can be denoted by

$$\begin{aligned} s(t) &= \sum_n \sigma_n p\left(t - t_n\right) \\ &= \sum_n \sigma_n \exp[j\beta(t - t_n)] \exp\left[j(\alpha t^2 - 2\alpha t_n t + \alpha t_n^2)\right]. \end{aligned} \tag{2.34}$$

The measured quantity of the FMCW radar called *beat signal* is obtained via mixing the complex conjugate of Equation (2.34) and the transmitted waveform as a reference signal, that is,

$$\begin{aligned} s_b(t) &= s^*(t)p(t) \\ &= \sum_n \sigma_n \exp(j\beta t_n - j\alpha t_n^2) \underbrace{\exp(j2\alpha t_n t)}_{\text{Sinusoid}} \end{aligned} \tag{2.35}$$

The sinusoidal term in the above Equation (2.35) contains the information related to the target range; as the delay time t_n increases with the target range, the frequency of the resultant sinusoid becomes higher. The time domain compression is achieved by taking the Fourier transform of

the beat signal $s_b(t)$. This procedure is also referred to as the *pulse compression* or *deramping*.

The above mentioned FMCW signaling has another characteristic which makes the connection between FMCW and pulsed waveform. Provided that the targets are within relatively near range, that is,

$$t_n \ll 1, \tag{2.36}$$

the beat signal of Equation (2.35) can be approximated by

$$s_b(t) \approx \sum_n \sigma_n \exp\left[j(\beta + 2\alpha t)t_n\right]. \tag{2.37}$$

Recalling that the instantaneous frequency of the FMCW signal is described by Equation (2.30), one can represent Equation (2.37) via

$$s_b(t) = \sum_n \sigma_n \exp\left(j\omega t_n\right). \tag{2.38}$$

Therefore, we can consider the beat frequency $s_b(t)$ as the frequency domain signal $s_b(\omega)$. Then, we define the following signal:

$$\begin{aligned} S(\omega) &= P(\omega)s_b(\omega)^* \\ &= P(\omega)\sum_n \sigma_n \exp\left(-j\omega\tau_n\right), \end{aligned} \tag{2.39}$$

where

$$P(\omega) = \begin{cases} 1 & \text{for } \omega \in [\omega_c - \omega_0, \omega_c + \omega_0], \\ 0 & \text{otherwise.} \end{cases} \tag{2.40}$$

Equation (2.39) has the same form of Equation (2.19), that is, the fast-time Fourier transform of received pulse radar signal. Therefore, FMCW beat signal can be considered as a special case of the pulse radar waveform; the contained information of both waveforms is equivalent. Moreover Equation (2.40) corresponds to the previous mentioned example of Equation (2.26), and thus the point spread function of the FMCW radar system can be determined by a sinc function defined in Equation (2.27).

The reconstruction is done by Equation (2.23) which ends up with the simple inverse Fourier

transformation defined via

$$\begin{aligned} s_M(t) &= \mathcal{F}^{-1}_{(\omega)}[S(\omega)] \\ &= \sum_n \sigma_n \exp[j\omega_c(t-t_n)]\text{sinc}\left[\frac{\omega_0(t-t_n)}{\pi}\right]. \end{aligned} \tag{2.41}$$

2.2.6 Reconstruction for Stepped Frequency Signaling

The stepped frequency signaling is useful when the user does not have an access to a high-speed A/D converter. Similar to the previous discussion on the FMCW signaling, the stepped frequency signal contains the same information of the pulsed waveform.

The transmitted signal of the stepped frequency radar is a simple sinusoid, that is,

$$p(t;\omega) = \exp(j\omega t). \tag{2.42}$$

The echoed signal model of this transmitted waveform for the case of point scatterers defined in Equation (2.16) can be denoted by

$$\begin{aligned} s(t;\omega) &= \sum_n \sigma_n p\left(t - \frac{2x_n}{c}\right) \\ &= \sum_n \sigma_n \exp\left[j\omega(t-t_n)\right]. \end{aligned} \tag{2.43}$$

The measured quantity of the stepped frequency radar is the ratio of this received signal to the transmitted signal, that is,

$$\begin{aligned} s_r(\omega) &= \frac{s(t;\omega)}{p(t;\omega)} \\ &= \sum_n \sigma_n \exp\left(j\omega t_n\right), \end{aligned} \tag{2.44}$$

provided that $p(t;\omega) \neq 0$. The above Equation (2.44) is only a function of frequency variable ω; the fast-time dependency is suppressed by taking the ratio, provided that the frequency of the returned signal $s(t;\omega)$ is equal to that of the transmitted waveform $p(t;\omega)$. For wide-bandwidth radar measurement, the frequency ω is *stepped* or *swept* to the other frequencies. Note that Equation (2.44) only holds provided that the targets are static over the observation period. If one observes a dynamic object, the echoed signal $s(t;\omega)$ would contain a different frequency component compared to the transmitted signal $p(t;\omega)$ due to so-called the *Doppler frequency*

shift.

We define the following signal:

$$\begin{aligned} S(\omega) &= P(\omega) s_r^*(\omega) \\ &= P(\omega) \sum_n \sigma_n \exp\left(-j\omega t_n\right), \end{aligned} \tag{2.45}$$

where

$$P(\omega) = \begin{cases} 1 & \text{for } \omega \in [\omega_c - \omega_0, \omega_c + \omega_0], \\ 0 & \text{otherwise.} \end{cases} \tag{2.46}$$

Equation (2.45) has the same form of Equation (2.19), that is, the fast-time Fourier transform of pulse radar received signal. Therefore, stepped frequency radar waveform can be considered as a special case of the pulse radar waveform as well as the FMCW case. Moreover Equation (2.46) corresponds to the previous mentioned example of Equation (2.26), and thus the point spread function of the stepped frequency radar system can be determined by Equation (2.27).

The reconstruction equation for the stepped frequency signal is, using Equation (2.23),

$$\begin{aligned} s_M(t) &= \mathcal{F}_{(\omega)}^{-1}[S(\omega)] \\ &= \sum_n \sigma_n \exp[j\omega_c(t - t_n)] \text{sinc}\left[\frac{\omega_0(t - t_n)}{\pi}\right], \end{aligned} \tag{2.47}$$

which is exactly same as the FMCW case of Equation (2.41).

2.2.7 Summary of Signal Models

So far, three types of radar signal model, namely the pulsed waveform, the FMCW, and the stepped frequency signaling, are discussed. We have shown that, though these waveforms have the different time-domain representation, the contained information can be considered as the same in the frequency domain representation. The idea is depicted in Figure 2.4.

For a general pulsed radar case, one has to firstly take the Fourier transform of the received signal $s(t)$ with respect to the fast-time t, and then, matched filter reconstruction of Equation (2.23) is used.

In the FMCW case, the time-domain beat signal $s_b(t)$ is assigned to the frequency domain signal via Equation (2.37) to form the Equation (2.39) which has the similar fashion of Equation (2.19). Then, the user can use the matched filter reconstruction described in Equation (2.23).

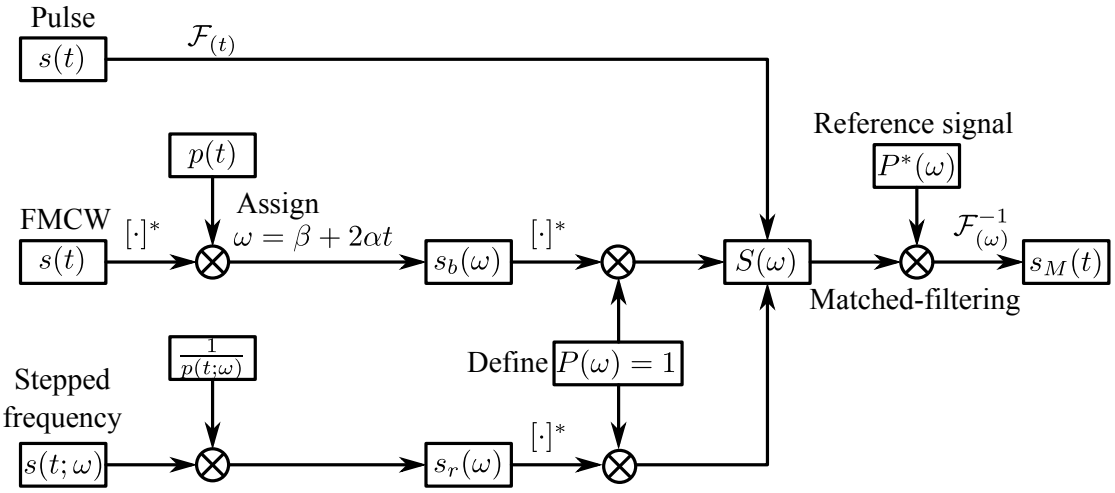

Figure 2.4: Summary of matched-filter reconstruction for each signal models.

Similarly, the stepped frequency radar signal defined in Equation (2.43) can be directly plugged into Equation (2.23). Because both the FMCW and stepped frequency case correspond to the example given in Equation (2.26), the matched filter reconstruction defined in Equation (2.23) ends up to the simple inverse Fourier transform, that is,

$$\begin{aligned} s_M(t) &= \mathcal{F}^{-1}_{(\omega)}[S(\omega)] \\ &= \sum_n \sigma_n \exp[j\omega_c(t-t_n)]\text{sinc}\left[\frac{\omega_0(t-t_n)}{\pi}\right]. \end{aligned} \tag{2.48}$$

The maximum of the sinc function occurs when $t = t_n$, and one can determine the target range x_n via

$$x_n = \frac{ct_n}{2}. \tag{2.49}$$

2.3 Synthetic Aperture Reconstruction

So far, the basis of the signal modeling and range reconstruction procedure is presented. Now we develop a SAR image formation algorithm based on the previous discussion.

2.3.1 System Model

The SAR imaging system geometry is depicted in Figure 2.5. The radar carrying aircraft moves along y-direction. The position of the radar is denoted by $u \in [-L, L]$, where L is the half-size of

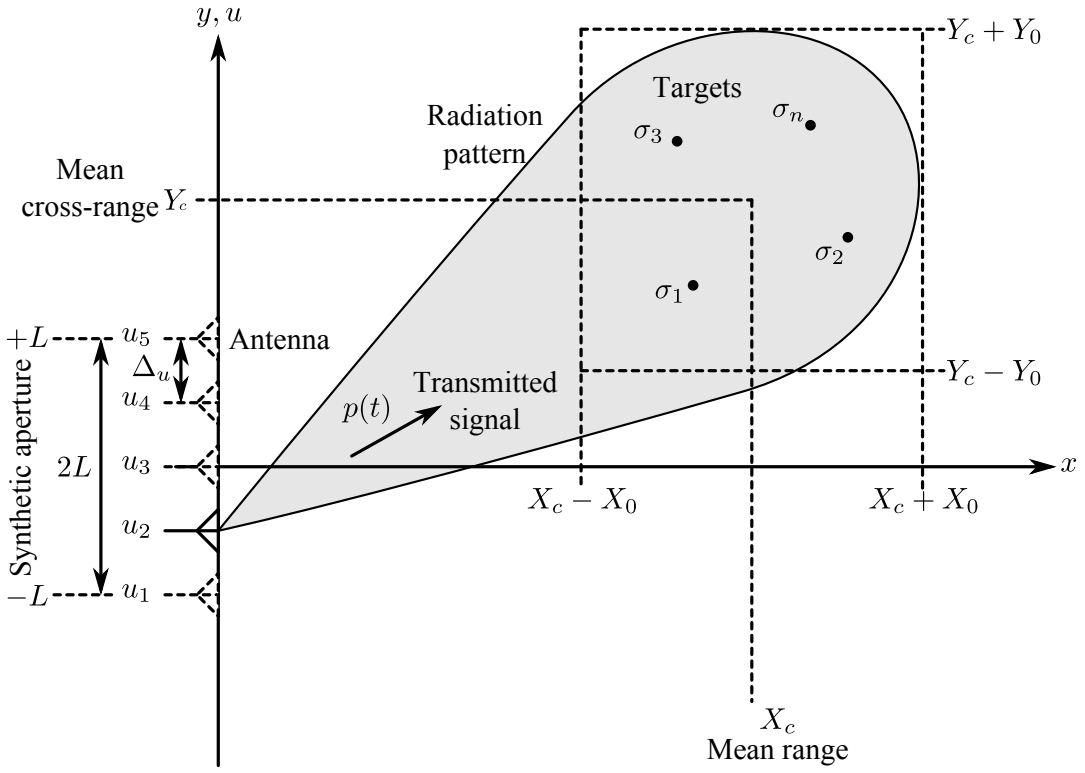

Figure 2.5: SAR system geometry.

the *synthetic aperture*. The radar position u is referred to as *slow-time* domain, while the time related to the transmitted pulse is called *fast-time* t domain; the aircraft motion is relatively *slow* compared to the transmitted radio wave which travels at the *fast* speed of light c.

The *radial* or *line-of-sight* (LOS) distance from the radar to the target located at (x, y) is

$$r(x, y) = \sqrt{x^2 + (y - u)^2}, \tag{2.50}$$

and the corresponding delay time is

$$t_r(x, y) = \frac{2r(x, y)}{c}. \tag{2.51}$$

We denote the continuous reflectivity function of the location (x, y) as $f(x, y)$. For a discrete target model, we can write the reflectivity function via

$$f(x, y) = \sum_n \sigma_n \delta(x - x_n)\delta(y - y_n), \tag{2.52}$$

where σ_n is the reflectivity of the nth target, and (x_n, y_n) is the location of this target, respectively. For this discrete model, we define the following radial distance and the time delay:

$$r_n = r(x_n, y_n), \tag{2.53}$$

and

$$t_n = t_r(x_n, y_n). \tag{2.54}$$

In this model, center of the target region is at (X_c, Y_c), and the extent of this region is

$$x \in [X_c - X_0, X_c + X_0], \tag{2.55a}$$

$$y \in [Y_c - Y_0, Y_c + Y_0], \tag{2.55b}$$

where X_0 and Y_0 are the half-width of the target region in x and y domain, respectively.

2.3.2 Signal Model

Let $p(t)$ be the transmitted radar pulse. The echoed signal at the slow-time u for continuous reflectivity function given in $f(x, y)$ is

$$\boldsymbol{s}(t, u) = \int_x \int_y f(x, y) p\left[t - t_r(x, y)\right] dy\, dx. \tag{2.56}$$

For the discrete model, plugging Equation (2.52) into the above Equation (2.56) yields

$$\boldsymbol{s}(t, u) = \sum_n \sigma_n p\left(t - t_n\right). \tag{2.57}$$

In the subsequent discussion, we employ the discrete model in Equation (2.57) is assumed for simplicity.

One can form a so-called real aperture radar image via the fast-time matched filtering as follows:

$$\begin{aligned} s_M(t, u) &= s(t, u) * p^*(-t) \\ &= \sum_n \sigma_n \mathrm{psf}_t \left(t - \frac{2r_n}{c}\right). \end{aligned} \tag{2.58}$$

The cross-range resolution of the real aperture image is restricted to the antenna beam width,

and the above equation is used only for displaying the synthetic aperture measurement.

2.3.3 Fourier Transform of the Received Signal

For matched filter reconstruction, it is required to derive the two-dimensional Fourier transform of the SAR received signal of Equation (2.57) with respect to fast-time t and slow-time u. We denote the fast-time frequency domain by ω and its wavenumber domain $k = \omega/c$, respectively. Also we express the Fourier transform of the transmitted pulse $p(t)$ as $P(\omega)$.

The one-dimensional Fourier transform of the SAR echoed signal given in Equation (2.57) is

$$s(\omega, u) = P(\omega) \sum_n \sigma_n \exp(-j2kr_n). \tag{2.59}$$

As mentioned in the discussion on the range reconstruction problem, the signal representation in the above form can be commonly used for various waveforms. For FMCW and stepped frequency waveform, we can assume the following signal spectrum:

$$P(\omega) = \begin{cases} 1 & \text{for } \omega \in [\omega_c - \omega_0, \omega_c + \omega_0], \\ 0 & \text{otherwise.} \end{cases} \tag{2.60}$$

Next we consider the Fourier transform of the Equation (2.59) with respect to slow-time u. The *method of stationary phase* states that, ignoring the unimportant amplitude function, the Fourier transform of the Equation (2.59) has the following form [1, 2]:

$$\begin{aligned} S(\omega, k_u) &= \mathcal{F}_{(u)}\left[s(\omega, u)\right] \\ &= P(\omega) \sum_n \sigma_n \exp\left(-j\sqrt{4k^2 - k_u^2}x_n - jk_u y_n\right), \end{aligned} \tag{2.61}$$

where k_u is the Fourier counterpart domain of the slow-time u. Then, the reconstruction algorithm can be developed based on the Equation (2.61).

2.3.4 Reconstruction

Our objective is to recover the target function $f(x, y)$ from the measured SAR signal defined in Equation (2.56). For this purpose, we present the Fourier properties of the discrete target function in Equation (2.52). The two-dimensional Fourier transform of Equation (2.52) with

respect to the fast-time t and slow-time u is

$$F(k_x, k_y) = \sum_n \sigma_n \exp(-jk_x x_n - jk_y y_n), \tag{2.62}$$

where (k_x, k_y) is the Fourier counterpart domain of the spatial variables (x, y), called spatial frequencies. Comparing Equation (2.61) and the above Equation (2.62), we can rewrite Equation (2.62) by

$$S(\omega, k_u) = P(\omega)F(k_x, k_y), \tag{2.63}$$

with the spatial frequency mapping defined via

$$k_x = \sqrt{4k^2 - k_u^2}, \tag{2.64a}$$

$$k_y = k_u. \tag{2.64b}$$

The spatial frequency mapping defined in Equation (2.64) is so-called the *Stolt mapping* which originates the analysis of seismic wave propagation [9]. The nonlinear mapping of k_x domain in Equation (2.64a) implies that we must *interpolate* the original unevenly spaced samples of k_x so that we have the evenly spaced samples of k_x domain to perform DFT or IDFT algorithms for the digital implementation.

Apart from the digital implementation issues, theoretical synthetic aperture reconstruction or deconvolution based on Equation (2.63) can be achieved via

$$F(k_x, k_y) = \frac{S(\omega, k_u)}{P(\omega)}, \tag{2.65}$$

provided that the signal $P(\omega) \neq 0$ for all ω. However, since $p(t)$ is a bandlimited signal, this theoretical reconstruction is not a practical option. Therefore, we should use the following matched-filter reconstruction:

$$\begin{aligned} F(k_x, k_y) &= P^*(\omega)S(\omega, k_u) \\ &= |P(\omega)|^2 \sum_n \sigma_n \exp(-jk_x x_n - jk_y y_n). \end{aligned} \tag{2.66}$$

As mentioned earlier, the digital implementation of the above Equation (2.66) involves the one-dimensional interpolation of unevenly spaced samples of k_x.

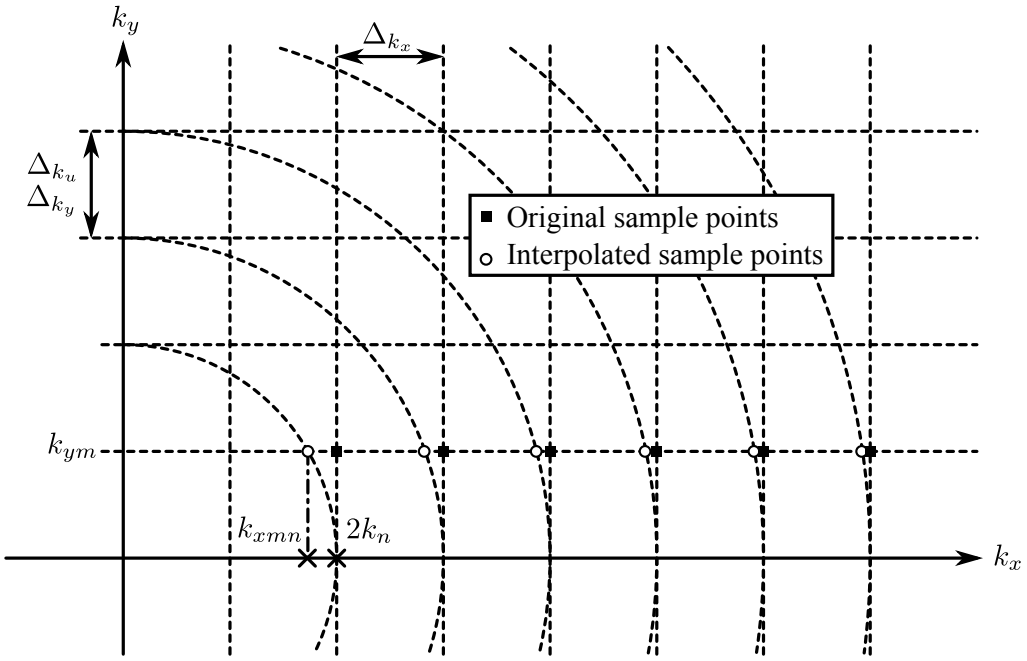

Figure 2.6: SAR spatial frequency interpolation (Stolt mapping).

2.3.5 Digital Implementation via Spatial Frequency Interpolation

So far, the reconstruction procedure for SAR measured signal is discussed. Next we deal with the digital implementation of the reconstruction problem. The key to achieve this is the spatial frequency mapping which is described in Equation (2.64) and interpolation of unevenly spaced spatial frequency samples of k_x. The idea of the spatial frequency interpolation called *Stolt interpolation* is shown in Figure 2.6.

Suppose that we have M discrete synthetic aperture samples of the SAR signal $s(\omega, u)$ with sample spacing Δ_u in the slow-time u domain. From the relationship of DFT sample spacing which is defined in Equation (2.10), we obtain M samples of $S(\omega, k_u)$ in the slow-time Doppler k_u domain with the following sample spacing:

$$\Delta_{k_u} = \frac{2\pi}{M\Delta_u}. \tag{2.67}$$

From the spatial frequency mapping of Equation (2.64), we have the values of $S(\omega, k_u)$ at evenly spaced values of k_u. However, range spatial frequency is a nonlinear mapping defined as Equation (2.64a). Since DFT algorithm assumes evenly spaced samples, we have to *interpolate*

from unevenly spaced values of k_x at

$$k_{xmn} = \sqrt{4k_n^2 - k_{um}} \tag{2.68}$$

where

$$k_n = n\Delta_k \tag{2.69}$$

are evenly spaced points in the fast-time wavenumber k domain and Δ_k is the sample spacing in this domain. Once the evenly spaced samples at the grid in (k_x, k_y) domain are obtained, one can take the two-dimensional inverse DFT with respect to the spatial frequency variables (k_x, k_y) to recover the two-dimensional reflectivity function $f(x, y)$.

2.4 Experimental System

This section summarizes the data acquisition system used in this research. A four-port vector network analyzer (VNA) is employed for the anechoic chamber measurements. To form a synthetic aperture, the antennas connected to the VNA is automatically scanned by a X-Y scanner. Inverse SAR (ISAR) measurement data is acquired by rotating the targets deployed on a turntable with the fixed radar antennas. For multiple angle SAR measurement, the targets are located on a elevation table which can tilt the targets.

2.4.1 Radar Transmitter and Receiver

In this research, we use a fully polarimetric X-band SAR system based on a vector network analyzer (VNA). The VNA can generate stepped frequency waveform described in Section 2.2.6. The simplified structure of a two-port VNA is shown in Figure 2.7. The source generates a sinusoid with a single frequency. As shown in this figure, we assume that the source is switched to the port 1 circuit. A part of the source signal is memorized in a_1, and the another part is transfered to the port 1 and then, the wave is transmitted to the target by the transmitting antenna. The reflected wave from the target arrives at the antenna connected to port 1 and port 2, and this received wave is respectively denoted by b_1 and b_2. Using these signals, the measured quantities called the *S-parameters* for port 1 transmission are formed via

$$S_{11} = \frac{b_1}{a_1}\Big|_{a_2=0}, \quad S_{21} = \frac{b_2}{a_1}\Big|_{a_2=0}. \tag{2.70}$$

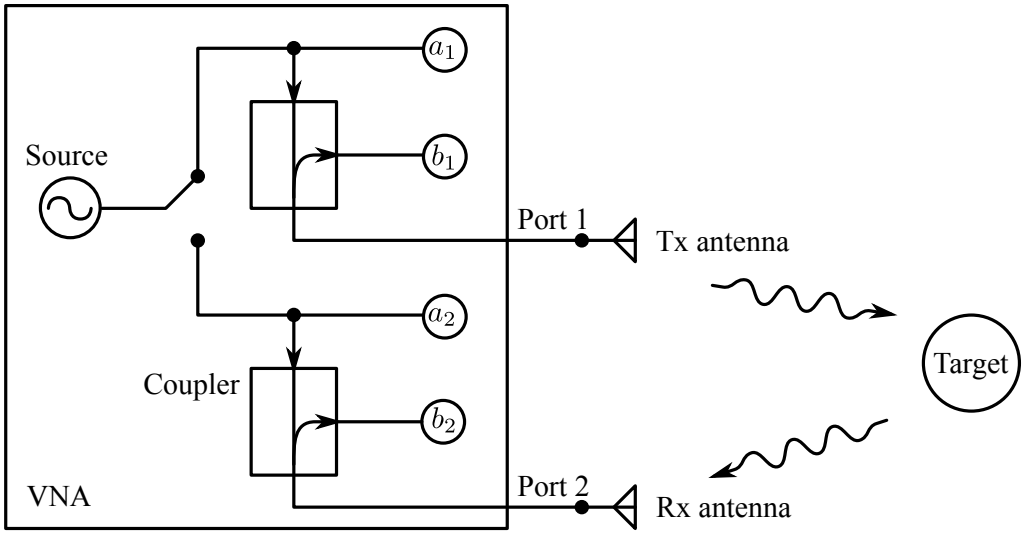

Figure 2.7: Simplified structure of a 2-port vector network analyzer.

Also the S-parameters for port 2 transmission is similarly defined by letting $a_1 = 0$. For polarimetric measurement, one has to change the combination of the transmitting and receiving antenna polarization, and therefore, S_{21} parameter is preferable for polarimetric measurement. Also S_{11} parameter would contain the stronger undesired antenna coupling than that of the S_{21} parameter. Throughout the thesis, we employ S_{21} parameter as the stepped frequency received signal, that is,

$$s_r(\omega) = S_{21}. \tag{2.71}$$

2.4.2 System Delay Compensation

In actual measurements, the transmitted and received signal experiences the certain delay due to the RF cable, amplifier, internal circuits of the receiver, and so on. For precise SAR image reconstruction, it is essential to remove these effect. The situation in which the system delay exists is depicted in Figure 2.8.

In this system model, the transmitter and receiver delay lengths are denoted by X_d^t and X_d^r, respectively. For the system delay compensation, one has to deploy a point-like targets such as conducting sphere or small trihedral reflector at known range X_k. The delayed version of the transmitted waveform is

$$p_d(t) = p\left(t - \frac{X_d^t}{c}\right), \tag{2.72}$$

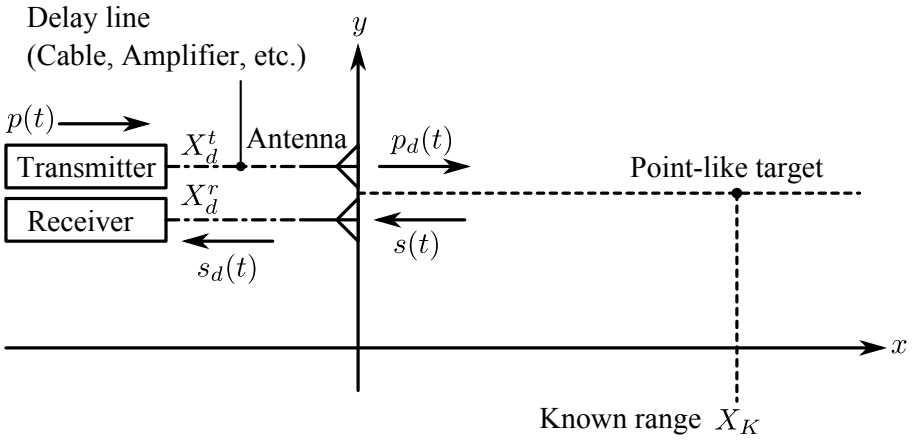

Figure 2.8: System delay model.

and the received signal becomes

$$\begin{aligned} s_d(t) &= \sigma_K \cdot p_d\left(t - \frac{2X_k + X_d^r}{c}\right) \\ &= \sigma_K \cdot p\left(t - \frac{2X_k + X_d^t + X_d^r}{c}\right). \end{aligned} \tag{2.73}$$

The Fourier transform of the above delayed signal model with respect to the fast-time t is

$$S_d(\omega) = \sigma_K P(\omega) \exp\left(-j\omega\frac{X_d}{c}\right) \exp\left(-j\omega\frac{2X_k}{c}\right), \tag{2.74}$$

where X_d is the total system delay defined by

$$X_d = X_d^t + X_d^r. \tag{2.75}$$

Once the total system delay length X_d is estimated or the user has *a priori* knowledge of the length, the delay can be removed in the fast-time frequency domain as follows:

$$S(\omega) = S_d(\omega) \exp\left(j\omega\frac{X_d}{c}\right). \tag{2.76}$$

Because we assume that the point-like calibration target is deployed in the radar front-end at known range X_k, one can readily estimate the total system delay length X_d by comparing the fast-time reconstruction of Equation (2.74) and the known range X_k. The peak position of the

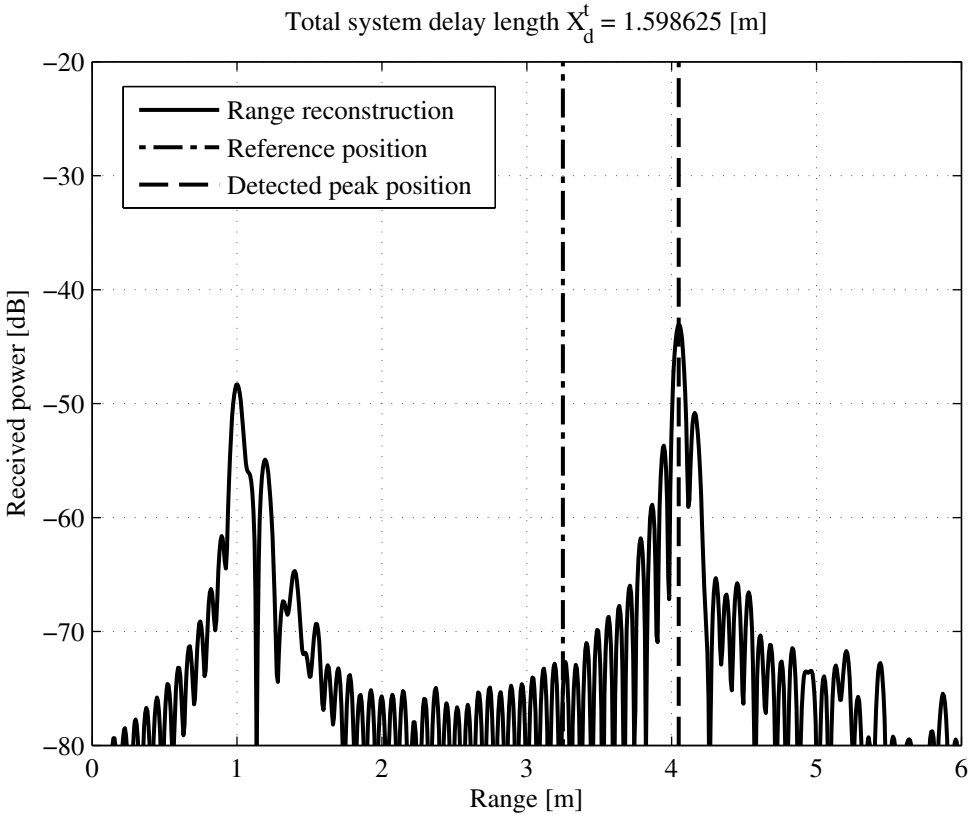

Figure 2.9: Range reconstruction via IFFT for a conducting sphere in hh-polarization and estimated total system delay length X_d.

reconstructed target function from Equation (2.74), denoted X_p, occurs at

$$X_p = X_k + X_d, \tag{2.77}$$

where both X_p and X_k are known constant, and the total system delay X_d is immediately derived from the above Equation (2.77). In the remaining discussion in this thesis, we assume that the system delay is properly compensated via the above procedure.

2.4.3 Ground Range Projection

The image obtained by a single-path linear SAR system is a slant plane image rather than a ground plane image. Even so in certain applications, it is convenient to convert the slant plane image into the ground plane image by projecting the slant plane pixels onto the ground plane

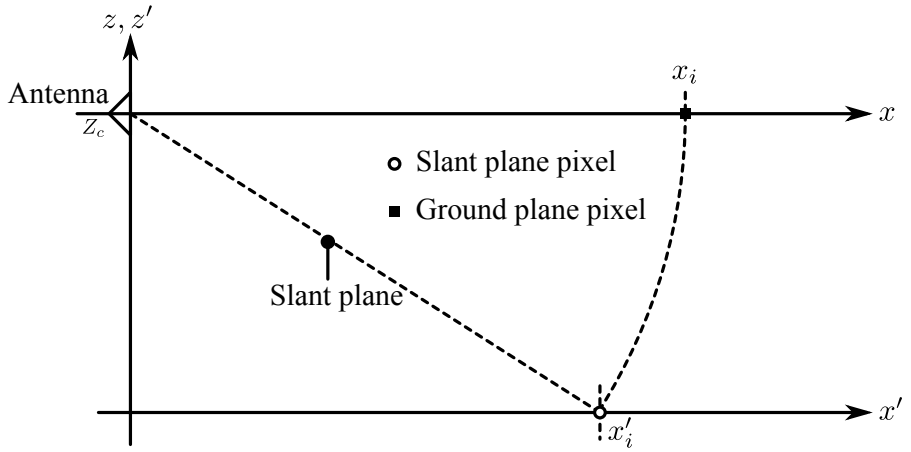

Figure 2.10: Ground range projection geometry (X-Y scanner measurement).

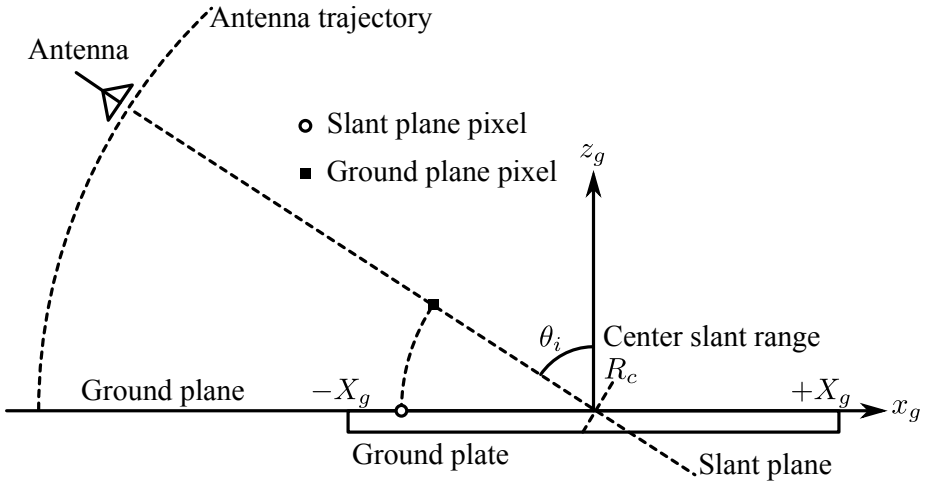

Figure 2.11: Ground range projection geometry (elevation table measurement).

using the geometric relationship between the radar and ground.

Figure 2.10 is the ground range projection geometry for the linear SAR observation using X-Y antenna scanner. We denote the fixed antenna altitude by Z_c. For this situation, the mapping of the slant range location x to the ground range position x' is defined via

$$x_i = \sqrt{x_i'^2 + Z_c^2}. \tag{2.78}$$

The corresponding ground range pixel x_i is obtained via one-dimensional interpolation.

Figure 2.11 shows the ground range projection geometry for the forest model using the elevation table to vary an incidence angle. In this case, the antenna location in the ground range

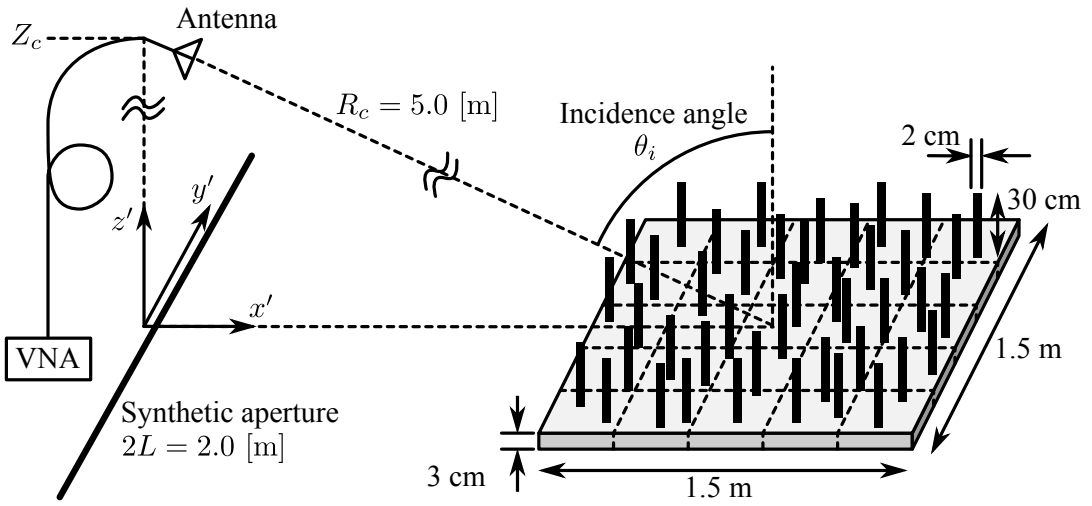

Figure 2.12: Target geometry (forest model).

direction vary with the rotation of the elevation table. Thus, the origin of the ground range is set to the center of the ground plate. The mapping is defined via

$$x_i = \sqrt{R_c^2 + x_g^2 + 2R_c x_g \sin\theta_i}, \tag{2.79}$$

and this pixel is obtained by one-dimensional interpolation.

2.5 Measured Data

This section provides the measured SAR and inverse SAR (ISAR) data which is referred throughout the thesis. The detailed analysis for the measured and reconstructed SAR images are discussed in the later chapters.

2.5.1 Forest Model

The forest model is composed of a cloud of wooden cylinders which stands vertically on a flat wooden plate. The target geometry is depicted in Figure 2.12. The purpose of this model is to emulate the scattering from a simple forest of which the foliage can be ignored. Such a situation is expected to occur when one observes Boreal forest at L-band or a longer wavelength. The notable feature of this model is that the wooden test pieces are put in water before the overall observation, and the measurement is made at different moisture conditions. The test pieces are

Table 2.1: Measurement parameter (forest model).

Center frequency [GHz]	10
Bandwidth [GHz]	2
Synthetic aperture length [m]	2
Trunk radius [cm]	1
Trunk length [cm]	30
Trunk density [m^{-2}]	56
Trunk orientation	Vertical
Moisture condition	9 conditions
Polarization	hh, hv, vh, vv

packed with plastic film to prevent the inside water from evaporating during one sequence of measurements. In addition, the trunk distribution density is changed to investigate the effects of forest biomass. For multiple angle observation, the test pieces are installed on the elevation table, and SAR measurements is done at each incidence angle.

Measurement Parameter

The measurement parameters of the forest model is listed in Table 2.1. This forest model is used to investigate the variation of moisture content of forested terrain. For this purpose, we measured the forest model target in 9 different moisture conditions with the fixed trunk density. Figure 2.13 shows the measured gravimetric moisture content for the ground plate and wooden cylinders at each moisture condition. Unfortunately, the deviation of gravimetric moisture of the ground plate is large and we cannot determine the specific moisture content for each condition. Instead of using the gravimetric moisture, we use the number from 1 to 9, called Wet-number, to indicate each moisture condition. For example, Wet-9 means the most wettest condition which is right after removing the plates from water, whereas Wet-1 indicates the most driest condition.

Reconstructed SAR Image

A reconstructed ground range SAR image of the forest model is shown in Figure 2.14. The wet condition is Wet-8 and the incidence angle is $\theta_i = 45°$. In the figure, the scattering from the distributed trunks are identified by the boxes.

2.5.2 Building Model

The building model is constructed from concrete blocks as shown in Figure 2.15 (a), and the details of these blocks are depicted in Figure 2.15 (b). The model is used to imitate the observation

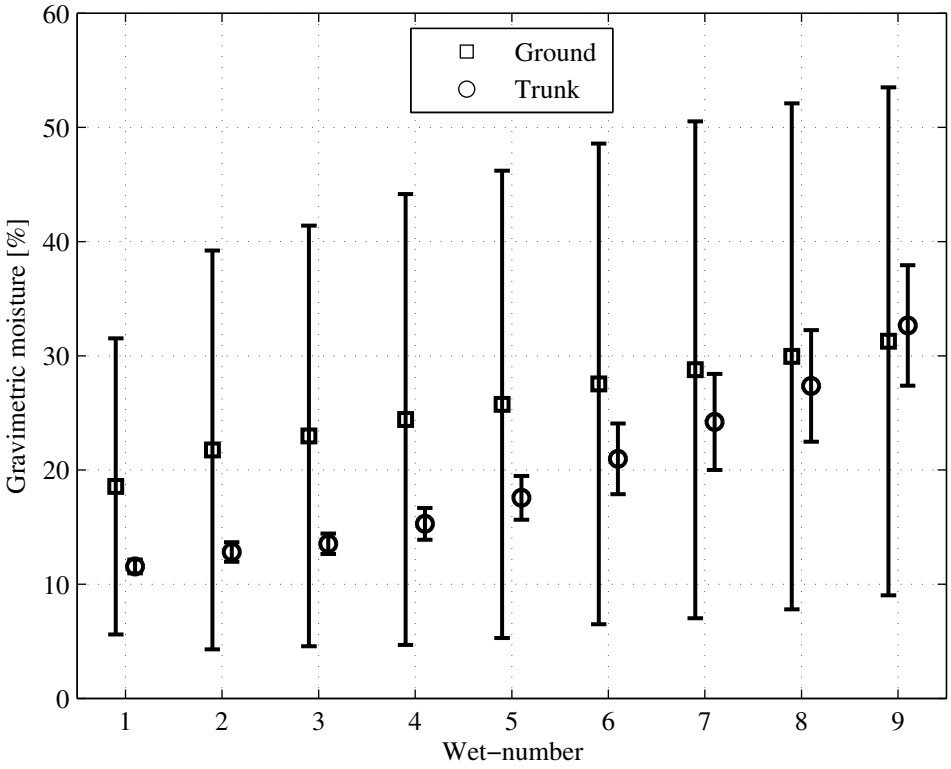

Figure 2.13: Measured gravimetric moisture contents.

of urban area. Some of the blocks are oriented with respect to the horizontal axis. The numbered blocks are stack of concrete cubes and each number indicates the number of the stacked cubes as shown in Figure 2.15 (b). For this model, both linear SAR and circular SAR measurements are made.

Measurement Parameter

The sets of measurement parameters for the building model is listed in Table 2.2 and 2.3. In the measurement using the parameters in Table 2.2, the radar altitude measured from the ground concrete plate is varied from 0.68 m to 1.7 m with 3 cm step. The model is used for the polarimetric and tomographic reconstruction given in Chapter 5.

Reconstructed SAR Image

A sample reconstructed linear SAR image of the building model is shown in Figure 2.16. The scattering from the ground plate edge is clearly imaged, and the block wall facing toward the

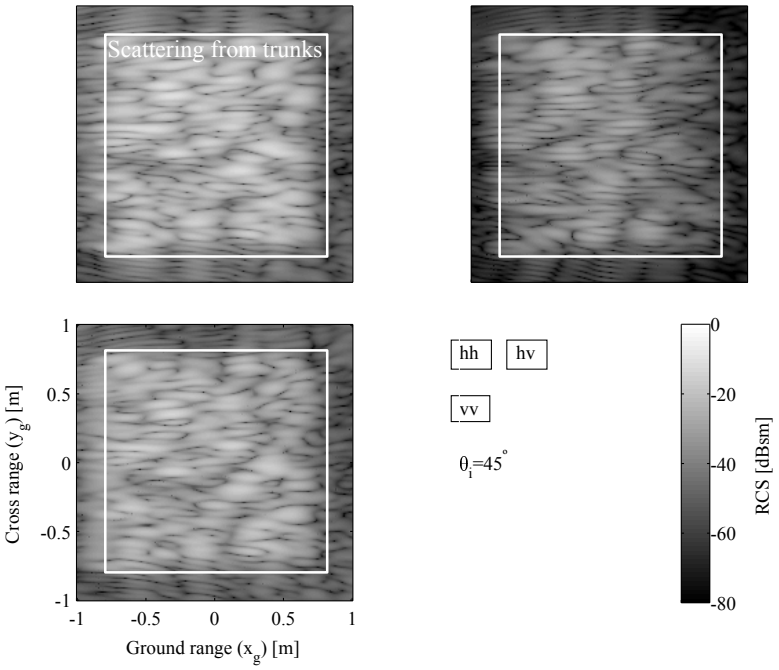

Figure 2.14: Reconstructed ground range image (forest model, center incidence angle $\theta_i = 45°$, Wet-8 condition).

Table 2.2: Measurement parameter (building model, linear SAR).

Center frequency [GHz]	10
Bandwidth [GHz]	2
Synthetic aperture length [m]	2
Radar altitude [m]	0.68–1.7
Altitude step [cm]	3
Polarization	hh, hv, vh, vv

antenna is also appeared in this image. However, the oriented or shadowed blocks are hardly seen in this image. The oriented blocks can be imaged using CSAR measurement described in Chapter 6, and the discrimination of the ground plate edge and blocks is possible via Tomographic SAR in Chapter 5.

2.6 Summary of This Chapter

This chapter described the basics of SAR image formation algorithms. Using the wavefront reconstruction theory, the high-resolution images can be reconstructed from the wide-bandwidth SAR measurements. The algorithm can be applied for the different radar waveforms, that is,

Table 2.3: Measurement parameter (building model, CSAR).

Center frequency [GHz]	10
Bandwidth [GHz]	2
Synthetic aperture length [deg.]	360
Radar altitude [m]	0.68–1.7
Altitude step [cm]	3
Radius of trajectory R_g [m]	2.9
Depression angle θ_z [deg.]	30
Polarization	hh, hv, vh, vv

pulsed, FMCW, and stepped frequency radar signal.

We also explained the stepped frequency measurement system which is able to acquire fully polarimetric SAR or ISAR data. For image reconstruction from the measured data, the system delay compensation is necessary and the method to do this is presented. The collected data and reconstructed SAR images are presented for the discussion in the subsequent chapters.

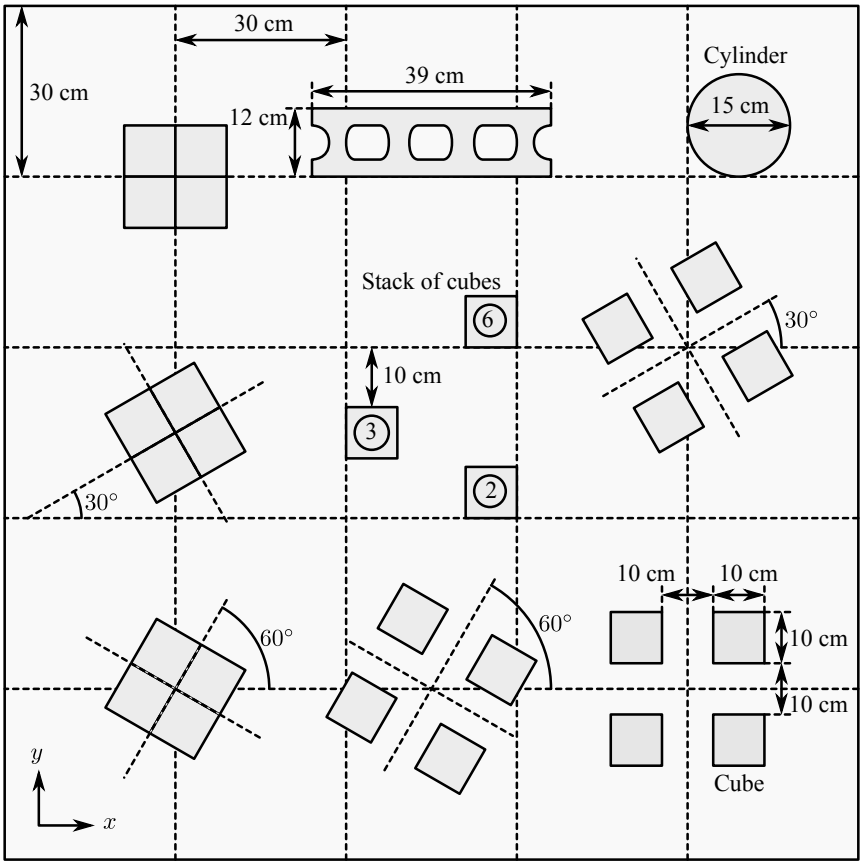

(a) Top view.

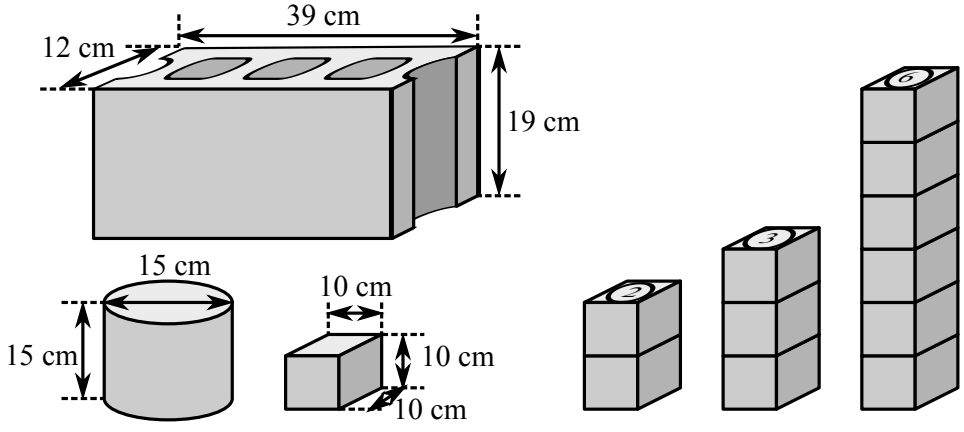

(b) Details of concrete blocks.

Figure 2.15: Building model target.

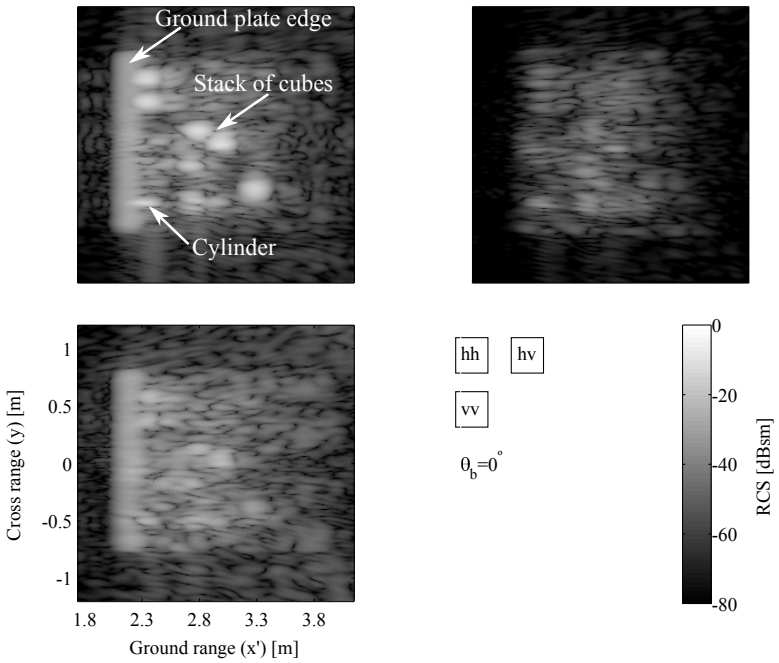

Figure 2.16: Reconstructed ground range image (building model, radar altitude $Z_c = 1.7$ [m], no azimuthal orientation).

Chapter 3

Polarimetric SAR

Introduction

The previous Chapter 2 described how the high-resolution SAR image is formed. Now, we can easily extend our discussion to the fully polarimetric case. The SAR system which utilizes the polarized wave is referred to as *polarimetric SAR* (PolSAR). The use of polarization of electromagnetic wave for the analysis of radar images aids the understanding of the observing scene. In this chapter, we present a brief review of radar polarimetry and describes several polarimetric target decomposition schemes.

The polarimetric radar backscatter from the earth terrain is a mixture of several scattering mechanisms such as surface scattering, double-bounce scattering, volume scattering, and the combination of these scattering mechanisms. The objective of the polarimetric target decomposition is to decompose such a complicated scattering phenomena into some simple scattering mechanisms using the information of the transmitted and received polarization states.

Until today, a number of polarimetric decomposition algorithms have been proposed and applied to the PolSAR images acquired by a spaceborne or airborne radar. One commonly used decomposition scheme is H-Alpha-Anisotropy decomposition developed by Cloude and Pottier [10], which is based on the eigenvalues of a polarimetric coherency matrix described later. The other method is called *model-based decomposition* that is based on physical scattering models [10, 5].

However, the validity of the decomposition algorithms are still subjected to investigation, because relating the decomposed results and real physical quantities such as soil moisture or forest biomass is difficult. In addition, the decomposed result using each decomposition algorithm could

be significantly different from each other, which complicates the understanding of the observing scene. Therefore, to aid the interpretation of the decomposed results, it could be convenient that we present the comparison of these decomposition algorithms. The aim of this section is to provide the reader with the qualitative comparison of the model-based decomposition algorithms using the measured data of the controlled laboratory experiments given in Chapter 2.

Outline

The outline of this chapter is as follows. Section 3.1 defines the observation scenario of PolSAR measurement considered in this chapter. In Section 3.2, the fundamental quantity to represent polarimetric radar data called the Sinclair *scattering matrix* and relationship between the reconstructed SAR images and the scattering matrix is given. Also we define several vector and matrix notations of polarimetric data for further discussion. Based on these polarimetric quantities, we present model-based polarimetirc decomposition algorithms in Section 3.3. Then, Section 3.4 shows the experimental results using the PolSAR images given in Chapter 2. Finally, Section 3.5 summarizes the discussion in this chapter.

3.1 Observation Scenario

The observation scenario of PolSAR is quite similar to those which is depicted in Figure 2.1 of Chapter 2 except for utilization of the four combination of transmitting and receiving polarization channels. The radar carrying platform travels along a straight line along y direction. As mentioned in Chapter 2, the three-dimensional reflectivity function in (x', y', z') is projected into the two-dimensional (x, y) image plane.

3.1.1 Signal Model

We denote the transmitted and received polarization state by α and β, respectively. The α-polarized transmitted pulse at a slow-time location u is represented by $p_\alpha(t, u)$, where t is the fast-time domain. For the lexicographic basis, the polarization states α and β are defined as $\alpha, \beta \in h, v$, where h represents horizontal polarization channel while v is vertically polarized channel. Using this notation, the *polarimetric* target reflectivity function is represented as $f_{\beta\alpha}(x, y)$. For

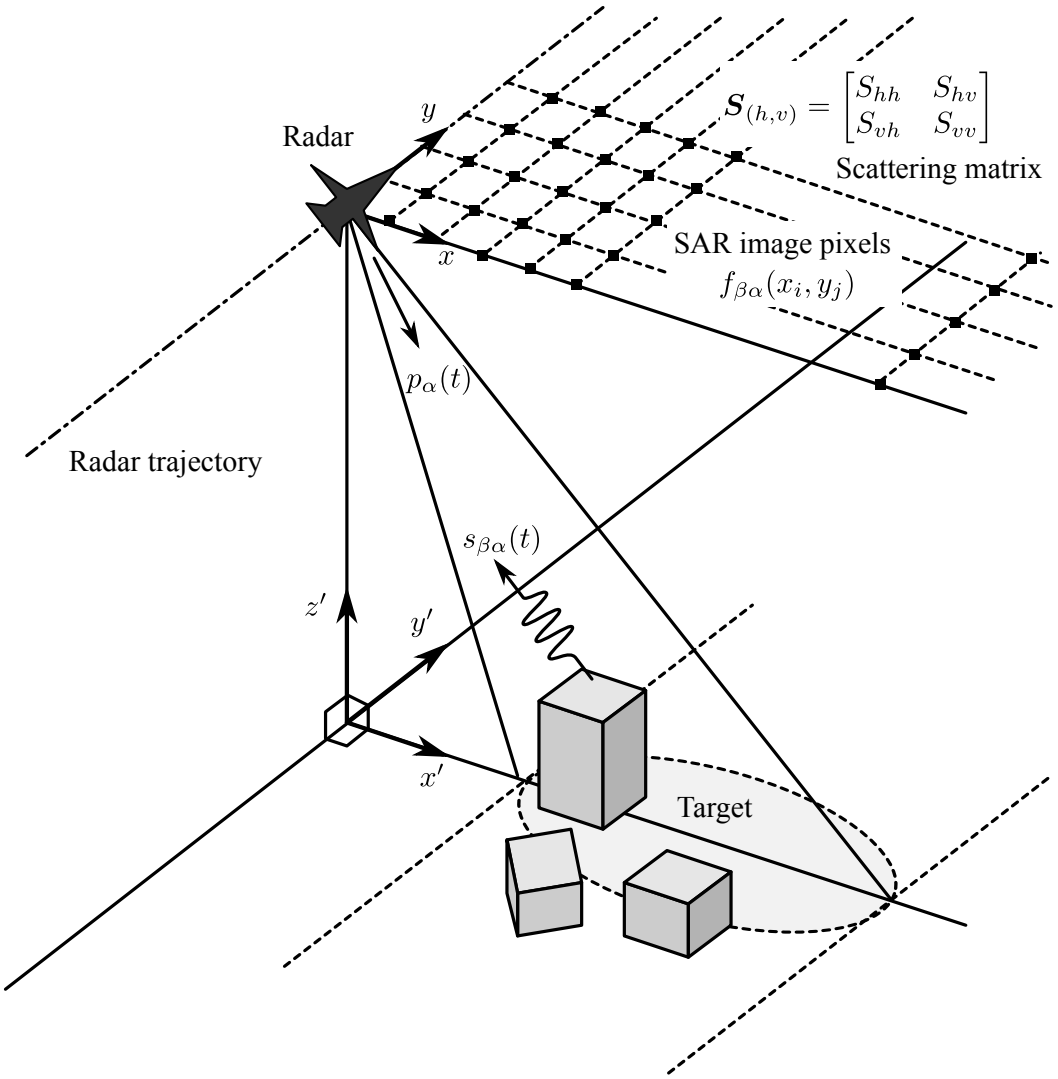

Figure 3.1: SAR observation scenario.

a discrete model, this function can be defined via

$$f_{\beta\alpha}(x, y) = \sum_n \sigma_n^{\beta\alpha} \delta(x - x_n)\delta(y - y_n), \tag{3.1}$$

where $\sigma_n^{\beta\alpha}$ is the reflectivity for the nth point target when a α-polarized wave arrives at this target and then the target scattered back a β-polarized wave. Using this model, polarimetric

echoed signal model can be represented by

$$s_{\beta\alpha}(t,u) = \sum_n \sigma_n^{\beta\alpha} p_\alpha(t - t_n), \tag{3.2}$$

where t_n is the round-trip delay for the nth point target defined in Equation (2.54).

3.1.2 Reconstruction

The objective of the reconstruction is to recover the polarimetric reflectivity function $f_{\beta\alpha}(x,y)$ or $\sigma_n^{\beta\alpha}$ from Equation (3.2). The reconstruction of the polarimetric received signal in Equation (3.2) is exactly same as the procedure described in Chapter 2. For convenience of the subsequent discussion, we denote target reflectivity at a pixel location identified by (x_i, y_j) as $f_{\beta\alpha}(x_i, y_j)$. Then, now we have the SAR images for each combination of the polarization channels, that is, hh, hv, vh, and vv for the lexicographic basis case. These polarimetric reflectivity functions are the basis of the development of polarimetric decomposition algorithms.

3.2 Polarimetric Vectors and Matrices

In polarimetric radar image analysis, the most basic quantity can be described as the 4×4 Sinclair scattering matrix. Using the notational conventions defined in Section 3.1, the polarimetric image pixel $f_{\beta\alpha}(x_i, y_j)$ is linked with the scattering matrix via

$$\begin{aligned} \boldsymbol{S}_{(h,v)} &= \begin{bmatrix} S_{hh}(x_i,y_j) & S_{hv}(x_i,y_j) \\ S_{vh}(x_i,y_j) & S_{vv}(x_i,y_j) \end{bmatrix} \\ &= \begin{bmatrix} f_{hh}(x_i,y_j) & f_{hv}(x_i,y_j) \\ f_{vh}(x_i,y_j) & f_{vv}(x_i,y_j) \end{bmatrix}. \end{aligned} \tag{3.3}$$

For notational simplicity, we arbitrarily omit the image pixel index (x_i, y_j) in the following discussion.

If we assume the monostatic configuration (e.g. the transmitter and receiver is located at the same position), the cross-polarized channels are equivalent to each other, that is,

$$S_{hv} = S_{vh}. \tag{3.4}$$

In realistic SAR systems, Equation (3.4) might not be satisfied since the transmitting and receiv-

ing antenna is located at slightly different positions. In such a case, one can utilize the following *symmetrized* scattering matrix $\boldsymbol{S}'_{(h,v)}$:

$$\boldsymbol{S}'_{(h,v)} = \frac{1}{2}\left[\boldsymbol{S}_{(h,v)} + \boldsymbol{S}^T_{(h,v)}\right], \tag{3.5}$$

where $[\cdot]^T$ represents the vector or matrix transpose operation. It is reported that the above symmetrization could achieve 3 dB improvement of the signal-to-noise ratio (SNR) in the cross-polarized channel [11]. This is due to the fact that the noise component in the cross-polarized channels are uncorrelated and the above summation suppress the noise component, while the cross-polarized signals are correlated each other and the above averaging does not weaken the signal component. Throughout this thesis, we assume that the monostatic assumption defined in (3.4) is satisfied or the measured matrix is symmetrized via Equation (3.5), and we simply write the symmetrized matrix $\boldsymbol{S}'_{(h,v)}$ as $\boldsymbol{S}_{(h,v)}$.

Then, the scattering matrix can be written as

$$\boldsymbol{S}_{(h,v)} = \begin{bmatrix} S_{hh} & S_{hv} \\ S_{hv} & S_{vv} \end{bmatrix}. \tag{3.6}$$

In addition, the following vectorized notation is convenient for further discussion.

$$\boldsymbol{k}_L = \begin{bmatrix} S_{hh} & \sqrt{2}S_{hv} & S_{vv} \end{bmatrix}^T. \tag{3.7}$$

We refer to the above vector as scattering vector. Using the scattering vector, we define the *averaged covariance matrix* as

$$\begin{aligned} \langle \boldsymbol{C}_{(h,v)} \rangle &= \frac{1}{N_p}\sum_{i,j} \boldsymbol{k}_L \boldsymbol{k}_L^\dagger \\ &= \begin{bmatrix} \langle S_{hh}S_{hh}^* \rangle & \sqrt{2}\langle S_{hh}S_{hv}^* \rangle & \langle S_{hh}S_{vv}^* \rangle \\ \sqrt{2}\langle S_{hh}S_{hh}^* \rangle & 2\langle S_{hh}S_{hv}^* \rangle & \sqrt{2}\langle S_{hh}S_{vv}^* \rangle \\ \langle S_{vv}S_{hh}^* \rangle & \sqrt{2}\langle S_{vv}S_{hv}^* \rangle & \langle S_{vv}S_{vv}^* \rangle \end{bmatrix}, \end{aligned} \tag{3.8}$$

where $\langle \cdot \rangle$ represents ensemble average. We also define the following *Pauli basis* matrices:

$$\boldsymbol{\sigma}_0^P = \frac{1}{\sqrt{2}}\begin{bmatrix} 1 & 0 \\ 0 & 1 \end{bmatrix}, \quad \boldsymbol{\sigma}_1^P = \frac{1}{\sqrt{2}}\begin{bmatrix} 1 & 0 \\ 0 & -1 \end{bmatrix}, \quad \boldsymbol{\sigma}_2^P = \frac{1}{\sqrt{2}}\begin{bmatrix} 0 & 1 \\ 1 & 0 \end{bmatrix}. \tag{3.9}$$

Using the above basis, the scattering matrix is represented by the following Pauli scattering vector (also known as the coherency vector):

$$\begin{aligned}\boldsymbol{k}_P &= \left[\mathrm{Tr}\left\{\boldsymbol{S}_{(h,v)}\boldsymbol{\sigma}_0^P\right\} \quad \mathrm{Tr}\left\{\boldsymbol{S}_{(h,v)}\boldsymbol{\sigma}_1^P\right\} \quad \mathrm{Tr}\left\{\boldsymbol{S}_{(h,v)}\boldsymbol{\sigma}_2^P\right\}\right]^T \\ &= \frac{1}{\sqrt{2}}\left[S_{hh}+S_{vv} \quad S_{hh}-S_{vv} \quad 2S_{hv}\right]^T, \end{aligned} \tag{3.10}$$

where $\mathrm{Tr}\{\cdot\}$ represents the trace of a matrix. Then, we define the averaged coherency matrix via

$$\begin{aligned}\langle \boldsymbol{T}_{(h,v)} \rangle &= \frac{1}{N_p}\sum_{i,j} \boldsymbol{k}_P \boldsymbol{k}_P^\dagger \\ &= \begin{bmatrix} \langle |S_{hh}+S_{vv}|^2 \rangle & \langle (S_{hh}+S_{vv})(S_{hh}-S_{vv})^* \rangle & \langle 2S_{hv}^*(S_{hh}+S_{vv}) \rangle \\ \langle (S_{hh}-S_{vv})(S_{hh}+S_{vv})^* \rangle & \langle |S_{hh}-S_{vv}|^2 \rangle & \langle 2S_{hv}^*(S_{hh}-S_{vv}) \rangle \\ \langle 2S_{hv}(S_{hh}+S_{vv})^* \rangle & \langle 2S_{hv}(S_{hh}-S_{vv})^* \rangle & \langle 4|S_{hv}|^2 \rangle \end{bmatrix}. \end{aligned} \tag{3.11}$$

Theoretically, the above covariance matrix and the coherency matrix contain same information since the polarization vector and the Pauli scattering vector defined in Equation (3.7) and (3.10) is related by the unitary transformation, that is,

$$\boldsymbol{k}_P = \boldsymbol{U}_P \boldsymbol{k}_L, \tag{3.12}$$

where $\boldsymbol{U}_P$ is the unitary transformation matrix defined by

$$\boldsymbol{U}_P = \frac{1}{\sqrt{2}}\begin{bmatrix} 1 & 0 & 1 \\ 1 & 0 & -1 \\ 0 & \sqrt{2} & 0 \end{bmatrix}. \tag{3.13}$$

However, from a signal processing point of view, the covariance matrix defined in Equation (3.8) might be more preferable due to the property of additive noise. Because the additive noise of two different polarization channels can be considered to be incoherent, the additive noise component only remains in the diagonal terms of the covariance matrix, while the noise in coherency matrix may scatter around all the components of the coherency matrix.

Let us assume that the *measured* (noisy) scattering vector is modeled by

$$\boldsymbol{k}_L' = \boldsymbol{k}_L + \boldsymbol{n}_L, \tag{3.14}$$

where $\boldsymbol{n}_L$ represents the additive noise for each polarization channel. The covariance matrix for the above measured scattering vector is

$$\begin{aligned}\langle \boldsymbol{C}'_{(h,v)} \rangle &= \langle \boldsymbol{k}'_L \boldsymbol{k}'^{\dagger}_L \rangle \\ &= \boldsymbol{C}_{(h,v)} + \boldsymbol{C}_N, \end{aligned} \tag{3.15}$$

where $\boldsymbol{C}_N$ is the noise covariance matrix defined by

$$\boldsymbol{C}_N = \langle \boldsymbol{n}_L \boldsymbol{n}_L^{\dagger} \rangle. \tag{3.16}$$

Suppose that the additive noise is the white Gaussian noise of which the average is zero and the deviation is σ^2, the measured covariance matrix in Equation (3.15) becomes

$$\langle \boldsymbol{C}'_{(h,v)} \rangle = \boldsymbol{C}_{(h,v)} + \sigma^2 \boldsymbol{I}_{(3\times 3)}, \tag{3.17}$$

where $\boldsymbol{I}_{(M\times N)}$ represents $M \times N$ unit matrix.

Therefore, the noise in the off-diagonal components of the covariance matrix is suppressed by the ensemble average. This is not true for the components of the coherency matrix which contains a coherent summation of the element of scattering matrix. In this thesis, we employ the covariance matrix for ensemble averaging operation. In the case of requiring the coherency matrix, we arbitrarily convert the averaged covariance matrix into the coherency matrix form using the unitary transformation.

3.2.1 Pauli Decomposition

The Pauli scattering vector in Equation (3.10) can be viewed as a simple decomposition of the scattering matrix, since the first component of the Pauli vector $S_{hh} + S_{vv}$ enhances the single or odd-bounce scattering mechanism, while the second component $S_{hh} - S_{vv}$ intensifies the double- or even-bounce scattering mechanism. The third component $2S_{hv}$ can be interpreted as an indicator of target randomness, and thus the volume scattering such as the scattering from vegetated terrain would appears in this component.

Under these assumptions, the simplest polarimetric decomposition, referred to as the Pauli decomposition, is done by just displaying the components of the Pauli scattering vector which is

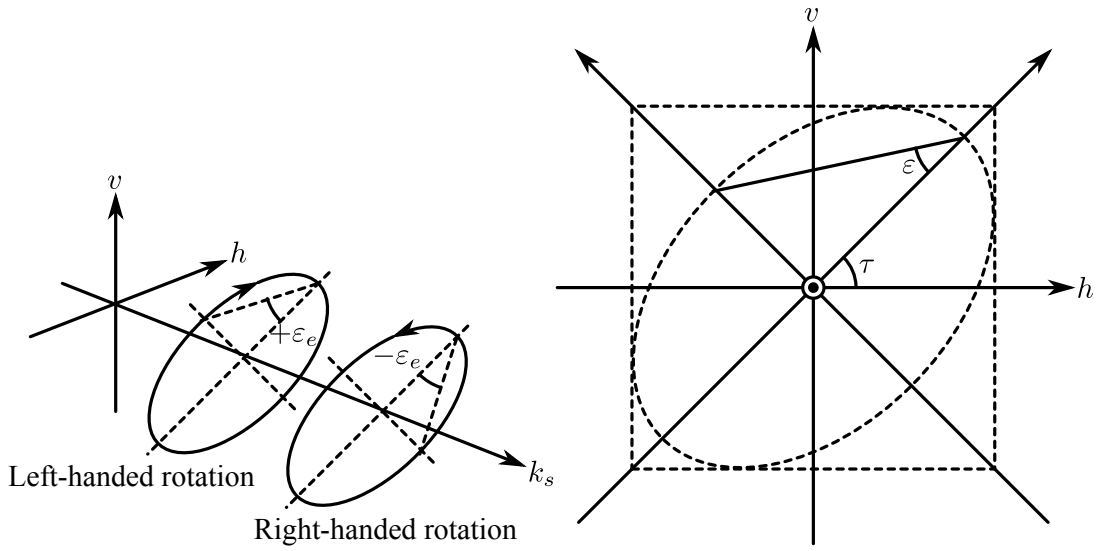

(a) Sense of rotation. (b) Elliptic parameter.

Figure 3.2: General elliptic polarization geometry.

given in Equation (3.10) as follows:

$$f_s = \frac{1}{2}|S_{hh} + S_{vv}|^2, \tag{3.18a}$$

$$f_d = \frac{1}{2}|S_{hh} - S_{vv}|^2, \tag{3.18b}$$

$$f_v = 2|S_{hv}|^2, \tag{3.18c}$$

where f_s, f_d, and f_v represent the surface (odd-bounce) scattering component, double-bounce (even-bounce) component, and volume scattering component.

3.2.2 Polarization Basis Transformation

Once polarimetric measurements in (h, v) polarization basis is obtained, one can transform the scattering matrix into the scattering matrix represented in an arbitrary polarization basis (a, b). Generally the transformed basis (a, b) represents an elliptic polarized wave as shown in Figure 3.2. In this figure, the parameter τ represents the tilt angle of the polarization ellipse, while ε describes the ellipticity. As described in [12], the polarization basis transformation is achieved

by

$$\begin{bmatrix} S_{aa} & S_{ab} \\ S_{ba} & S_{bb} \end{bmatrix} = \frac{1}{1+\rho_1\rho_1^*} \begin{bmatrix} e^{j\rho_2} & 0 \\ 0 & e^{-j\rho_2} \end{bmatrix} \begin{bmatrix} 1 & \rho_1 \\ -\rho_1^* & 1 \end{bmatrix} \begin{bmatrix} S_{hh} & S_{hv} \\ S_{vh} & S_{vv} \end{bmatrix} \begin{bmatrix} 1 & -\rho_1^* \\ \rho_1 & 1 \end{bmatrix} \begin{bmatrix} e^{j\rho_2} & 0 \\ 0 & e^{-j\rho_2} \end{bmatrix}, \tag{3.19}$$

where ρ_1 and ρ_2 are respectively defined as

$$\rho_1 = \frac{\tan\tau + j\tan\varepsilon}{1 - j\tan\tau\tan\varepsilon}, \tag{3.20a}$$

$$\rho_2 = \tan^{-1}(\tan\tau\tan\varepsilon). \tag{3.20b}$$

For the special case of circular (l, r) polarization basis, Equation (3.19) takes the following form by letting $\rho_1 = j$ and $\rho_2 = 0$:

$$\boldsymbol{S}_{(l,r)} = \begin{bmatrix} S_{ll} & S_{lr} \\ S_{rl} & S_{rr} \end{bmatrix} = \frac{1}{2} \begin{bmatrix} 1 & j \\ j & 1 \end{bmatrix} \begin{bmatrix} S_{hh} & S_{hv} \\ S_{vh} & S_{vv} \end{bmatrix} \begin{bmatrix} 1 & j \\ j & 1 \end{bmatrix}. \tag{3.21}$$

Also we can consider γ-rotated linear polarization basis (h', v') by letting $\rho_1 = \tan\gamma$ and $\rho_2 = 0$ as follows:

$$\boldsymbol{S}_{(h',v')} = \begin{bmatrix} S_{h'h'} & S_{h'v'} \\ S_{v'h'} & S_{v'v'} \end{bmatrix} = \begin{bmatrix} \cos\gamma & -\sin\gamma \\ \sin\gamma & \cos\gamma \end{bmatrix} \begin{bmatrix} S_{hh} & S_{hv} \\ S_{vh} & S_{vv} \end{bmatrix} \begin{bmatrix} \cos\gamma & \sin\gamma \\ -\sin\gamma & \cos\gamma \end{bmatrix}. \tag{3.22}$$

As it is discussed in Chapter 6, the polarization basis of circular SAR (CSAR) measurement is changed while the radar travels along a circular flight path. The above mentioned polarization basis transformation can be used to incorporate this effect into the CSAR image reconstruction algorithm [8].

3.3 Model Based Polarimetric Decompositions

So far, the fundamental quantities for PolSAR image analysis are established. Now we present the polarimetric decomposition algorithms based on the several polarimetric matrices given in Section 3.2. Although there are many polarimetric decomposition schemes, namely, physical or mathematical based decompositions, coherent or incoherent, and so forth, however, this section and remaining discussion focus on the physical model based polarimetric decomposition algorithms.

3.3.1 Freeman-Durden Decomposition

Freeman and Durden [5] proposed the following decomposition of the covariance matrix defined as Equation (3.8):

$$\langle \boldsymbol{C}_{(h,v)} \rangle = f_s \boldsymbol{C}_s + f_d \boldsymbol{C}_d + f_v \boldsymbol{C}_v, \tag{3.23}$$

where f_s, f_d, and f_v represent the surface, double-bounce, and volume scattering component, respectively. We refer this decomposition model as Freeman-Durden decomposition (FDD). The decomposed covariance matrices in Equation (3.23) are

$$\boldsymbol{C}_s = \begin{bmatrix} |\beta_s|^2 & 0 & \beta_s \\ 0 & 0 & 0 \\ \beta_s^* & 0 & 1 \end{bmatrix}, \quad \boldsymbol{C}_d = \begin{bmatrix} |\alpha_d|^2 & 0 & \alpha_d \\ 0 & 0 & 0 \\ \alpha_d^* & 0 & 1 \end{bmatrix}, \quad \boldsymbol{C}_v = \begin{bmatrix} 1 & 0 & 1/3 \\ 0 & 2/3 & 0 \\ 1/3 & 0 & 1 \end{bmatrix}, \tag{3.24}$$

where β_s and α_d are complex valued constants. The matrix $\boldsymbol{C}_v$ in the above equation is the model for randomly oriented dipole which represents thin vegetation structure.

From Equation (3.23), the following set of four equations which has five unknowns can be derived:

$$\langle |S_{hh}|^2 \rangle = f_s |\beta_s|^2 + f_d |\alpha_d|^2 + f_v, \tag{3.25a}$$

$$\langle |S_{vv}|^2 \rangle = f_s + f_d + f_v, \tag{3.25b}$$

$$\langle |S_{hv}|^2 \rangle = f_v/3, \tag{3.25c}$$

$$\langle |S_{hh} S_{vv}^*| \rangle = f_s \beta_s + f_d \alpha_d + f_v/3. \tag{3.25d}$$

To solve the above set of equations, Freeman and Durden [5] suggested that the volume scattering term f_v is determined by Equation (3.25c) before solving for the other terms. Once the volume scattering contribution is determined, one can make the following subtraction:

$$\langle \boldsymbol{C}'_{(h,v)} \rangle = \langle \boldsymbol{C}_{(h,v)} \rangle - \begin{bmatrix} 3\langle |S_{hv}|^2 \rangle & 0 & \langle |S_{hv}|^2 \rangle \\ 0 & 2\langle |S_{hv}|^2 \rangle & 0 \\ \langle |S_{hv}|^2 \rangle & 0 & 3\langle |S_{hv}|^2 \rangle \end{bmatrix} = f_s \boldsymbol{C}_s + f_d \boldsymbol{C}_d \tag{3.26}$$

Then, the Equation (3.25) becomes the following set of three remaining equations which have

four unknowns, that is,

$$\langle |S_{hh}|^2 \rangle' = f_s |\beta_s|^2 + f_d |\alpha_d|^2, \tag{3.27a}$$

$$\langle |S_{vv}|^2 \rangle' = f_s + f_d, \tag{3.27b}$$

$$\langle |S_{hh} S_{vv}^*| \rangle' = f_s \beta_s + f_d \alpha_d, \tag{3.27c}$$

where $[\cdot]'$ means the quantity after the subtraction of the volume scattering component. To determine the remaining unknowns, the following assumption is made. If the residual co-polarized phase is closer to zero than π, we assume that the surface scattering component is dominant, and the constant α_d is fixed to $\alpha_d = -1$ (double-bounce scattering). Otherwise, we assume that the double-bounce component is dominant and the constant β_s is set to $\beta_s = 1$ (surface scattering). Then, we can solve the other components from Equation (3.27)

3.3.2 Yamaguchi Decomposition

As an extension of FDD, Yamaguchi et al. added the fourth component to Equation (3.23). The model can be described as

$$\langle \boldsymbol{C}_{(h,v)} \rangle = f_s \boldsymbol{C}_s + f_d \boldsymbol{C}_d + f_v \boldsymbol{C}_v + f_c \boldsymbol{C}_c, \tag{3.28}$$

where the additional matrix $\boldsymbol{C}_c$ takes one of the following two forms:

$$\boldsymbol{C}_c^R = \frac{1}{4} \begin{bmatrix} 1 & j\sqrt{2} & -1 \\ -j\sqrt{2} & 2 & j\sqrt{2} \\ -1 & -j\sqrt{2} & 1 \end{bmatrix}, \quad \boldsymbol{C}_c^L = \frac{1}{4} \begin{bmatrix} 1 & -j\sqrt{2} & -1 \\ j\sqrt{2} & 2 & -j\sqrt{2} \\ -1 & j\sqrt{2} & 1 \end{bmatrix}. \tag{3.29}$$

Both of these two matrices states that the cross-products $\langle S_{hh} S_{vv}^* \rangle$ and $\langle S_{hv} S_{vv}^* \rangle$ are purely imaginary numbers. Since this might not true for real observed images, Yamaguchi et al. suggested to use the following helix scattering model:

$$\frac{f_c}{4} = \frac{1}{2} \left| \mathrm{Im} \left\{ \langle S_{hh} S_{vv}^* \rangle + \langle S_{hv} S_{vv}^* \rangle \right\} \right|. \tag{3.30}$$

The helix scattering model $\boldsymbol{C}_c$ in Equation (3.28) is determined via

$$\boldsymbol{C}_c = \begin{cases} \boldsymbol{C}_c^R & \text{for } \mathrm{Im}\left\{\langle S_{hh}S_{vv}^*\rangle + \langle S_{hv}S_{vv}^*\rangle\right\} > 0, \\ \boldsymbol{C}_c^L & \text{otherwise.} \end{cases} \tag{3.31}$$

If we assume that the volume component in Equation (3.28) is modeled by uniformly oriented wires, we find from Equation (3.28) that the following five equations with six unknowns:

$$\langle |S_{hh}|^2 \rangle = f_s|\beta_s|^2 + f_d|\alpha_d|^2 + \frac{3}{8}f_v + \frac{1}{4}f_c, \tag{3.32a}$$

$$\langle |S_{hv}|^2 \rangle = \frac{1}{8}f_v + \frac{1}{4}f_c, \tag{3.32b}$$

$$\langle |S_{vv}|^2 \rangle = f_s + f_d + \frac{3}{8}f_v + \frac{1}{4}f_c, \tag{3.32c}$$

$$\langle S_{hh}S_{vv}^* \rangle = f_s\beta_s + f_d\alpha_d + \frac{1}{8}f_v - \frac{1}{4}f_c, \tag{3.32d}$$

$$\frac{1}{2}\left|\mathrm{Im}\left\{\langle S_{hh}S_{hv}^*\rangle + \langle S_{hv}S_{vv}^*\rangle\right\}\right| = \frac{f_c}{4}. \tag{3.32e}$$

From the above Equation (3.32e), we find

$$f_c = 2\left|\mathrm{Im}\left\{\langle S_{hh}S_{vv}^*\rangle + \langle S_{hv}S_{vv}^*\rangle\right\}\right|. \tag{3.33}$$

Also from Equation (3.32b), we can write the volume scattering component f_v

$$f_v = 8\left(\langle |S_{hv}|^2 \rangle - \frac{f_c}{4}\right) \tag{3.34}$$

Then, one can subtract the helix scattering and volume scattering components from Equation (3.28) as it is similarly done in the Freeman-Durden decomposition which is described in Section 3.3.1 or [5], that is,

$$f_s\boldsymbol{C}_s + f_d\boldsymbol{C}_d = \langle \boldsymbol{C}_{(h,v)} \rangle - \frac{f_v}{8}\begin{bmatrix} 3 & 0 & 1 \\ 0 & 2 & 0 \\ 1 & 0 & 3 \end{bmatrix} - \frac{f_c}{4}\begin{bmatrix} 1 & \pm j\sqrt{2} & -1 \\ \mp j\sqrt{2} & 2 & \pm j\sqrt{2} \\ -1 & \mp j\sqrt{2} & 1 \end{bmatrix}. \tag{3.35}$$

Moreover Yamaguchi et al. proposed the following covariance matrices for horizontally or

vertically oriented wire distribution [6]:

$$\boldsymbol{C}_v^H = \frac{1}{15}\begin{bmatrix} 8 & 0 & 2 \\ 0 & 4 & 0 \\ 2 & 0 & 3 \end{bmatrix}, \quad \boldsymbol{C}_v^V = \frac{1}{15}\begin{bmatrix} 3 & 0 & 2 \\ 0 & 4 & 0 \\ 2 & 0 & 8 \end{bmatrix}, \tag{3.36}$$

where $\boldsymbol{C}_v^H$ and $\boldsymbol{C}_v^V$ are the model for vertically and horizontally distributed wire, respectively. These matrices are derived by assuming the cosine-squared distribution of wire orientation angle around either vertical or horizontal directions.

For the horizontal case, we have the following set of equations from Equation (3.28):

$$\langle |S_{hh}|^2 \rangle = f_s|\beta_s|^2 + f_d|\alpha_d|^2 + \frac{8}{15}f_v + \frac{1}{4}f_c, \tag{3.37a}$$

$$\langle |S_{hv}|^2 \rangle = \frac{2}{15}f_v + \frac{1}{4}f_c, \tag{3.37b}$$

$$\langle |S_{vv}|^2 \rangle = f_s + f_d + \frac{3}{8}f_v + \frac{1}{4}f_c, \tag{3.37c}$$

$$\langle S_{hh}S_{vv}^* \rangle = f_s\beta_s + f_d\alpha_d + \frac{3}{15}f_v - \frac{1}{4}f_c, \tag{3.37d}$$

$$\frac{1}{2}\left|\mathrm{Im}\left\{\langle S_{hh}S_{hv}^* \rangle + \langle S_{hv}S_{vv}^* \rangle\right\}\right| = \frac{f_c}{4}. \tag{3.37e}$$

The helix scattering component f_c is determined via Equation (3.33), and the corresponding volume scattering component f_v is

$$f_v = \frac{15}{2}\left(\langle |S_{hv}|^2 \rangle - \frac{f_c}{4}\right). \tag{3.38}$$

Then, the surface and double-bounce scattering component is derived from the Freeman-Durden approach [5] after making the following subtraction:

$$f_s\boldsymbol{C}_s + f_d\boldsymbol{C}_d = \langle \boldsymbol{C}_{(h,v)} \rangle - \frac{f_v}{15}\begin{bmatrix} 8 & 0 & 2 \\ 0 & 4 & 0 \\ 2 & 0 & 3 \end{bmatrix} - \frac{f_c}{4}\begin{bmatrix} 1 & \pm j\sqrt{2} & -1 \\ \mp j\sqrt{2} & 2 & \pm j\sqrt{2} \\ -1 & \mp j\sqrt{2} & 1 \end{bmatrix}. \tag{3.39}$$

Similarly, for the case of vertical oriented model $\boldsymbol{C}_v^V$, the helix scattering component f_c is determined by Equation (3.33), and the corresponding volume scattering component f_v is derived from Equation (3.38). The surface and double-bounce scattering components are determined

after making the following subtraction:

$$f_s \boldsymbol{C}_s + f_d \boldsymbol{C}_d = \langle \boldsymbol{C}_{(h,v)} \rangle - \frac{f_v}{15} \begin{bmatrix} 3 & 0 & 2 \\ 0 & 4 & 0 \\ 2 & 0 & 8 \end{bmatrix} - \frac{f_c}{4} \begin{bmatrix} 1 & \pm j\sqrt{2} & -1 \\ \mp j\sqrt{2} & 2 & \pm j\sqrt{2} \\ -1 & \mp j\sqrt{2} & 1 \end{bmatrix}. \tag{3.40}$$

To determine which model to employ, i.e. uniform, horizontal, or vertical wire distribution, Yamaguchi et al. suggested to use the ratio of the vv to hh backscattering coefficients. The following steps for Yamaguchi decomposition algorithm describes the criterion for the selection of volume scattering model.

Step 1. *Free from the selection of volume scattering model, estimate the helix scattering component from Equation (3.33).*

Step 2. *We denote the ratio of hh to vv backscattering coefficient as HH/VV. The following criterion is used to estimate the volume scattering component.*

Case 1. *For (-2 dB < VV/HH < +2 dB), use Equation (3.34)*

Case 2. *For (-2 dB > VV/HH > +2 dB), use Equation (3.38)*

Step 3. *Now the helix and volume scattering component is fixed, and the following subtraction can be made.*

Case 1. *For (-2 dB < VV/HH < +2 dB), use Equation (3.35)*

Case 2. *For (-2 dB < VV/HH), use Equation (3.39)*

Case 3. *For (VV/HH > +2 dB), use Equation (3.40)*

Step 4. *Determine the surface and double-bounce scattering components from Equation (3.27) and the procedure in Freeman-Durden decomposition [5].*

3.3.3 Adaptive Model-Based Decomposition

The main idea of Yamaguchi decomposition is introducing the additional volume scattering component which can be adaptively selected. However, the decomposition scheme only has the finite number of the volume scattering models. To incorporate more accurate volume scattering models, Arii et al. proposed the adaptive model-based decomposition (AMBD) [27]. In AMBD, the volume scattering model is adaptively chosen from an infinite number of models represent various types of vegetation. The detail of this algorithm is presented in [27].

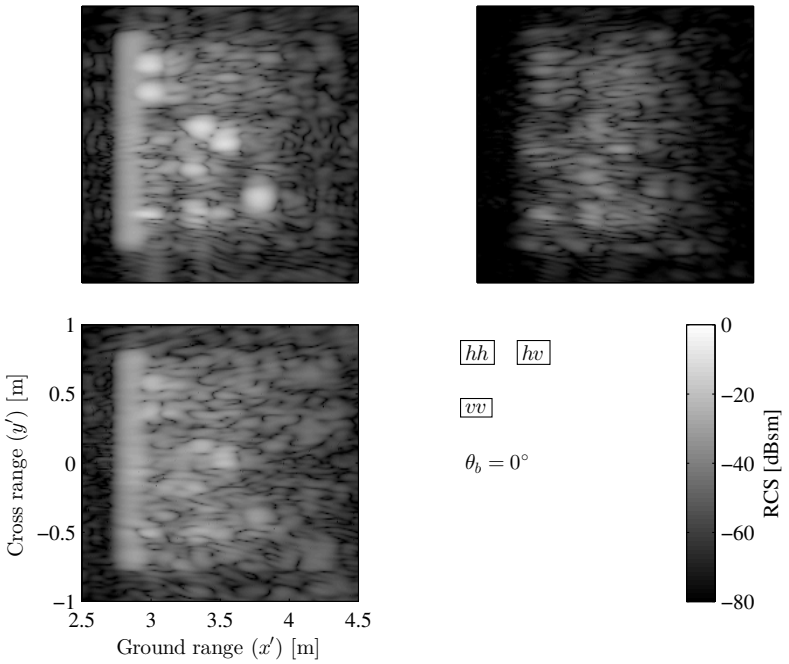

Figure 3.3: SAR image for each polarization channel (forest model).

3.4 Comparison of Decomposition Algorithms

So far, we have shown three types of model-based decomposition algorithms. The aim of this section is comparing those decomposition schemes qualitatively by applying the algorithms to the obtained SAR images which are summarized in the end of Chapter 2. The measured data of the building model and the forest model is used for this purpose.

3.4.1 Building Model

The measured SAR data of the building model at the highest radar altitude of 1.7 m is employed for our analysis. The pixel size of the ground range image is 1 cm $\times$ 1 cm, and the averaged covariance matrices are calculated from 5×5 adjacent pixels.

Figure 3.3 and 3.4 show the obtained SAR image and the Pauli decomposed image for the building model. The building wall facing toward the radar LOS direction is clearly appeared in the hh-polarized image while the cross-polarized image is much weaker than that of the co-polarized image. By utilizing the Pauli decomposition, scattering from the ground plate edge is shown as the P_s component, while the double-bounce scattering between the ground and building walls are imaged as P_d component. Because the model structure is simple, the Pauli

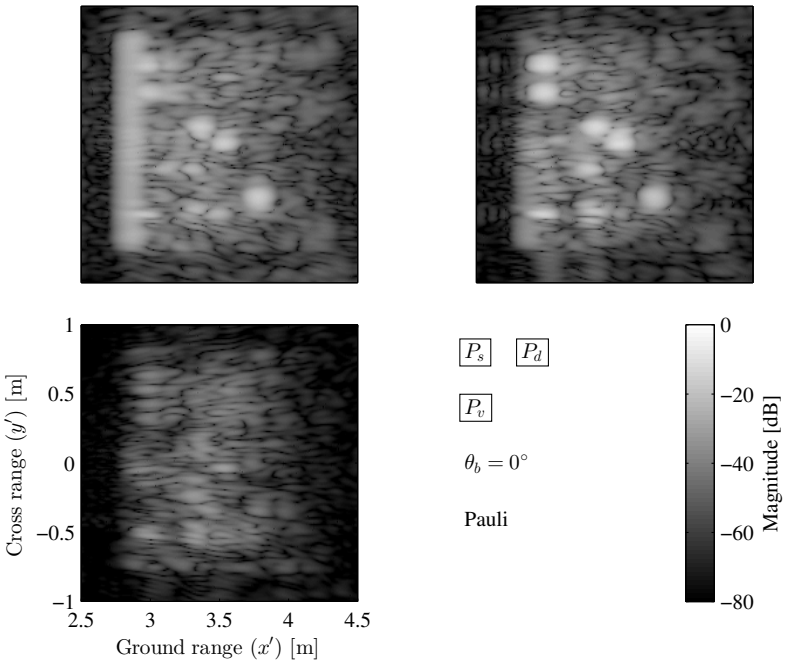

Figure 3.4: Pauli decomposition (forest model).

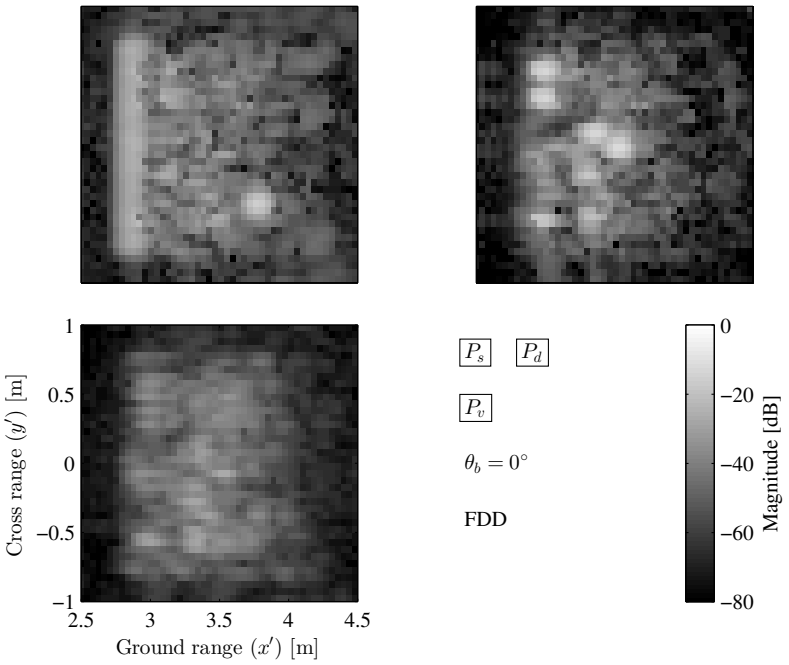

Figure 3.5: Freeman-Durden decomposition (forest model).

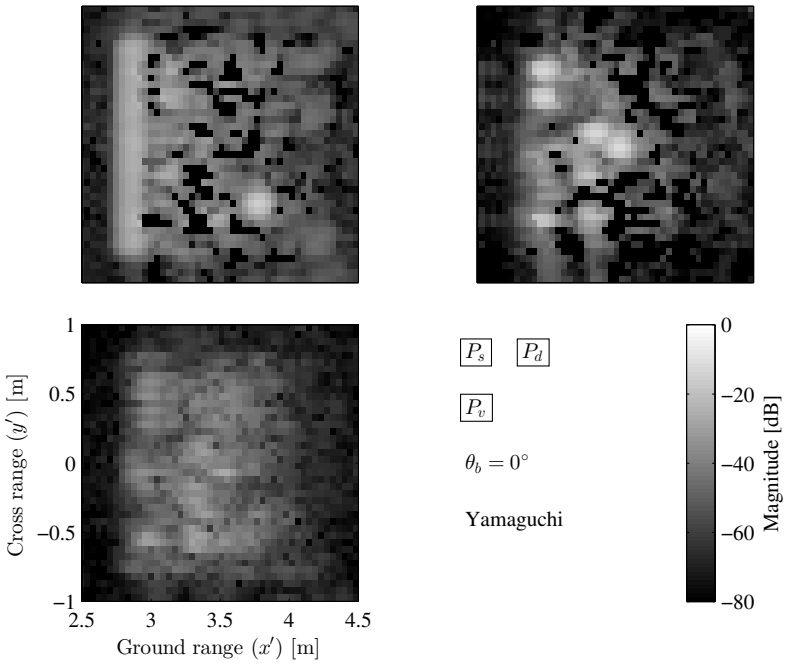

Figure 3.6: Yamaguchi decomposition (forest model).

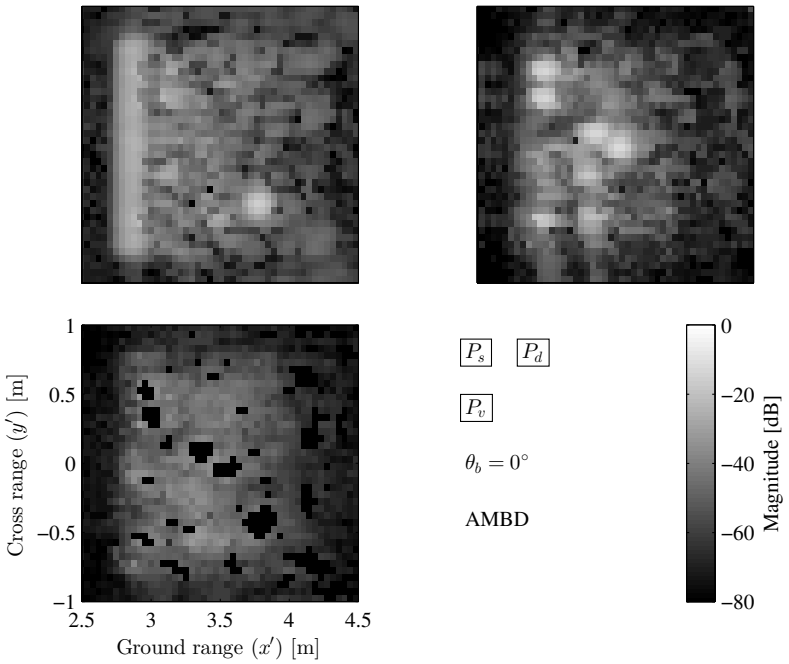

Figure 3.7: Adaptive model-based decomposition (forest model).

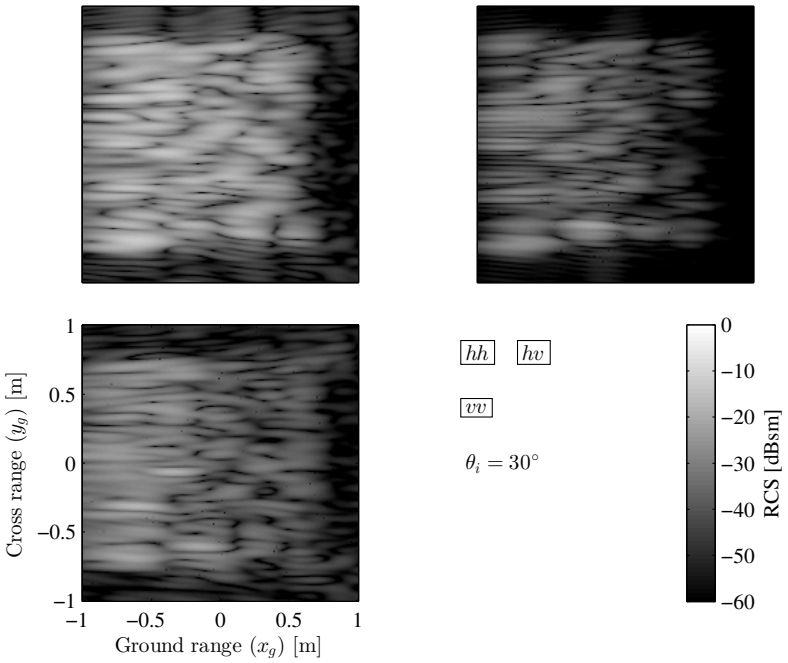

Figure 3.8: SAR image for each polarization channel (forest model).

decomposition works well for this model.

Figure 3.5, 3.6, and 3.7 are the model-based polarimetric decomposition results, that is, the Freeman-Durden decomposition, the Yamaguchi decomposition, and the adaptive model-based decomposition. These images are similar to the Pauli decomposed image. Because the main difference of these model-based decomposition algorithms is the choice of the volume scattering component only slight difference can be observed in the building model.

3.4.2 Forest Model

Though multiple incidence angle SAR images in different moisture conditions are available, we restrict our discussion to the analysis of a single incidence angle image. The discussion on how the moisture condition of forest and the incidence angle affects to the PolSAR image is studied in Chapter 4. The pixel size of the ground range image is 1 cm $\times$ 1 cm, and the averaged covariance matrices are calculated from 5×5 adjacent pixels.

Figure 3.8 and 3.9 are the reconstructed PolSAR image and the Pauli decomposed image, respectively. As mentioned in Chapter 2, the scattering from this forest model is expected to be dominated by the double-bounce scattering between the ground and trunk surfaces. However,

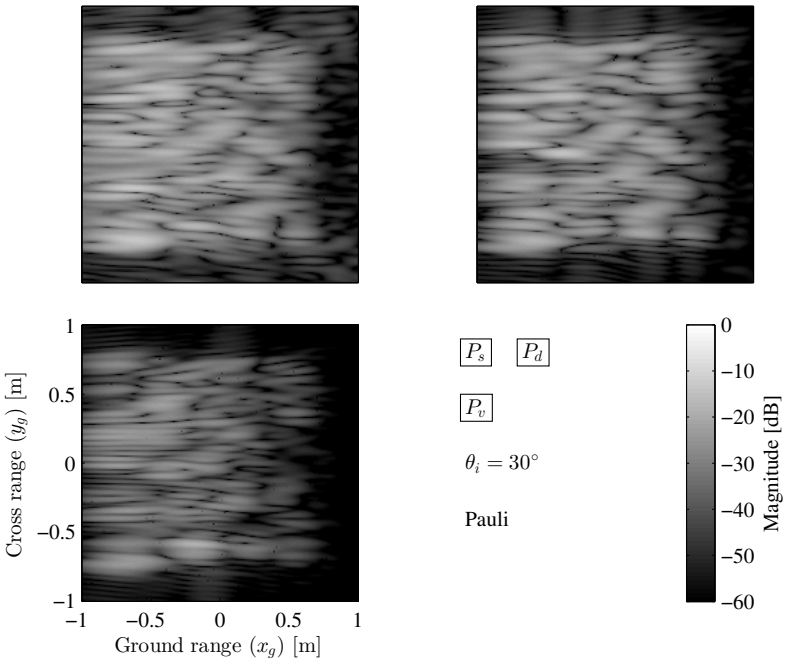

Figure 3.9: Pauli decomposition (forest model).

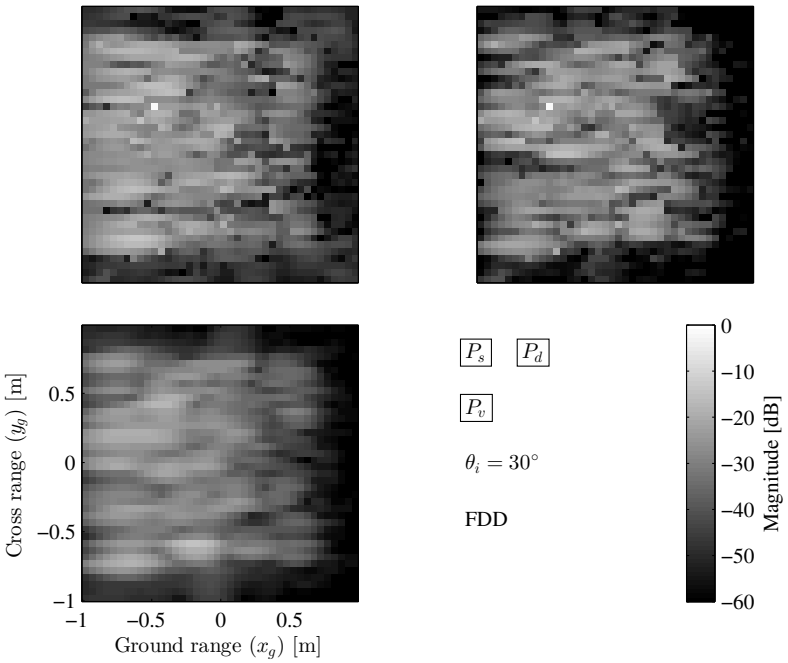

Figure 3.10: Freeman-Durden decomposition (forest model).

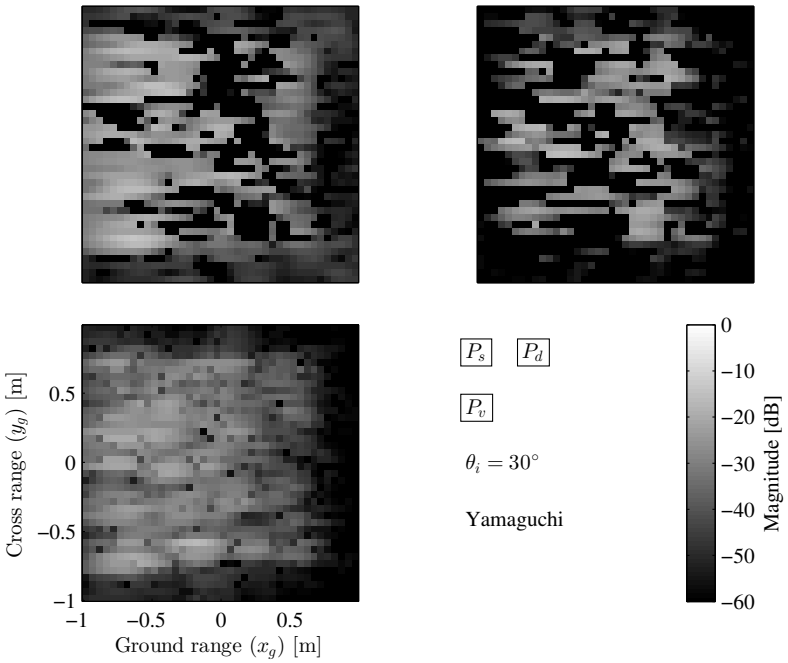

Figure 3.11: Yamaguchi decomposition (forest model).

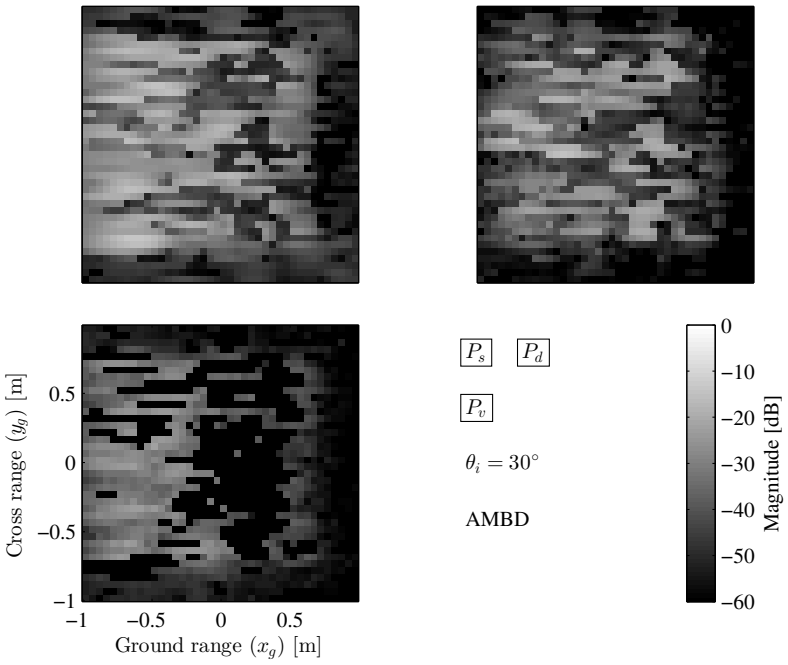

Figure 3.12: Adaptive model-based decomposition (forest model).

the P_s and P_d component of the Pauli decomposition show the similar intensity, and thus we can see that our assumption in the Pauli decomposition does not works well for the forested terrain observation.

Figure 3.10, 3.11, and 3.12 are the model-based decomposition results, that is, the Freeman-Durden decomposition, the Yamaguchi decomposition, and the adaptive model-based decomposition, respectively. In FDD image, all the decomposed components have similar image intensity. Comparing to the FDD image and Yamaguchi decomposed image, the volume scattering component of the Yamaguchi decomposed image seems to be dominant, due to the introduction of the additional volume scattering model. However, both of these results are unexpected since the forest model consists of the simple orthogonal structures.

For AMBD image in Figure 3.12, volume scattering component is significantly suppressed and the decomposed image is dominated by the surface and double-bounce scattering component. This fact implies that the conventional FDD and Yamaguchi decomposition overestimate the volume scattering component.

3.5 Summary of This Chapter

In this chapter, the basics of PolSAR image analysis is presented by introducing the several polarimetric quantities for further analysis. The PolSAR is a simple extension of the single-polarized SAR described in Chapter 2, and similar reconstruction algorithm can be used to form the SAR image for each polarization channel. The Sinclair scattering matrix is defined for each image pixel, and further polarimetric analysis is base on this quantity.

The fundamentals of polarimetric model-based decomposition algorithms are described, and we compare the different decomposition algorithms qualitatively by applying these to the measured SAR images. By this comparison, AMBD shows the most preferable decomposition results for the forest model, because the scattering from this forest model is expected to be dominated by the double-bounce scattering from the ground and vertical trunks, and AMBD predicts that the double-bounce component is dominant.

Chapter 4

Multiple Angle SAR

Introduction

This chapter presents the analysis of multiple angle SAR (MA-SAR) images. So far the basic concepts of SAR image reconstruction and its polarimetric analysis is established. Though the introduction of polarimetric concepts such as the model-based decomposition schemes tell us the great details of the observing targets, we are still missing the important information, that is, the *angular dependence* of the observing scene. For example, as shown in Section 3.4, model-based decomposition of SAR image of a highly-directive target such as a man-made structure results in a completely different image when the target is observed from different azimuthal angles. Therefore, to deal with the diversity of the observing scene, we must investigate the effect of the angular dependence. In this Chapter, we discuss on the incidence angle dependence of the SAR images. By utilizing multiple angle angle SAR image acquired in an anechoic chamber, we show that the SAR images of forested terrain highly depend on the incidence angle. Also we present the effect of forest moisture condition to the multiple angle SAR image, and propose the index to infer the moisture condition of forested terrain.

Outline

The discussion starts with the definition of the observation scenario of MA-SAR in Section 4.1. In Section 4.2, we describe how incidence angle affects the scattered wave by the classical Fresnel reflection and transmission coefficients. Then, Section 4.4 shows the incidence angle dependence of forest observation, and we propose a simple index to estimate forest moisture condition.

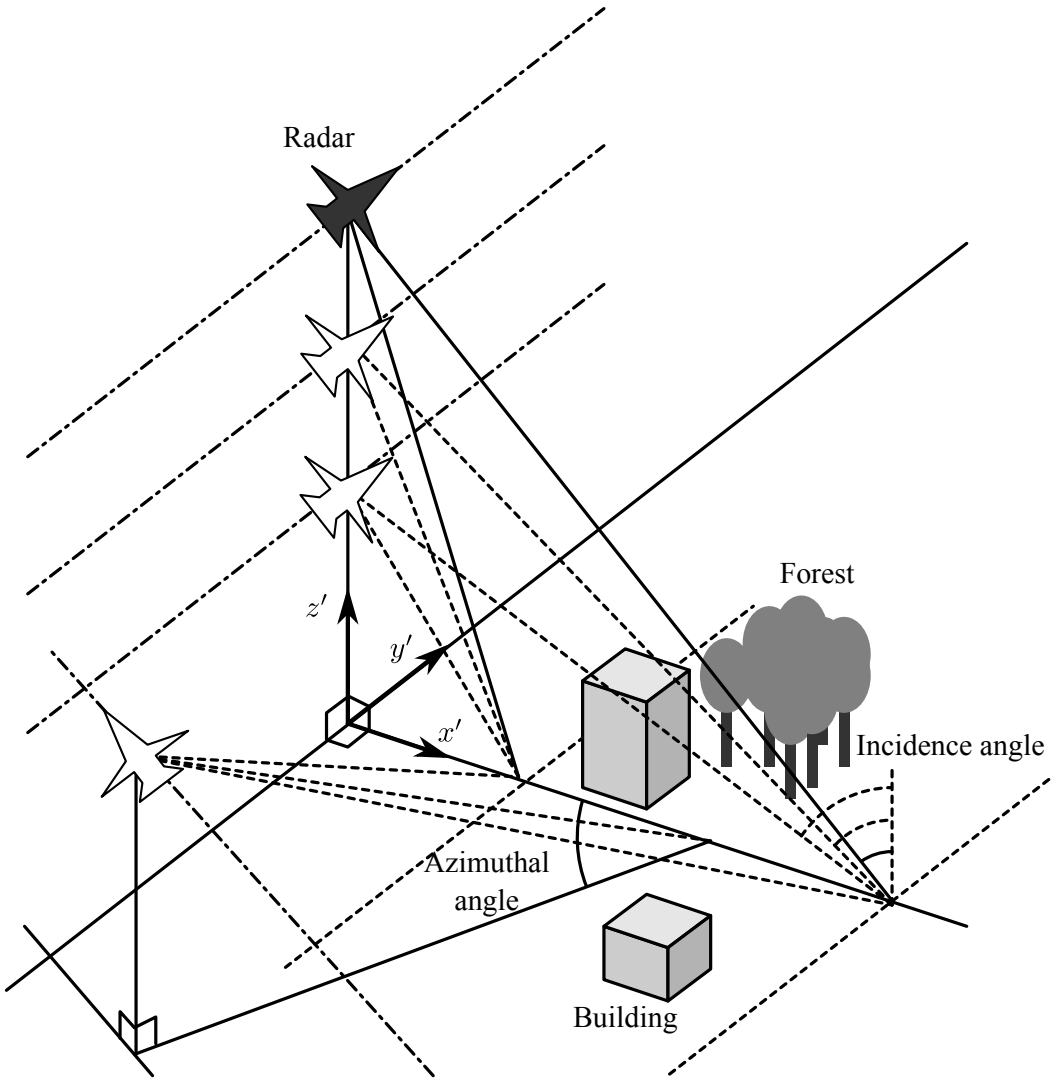

Figure 4.1: MA-SAR observation scenario.

4.1 Observation Scenario

The MA-SAR observation scenario is depicted in Figure 4.1. In MA-SAR measurement, we can vary an incidence angle as well as an azimuthal angle to collect the backscattering of the target from various angles. The image reconstruction is achieved by the algorithms presented in Chapter 2, and polarimetric extension is also possible as shown in Chapter 3. Similar to the previous chapter, we denote the reconstructed polarimetric SAR image at the pixel location (x_i, y_j) by $f_{\beta\alpha}(x_i, y_j)$, where $\alpha, \beta \in \{h, v\}$ represent the transmitted and received polarization

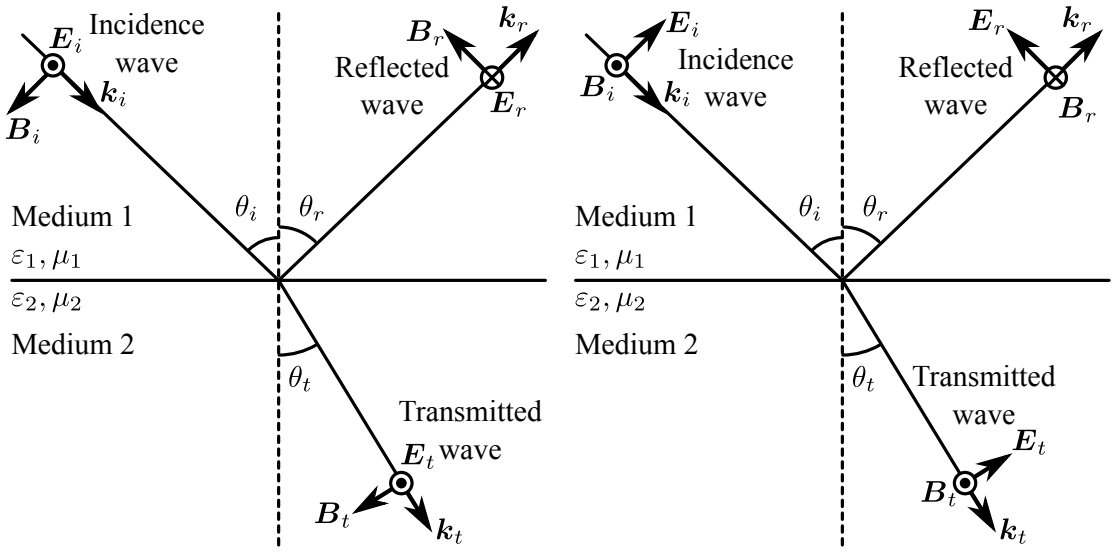

Figure 4.2: Reflection and transmission of a plane wave incidence at a flat dielectric interface.

channels, respectively.

4.2 Effect of Incidence Angle

We present how radar incidence angle affects to the resultant SAR image using a simple dielectric surface model as shown in Figure 4.2. A plane wave impinges a flat dielectric interface at an incidence angle θ_i, and a part of this wave is reflected at the interface, while the another part transmits the interface. We denote medium permittivity as ε_1 and ε_2, and permeability as μ_1 and μ_2, respectively. We denote the magnitude of the incidence, reflected, and transmitted electric vector by E_i, E_r and E_t.

4.2.1 Fresnel Coefficient

We assume that the dielectric medium is non-magnetic substance, that is, $\mu_1 \approx 1$ and $\mu_2 \approx 1$. Classical electromagnetic theory states that, for the H-polarized case shown in Figure 4.2 (a),

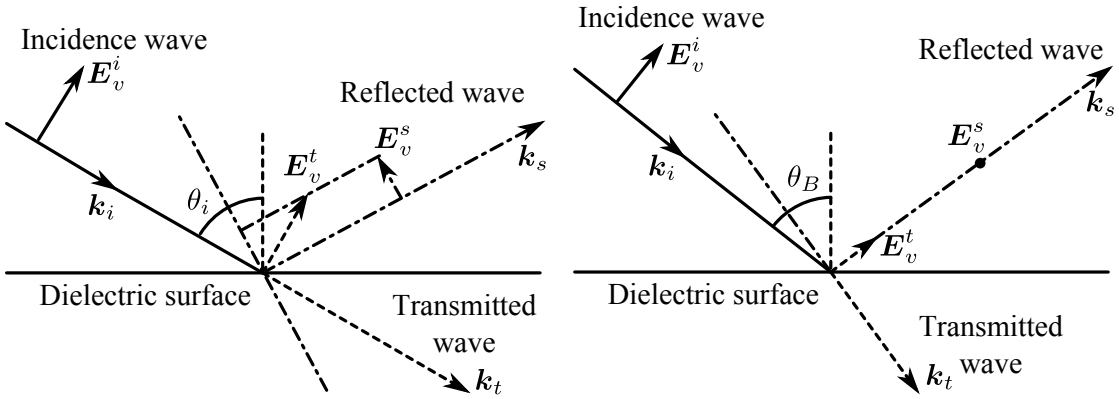

(a) Generic incidence. (b) Incidence at Brewster angle.

Figure 4.3: Illustration of Brewster angle effect.

the transmission and reflection coefficient are respectively expressed by

$$r_H(\theta_i;\varepsilon_r) = \frac{E_r}{E_i} = \frac{\cos\theta_i - \sqrt{\varepsilon_r - \sin^2\theta_i}}{\cos\theta_i + \sqrt{\varepsilon_r - \sin^2\theta_i}}, \tag{4.1a}$$

$$t_H(\theta_i;\varepsilon_r) = \frac{E_t}{E_i} = \frac{2\cos\theta_i}{\cos\theta_i + \sqrt{\varepsilon_r - \sin^2\theta_i}}, \tag{4.1b}$$

where ε_r is the medium permittivity defined via

$$\varepsilon_r = \frac{\varepsilon_2}{\varepsilon_1}. \tag{4.2}$$

Similarly, for the V-polarized case shown in Figure 4.2 (b) we have

$$r_V(\theta_i;\varepsilon_r) = \frac{E_r}{E_i} = \frac{\varepsilon_r\cos\theta_i - \sqrt{\varepsilon_r - \sin^2\theta_i}}{\varepsilon_r\cos\theta_i + \sqrt{\varepsilon_r - \sin^2\theta_i}}, \tag{4.3a}$$

$$t_V(\theta_i;\varepsilon_r) = \frac{E_t}{E_i} = \frac{2\sqrt{\varepsilon_r}\cos\theta_i}{\varepsilon_r\cos\theta_i + \sqrt{\varepsilon_r - \sin^2\theta_i}}. \tag{4.3b}$$

These coefficients are known as *Fresnel coefficients* and functions of the incidence angle θ_i and the medium relative permittivity ε_r.

4.2.2 Brewster Angle

The Fresnel reflection coefficient for V-polarize case defined in Equation (4.3a) has an important characteristic. When an incidence angle satisfies the condition

$$\tan\theta_i = \sqrt{\varepsilon_r}, \tag{4.4}$$

The V-polarized reflection coefficient Equation (4.3a) becomes zero; the incidence wave perfectly transmits the interface, and no reflection can be observed at this angle. This angle is known as *Brewster angle* or *polarization angle*, and we denote this angle as θ_B. Rigorously, the Brewster angle θ_B exists provided that the medium relative permittivity ε_r is a pure real quantity. Otherwise, the reflection coefficient drops off around the Brewster angle. If one has a knowledge of the Brewster angle θ_B, one can readily invert the medium relative permittivity ε_r, though direct measurement of Brewster angle using SAR system might be difficult. As it is discussed later, estimating the dielectric constant is important for soil moisture estimation, because dielectric constant of soil surfaces depends on its moisture content.

The schematic description of the Brewster angle is shown in Figure 4.3. In general, a V-polarized incident wave is reflected and transmitted at the dielectric interface as depicted in Figure 4.3 (a), and the intensity of the transmission E_t and reflection E_r can be described by the Fresnel coefficients given in Equation (4.3). The reflected electric vector $\boldsymbol{E}_V^r$ is the component of the transmitted electric vector $\boldsymbol{E}_V^t$ along the orthogonal line of reflected vector k_r. However, at the Brewster angle θ_B shown in 4.3 (b), the transmitted electric vector $\boldsymbol{E}_V^t$ is parallel with the reflected wave vector $\boldsymbol{k}_r$; the reflected electric vector $\boldsymbol{E}_V^r$ has no orthogonal component to the reflected wave vector $\boldsymbol{k}_r$, and therefore no reflection can be observed at the Brewster angle.

From the above discussion, the scattering of a dielectric object depends on the radar incidence angle, especially the V-polarized case, even if the object has a simple structure such as flat surface as shown in Figure 4.3. In other words, the V-polarized scattering conveys the information related to the medium permittivity.

4.2.3 Brewster Angle for Double-Bonce Case

In the previous discussion, we have shown that the scattering of V-polarized incident wave strongly depends on not only the medium permittivity but also the incidence angle. To extend this idea to the monostatic radar case, we consider the two situations as shown in Figure 4.4. Both of the cases have a pair of orthogonal surfaces, and an incidence wave strikes the bottom surface

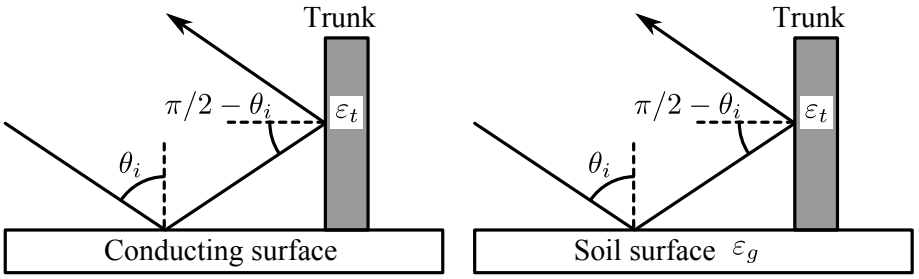

(a) Conducting ground surface. (b) Dielectric ground surface.

Figure 4.4: Geometry of double-bounce between ground surface and trunk surface.

at an incidence angle θ_i. Clearly, the scattering mechanism is dominated by the double-bounce scattering caused between the ground surface and the another dielectric surface.

In Figure 4.4, a flat dielectric object stands on a flat conducting surface. In this case, the backscattering coefficient for hh-polarized case σ_{hh} and vv-polarized case σ_{vv} can be described as the Fresnel reflection coefficient defined in Equation (4.3), that is,

$$\sigma_{hh} = r_H\left(\frac{\pi}{2} - \theta_i\right), \tag{4.5a}$$

$$\sigma_{vv} = r_V\left(\frac{\pi}{2} - \theta_i\right). \tag{4.5b}$$

The only one Brewster angle for this case θ_B^t exists and is expressed as

$$\theta_B^t = \frac{\pi}{2} - \tan^{-1}\sqrt{\varepsilon_r^t}. \tag{4.6}$$

Replacing the conducting ground surface as the dielectric surface shown in Figure 4.4, the reflection can be described by the two Fresnel reflection coefficients as

$$\sigma_{hh} = r_H\left(\theta_i;\varepsilon_g\right) r_H\left(\frac{\pi}{2} - \theta_i;\varepsilon_t\right), \tag{4.7a}$$

$$\sigma_{vv} = r_V\left(\theta_i;\varepsilon_g\right) r_V\left(\frac{\pi}{2} - \theta_i;\varepsilon_t\right). \tag{4.7b}$$

In addition to the Brewster angle defined in Equation (4.6), one more Brewster angle for the ground surface appears at

$$\theta_B^g = \tan^{-1}\sqrt{\varepsilon_r^g}. \tag{4.8}$$

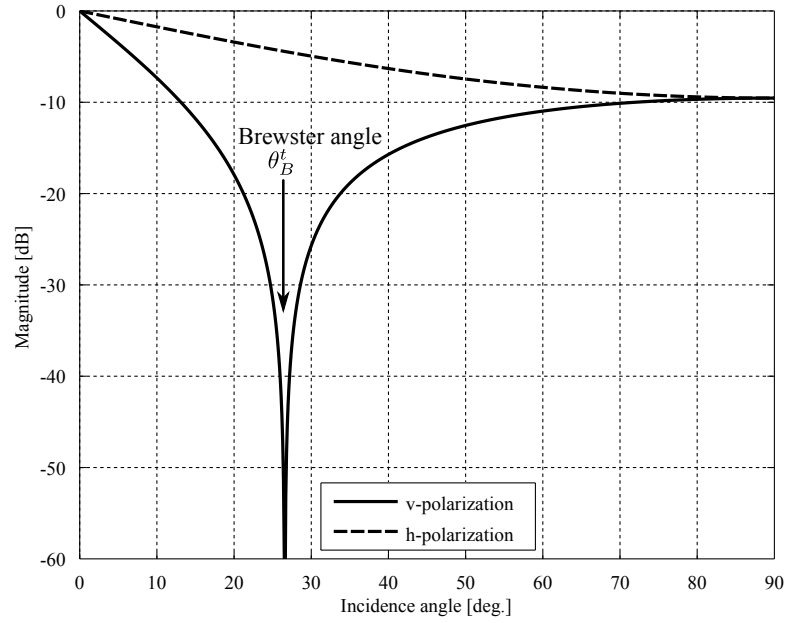

(a) Magnitude.

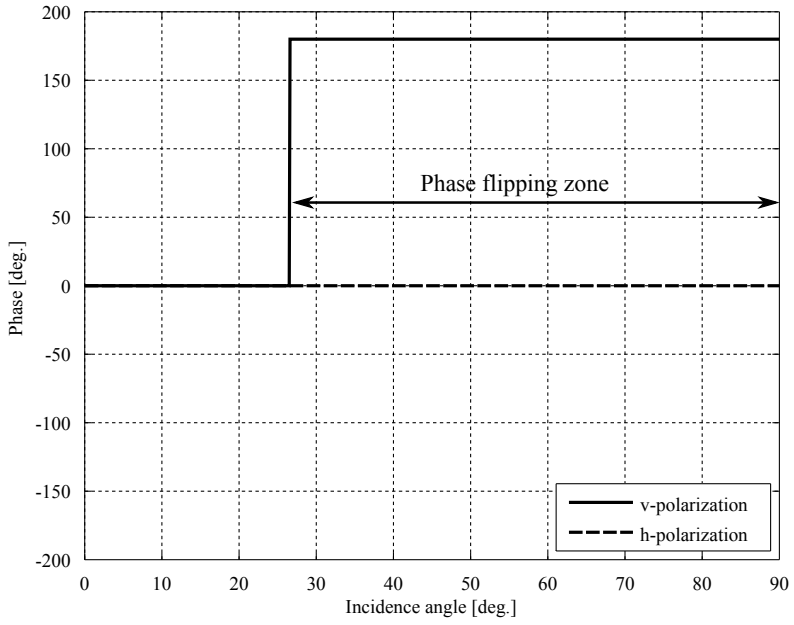

(b) Phase.

Figure 4.5: Fresnel reflection coefficient (conducting ground surface, $\varepsilon_v = 4$).

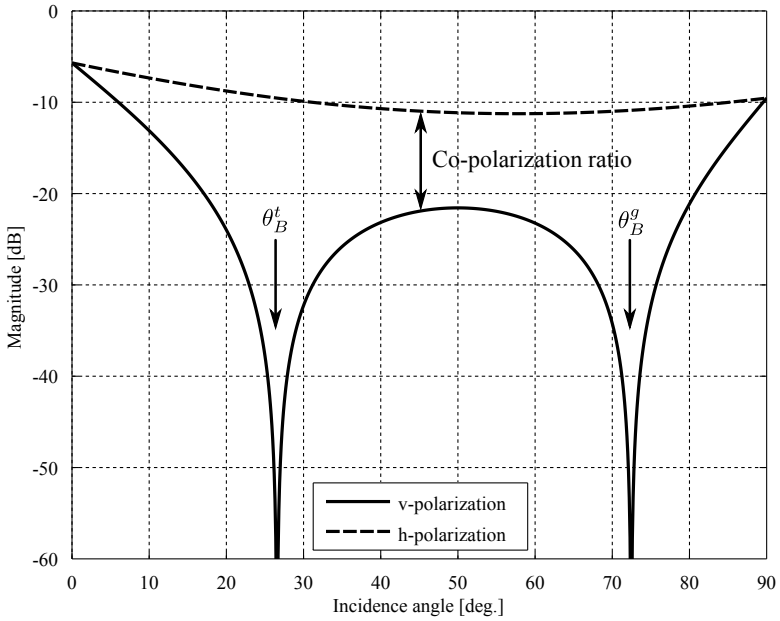

(a) Magnitude.

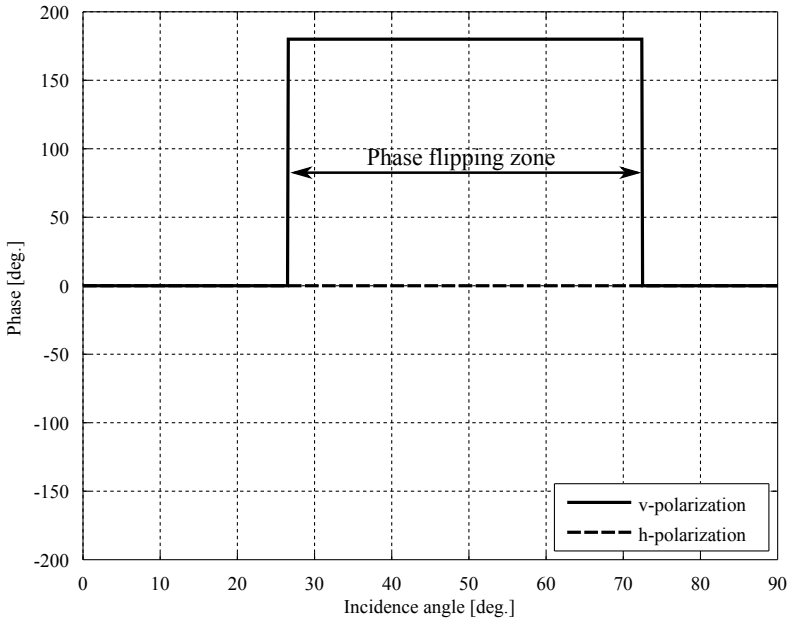

(b) Phase.

Figure 4.6: Fresnel reflection coefficient ($\varepsilon_g = 10, \varepsilon_v = 4$).

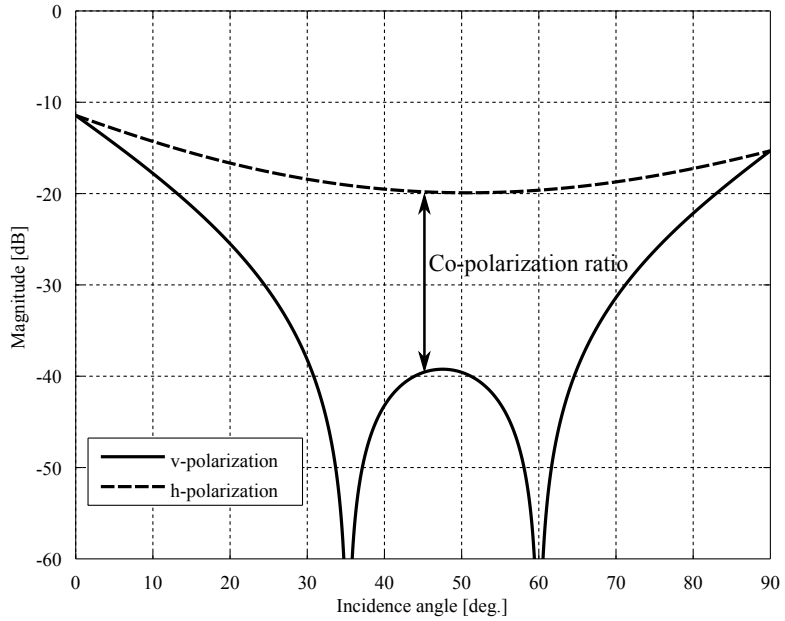

Figure 4.7: Fresnel reflection coefficient ($\varepsilon_g = 3, \varepsilon_v = 2$).

4.2.4 Numerical Example

A numerical example of the magnitude and phase of the double-bounce Fresnel reflection coefficient are respectively shown in Figure 4.5 (a) and (b) for the case of conducting ground surface. Similarly, Figure 4.6 (a) and (b) show the case of dielectric ground surface. The dielectric constants are set to $\varepsilon_g = 10$ and $\varepsilon_v = 4$.

In Figure 4.5 (a), we can recognize the sharp dips due to the Brewster angle effect in the v-polarized magnitude while the h-polarized magnitude doest not vary significantly compared to the v-polarization. Because the ground surface is considered to be a conducting surface, only one dip at the Brewster angle for trunk surface can be observed. In addition, we can see that the v-polarized phase in Figure 4.5 (b) flips at the Brewster angle.

Let us move on to the second case, that is, both ground and trunk surface are dielectric surface. In this case, additional Brewster angle for the ground surface is appeared as shown in Figure 4.6 (a). Also from 4.6 (b), one more phase flipping occurs at the second Brewster angle. Because of this, the phase flipping zone is restricted between these two Brewster angles; when phase flipping occurs, one can notice that the incidence angle is between two Brewster angles.

The another notable characteristic of the double-bounce Fresnel reflection coefficient is the

ratio between h and v polarized coefficient. Figure 4.7 shows the double-bounce Fresnel reflection coefficient when the dielectric constants are set to smaller compared to the previous examples. The dielectric constants are $\varepsilon_g = 3$ and $\varepsilon_v = 2$ for this example, and comparing to Figure 4.6, one can notice that the co-polarization ratio around 45° becomes larger as the decrease of the dielectric constants. This fact implies that the co-polarization ratio is sensitive to the variation of the dielectric constants, and we can use the ratio as an indicator of the permittivity of the target which has an orthogonal structure.

4.3 Soil Moisture Effects of Forested Terrain

In Section 4.2, we have shown that the significance of the incidence angle and medium permittivity. As mentioned in the previous discussion, the variation of moisture content corresponds to the variation of permittivity. This section utilizes the concept of the double-bounce Fresnel reflection coefficient to estimate soil moisture condition of forested terrain.

Soil moisture is one of the key parameters to characterize the global climate system in numerous environmental studies, including hydrology, meteorology, and agriculture, since the flux of water in soil plays an important role in the hydrological cycle. Several satellite missions are being conducted or planned for the earth observation, some of which are specialized to provide global hydrological information [14]–[16].

The difficulty of soil moisture retrieval using PolSAR is that the radar observables usually do not have a straightforward interpretation. It is well-known that the radar backscatter is affected not only by terrain moisture content, but also by other surface characteristics such as roughness, correlation length, local topography or incidence angle, and so forth [17, 18]. In addition, the perturbation in the backscatter due to vegetation complicates the problem exceedingly, as commonly reported that the sensitivity of the backscatter to soil moisture is degraded by vegetation cover.

The retrieval of soil moisture from radar imagery usually relies on an empirical relationship to convert the backscattering coefficient into volumetric soil moisture [21]–[23], and most of the algorithms are at their best when monitoring bare soil surface moisture. However soil moisture algorithms should be designed to compensate for the effects of vegetation cover as much as possible, since approximately 31% of the total land surface of the earth is occupied by forests [24], and the ratio reaches to more than 76% when taking other types of vegetation into account [25, 26]. Although some algorithms to deal with this problem have been proposed, they are still

subjected to investigation because the lack of sufficient quantitative validation.

To quantitatively examine how the moisture content affects the radar backscattering from forests, both surface characteristics and vegetation cover should be considered simultaneously. One effective approach is the utilization of microwave scattering models for vegetated terrain [27]–[29], and appropriate experimental validation under well-controlled conditions. In general, the scattering models can express arbitrary types and conditions of vegetated terrain without limitation by introducing several kinds of input parameters as a forward model. However, with the increase in the number of model inputs, model complexity also expands, and therefore deriving physical interpretations from the computation result, a complex mixture of several backscattering components, becomes a difficult task. Furthermore, experimental validation of such a complicated model is usually out of control since natural terrain has many uncertainties of surface conditions and vegetation structure, and indoor measurement has a number of practical limitations for constructing an experimental model.

Hence, from the perspective of understanding how terrain physical parameters affect the resultant backscattering, and to assist well-controlled experimental validation, it is essential to have a microwave scattering model with moderate complexity by which it is sufficient to describe the main contributors of vegetation backscattering. For this objective, we employ a simplified Discrete Scatterer Model (DSM) in which vegetation is considered as an assemblage of primitive scatterers [27], [28], which we expect the model to be convenient for both theoretical and experimental consideration. From both the simplified DSM and a series of experiments, it is shown that the co-polarization ratio can be an index to monitor the relative variation of forest moisture content. Since relative soil moisture is of much interest for climate system modeling [31], the co-polarization ratio can be an useful parameter to understand the global climate system from SAR imagery.

4.3.1 Soil and Vegetation Permittivity Model

This section provides permittivity models for soil and vegetation components, which are (semi-) empirically derived from various measurement data.

Permittivity Model for Soil

The permittivity model derived by Hallikainen et al. is summarized as follows. The relative permittivity of soil which contains percent sand and clay content of S_c and C_c, respectively, is

modeled by

$$\varepsilon_S = \varepsilon_s' + j\varepsilon_s'', \tag{4.9}$$

where ε_s' and ε_s'' are the real and imaginary part of the soil relative permittivity, respectively. These are determined via

$$\varepsilon_s' = (a_0' + a_1' S_c + a_2' C_c) + (b_0' + b_1' S_c + b_2' C_c) m_s + (c_0' + c_1' S_c + c_2' C_c) m_s^2, \tag{4.10}$$

$$\varepsilon_s'' = (a_0'' + a_1'' S_c + a_2'' C_c) + (b_0'' + b_1'' S_c + b_2'' C_c) m_s + (c_0'' + c_1'' S_c + c_2'' C_c) m_s^2, \tag{4.11}$$

where m_s is the volumetric moisture, and the other constants are given by

$$\begin{aligned} a_0' &= 2.862, \quad & a_1' &= -0.012, \quad & a_2' &= 0.001, \\ b_0' &= 3.803, \quad & b_1' &= 0.462, \quad & b_2' &= -0.341, \\ c_0' &= 119.006, \quad & c_1' &= -0.500, \quad & c_2' &= -0.633, \end{aligned} \tag{4.12}$$

and

$$\begin{aligned} a_0'' &= 0.356, \quad & a_1'' &= -0.003, \quad & a_2'' &= -0.008, \\ b_0'' &= 5.507, \quad & b_1'' &= 0.044, \quad & b_2'' &= -0.002, \\ c_0'' &= 17.753, \quad & c_1'' &= -0.313, \quad & c_2'' &= 0.206. \end{aligned} \tag{4.13}$$

Permittivity Model for Vegetation

Ulaby et al. developed a permittivity model for vegetation components described below. The vegetation relative permittivity ε_V can be modeled by

$$\varepsilon_v = \varepsilon_R + v_f \left(4.9 + \frac{75.0}{1 + jf/18} - j\frac{18\sigma_v}{f}\right) + v_b \left(2.9 + \frac{55.0}{1 + \sqrt{jf/0.18}}\right), \tag{4.14}$$

$$f = \frac{\omega}{2\pi} \cdot 10^{-9}, \tag{4.15}$$

$$S_s = 8.5, \tag{4.16}$$

$$\sigma_v = 0.16 S_s - 0.0013 S_s^2, \tag{4.17}$$

$$\varepsilon_R = 1.7 + 3.2 m_v + 6.5 M_V^2, \tag{4.18}$$

$$v_f = (0.82 m_v + 0.166) m_v, \tag{4.19}$$

$$v_b = \frac{31.4 m_v^2}{1 + 59.5 m_v^2}, \tag{4.20}$$

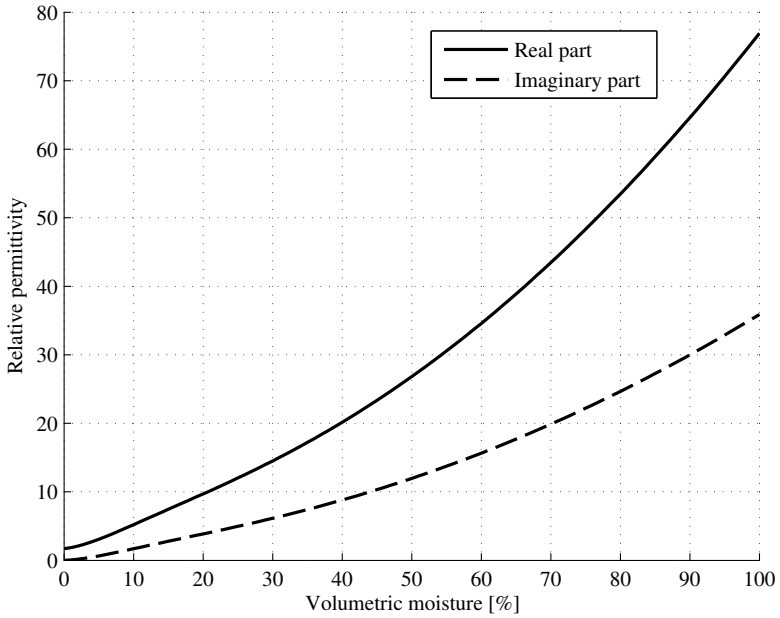

Figure 4.8: Calculated relative permittivity for vegetation.

where f is the frequency in gigahertz, and S_s is the percent salinity of the vegetation. The volumetric moisture is represented by m_v.

Numerical Example

The numerical example of the vegetation permittivity model is shown in Figure 4.8 in terms of volumetric moisture content. We can see that the relative permittivity increases as an increase of volumetric moisture content. Thus, once the relative permittivity of the target is obtained, one can estimate the moisture content from the relative permittivity.

4.4 Modeling of Forested Terrain

Many microwave scattering models [27]–[29] for forested terrain have been developed to better understand microwave interaction within forests, and to assist forest parameter retrieval from SAR imagery. A vast majority of them are dedicated to precisely simulate forest backscattering behavior, requiring many input parameters for which it is difficult to determine suitable values. However, for physical parameter inversion from SAR imagery, a microwave model should be designed so that the number of inputs is limited as little but sufficient to represent the main

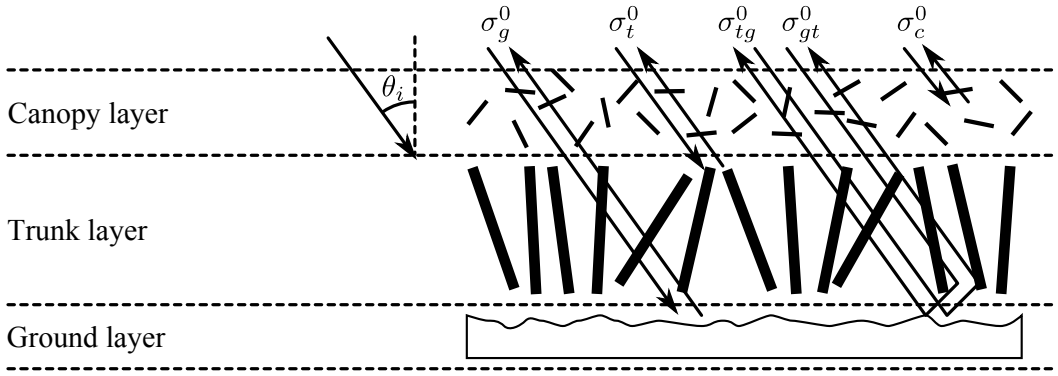

Figure 4.9: Generic DSM geometry.

scattering contributors of forested terrain as possible.

For this reason, we employ a Discrete Scatterer Model (DSM) [27] which is originally proposed by Durden et al. [28]. In this model, discrete canonical scatterers such as discs, cylinders, and needles can be used to represent vegetation components. In this study, further simplification is necessary to better understand an individual scattering behavior. The detailed description of the DSM used in this chapter is given in [27], and this section provides the brief explanation only.

As shown in Figure 4.9, the generic DSM is composed of a stack of layers containing canopy, trunk, and ground, in which the vegetation components are represented as a cloud of dielectric inclined cylinders so that its angular distribution obeys a prescribed probability density function (pdf). The ground layer is expressed as a rough dielectric surface with roughness parameters of root-mean-square (rms) height and correlation length. The model takes first-order scattering plus ground-trunk interaction into account, and other higher-order multiple scattering components are ignored by assuming that the vegetation components are sparsely distributed, and an incident wave is well attenuated during the multiple scattering process.

4.4.1 Model Simplification

To demonstrate how terrain physical parameters, particularly soil moisture, contribute to forest backscattering, it is necessary to simplify the above general model to isolate a individual scattering component.

When a radar uses L-band or P-band wavelength, which are commonly preferred in forest monitoring applications, to observe over forested terrain, an incident wave is supposed to penetrate the layers of canopy components to probe the physical characteristics of the underlying soil surface. Thus, the resultant backscattering is a mixture of interactions with not only the canopy

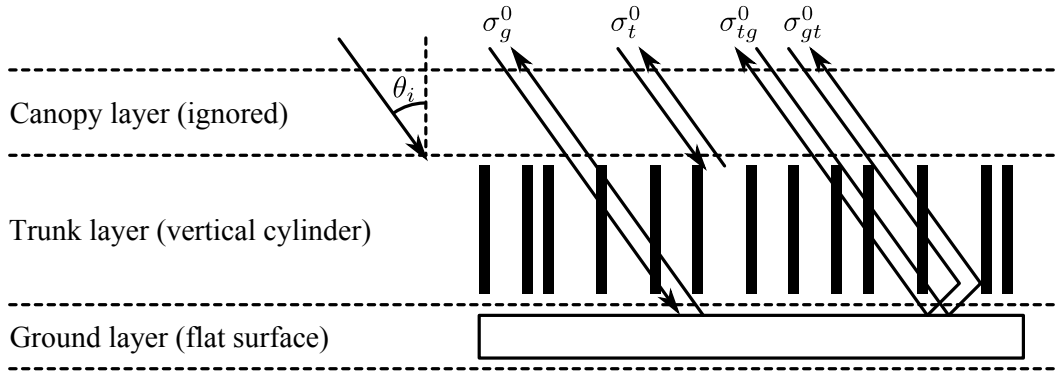

Figure 4.10: Simplified DSM geometry.

structure, but also soil surfaces and trunks. However, the coherent double-bounce scattering in ground-trunk interaction can be significant in the radar backscatter from the boreal forest which occupies about 60% of the land area of Canada, as reported in [32]. Therefore, model simplification should be made so as to leave this particular scattering component in the model, and additionally to be easily validated by well-controlled indoor laboratory experiments.

The canopy layer is removed to suppress the volume scattering component, and thus volume scattering occurs only from a cloud of dielectric cylinders for the trunk model, and from a rough ground surface at this step. To emphasize the ground-trunk interaction, the roughness parameters, the rms height, and the correlation length are selected so that the soil surface is considered to be flat, and the pdf of trunk inclination is a delta function which means all the trunks are vertically stood on the smooth soil surface. The pair of orthogonal surfaces of the ground and the trunks are obviously the source of double-bounce backscattering.

According to the above simplification, the scattering mechanisms considered in the model are illustrated in Figure 4.10 and are represented as follows:

1. *the direct backscattering from the trunks (σ_t^0),*
2. *the direct backscattering from the ground (σ_g^0),*
3. *scattering by the trunk followed by scattering by the ground (σ_{gt}^0),*
4. *the same scattering path taken place in the opposite direction (σ_{tg}^0).*

Computation of these scattering components includes the attenuation due to the trunk layer, through which an electromagnetic wave passes twice as an incoming wave from the transmitter, and as an outgoing wave left from the layer that returns back to the receiver. The total

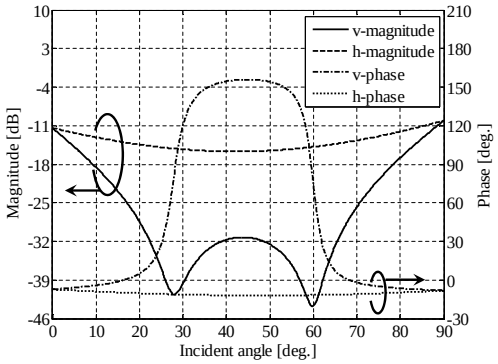

Figure 4.11: Brewster angle shown in the double-bounce scattering.

backscattering coefficient is given by the incoherent sum of each scattering contribution:

$$\sigma^0 = \sigma_t^0 + \sigma_g^0 + \sigma_{gt}^0 + \sigma_{tg}^0. \tag{4.21}$$

Though this simplified model seems to be slightly different from actual forests, the model can be viewed as an idealized boreal forest model to isolate the double-bounce scattering component. We can expect that the model prediction can be successfully applied to understand the scattering of real boreal forest since the scattering is usually dominated by the double-bounce scattering for L-band or P-band observation [32].

In addition, this model can be easily validated under well-controlled laboratory environments. Now that the main scattering contributor is the ground-trunk interaction, the effect of the moisture content on the double-bounce scattering can be revealed at this step. The backscattering coefficient is calculated for each linear polarization combination. In the following discussion, $qp \in \{hh, hv, vh, vv\}$ accounts for p-polarized transmission and q-polarized receiving, where h and v indicate horizontal and vertical polarization, respectively.

Figure 4.4 shows the geometry of the ground-trunk interaction which is expected to be the dominant scattering component in this simplified model. As discussed in Section 4.2, if we treat the two orthogonal surfaces as flat surfaces which have infinite extent, the total reflection from the orthogonal structure r_t can be expressed as the double-bounce Fresnel reflection coefficient in Equation (4.7).

Figure 4.11 shows the total reflection coefficient at horizontal and vertical polarization for $\varepsilon_g = 2.9 + 0.4j$ and $\varepsilon_t = 3.5 + 0.7j$. These permittivities are derived from semi-empirical permittivity models given in Equations (4.9) and (4.14), and correspond to the trunk volumetric

Table 4.1: DSM calculation parameters of (a) a typical boreal forest and (b) parameters for experimental validation.

Model	(a) L	(b) X
Wavelength [cm]	24	3
Trunk radius [cm]	8	1
Trunk length [m]	2.4	0.3
Trunk layer height [m]	2.4	0.3
Trunk density [#/m^2]	0.39	55.6
Trunk volumetric water content [%]	4.5 (Dry) – 46 (Wet)	
Trunk orientation	Vertical	
Volumetric soil moisture [%]	1.5 (Dry) – 58 (Wet)	
Amount of sand in soil [%]	50	
Amount of clay in soil [%]	15	
Surface roughness [cm]	10^{-6}	
Correlation length [cm]	0.1	

moisture content of 4.5% and the volumetric soil moisture of 1.5%.

The moisture contents are selected to simulate a typical dry forest. The curves of the vertical polarization drops off at certain incident angles due to Brewster angle at which a vertically-polarized wave perfectly transmits though a surface, and no reflection occurs at this angle. Since the model has a pair of the orthogonal surfaces, two Brewster angles, the smaller one for the trunk and the larger one for the ground surface, are given in Equations (4.6) and (4.8), respectively.

In addition, the vertically-polarized phase flips at the dips, and thus the phase indicates if an incident angle is within or without the interval between the two dips at the Brewster angles. We discuss the possibility of these characteristics as a indicator of moisture conditions later.

4.4.2 DSM Simulation Parameters

In forest monitoring applications, L-band or P-band wavelength is preferred, so ideally simulation and experimental validation should be conducted at a similar wavelength with actual forest geometry. Even so, laboratory measurements are more conveniently done on smaller scale models because a microwave anechoic chamber is spatially limited, and it is usually impossible to hold a large, real-scale forest model. The scaling of a nondispersive, lossless object, or a perfectly conducting object is readily accomplished by scaling the entire dimensions in inverse proportion to a scaled wavelength. However, for a lossy object such as soil or a tree, permittivity scaling is additionally required to maintain the entire electrical properties of an original model. Because the operation is difficult in practice, we employ the geometric scaling only in this study.

To examine the validity of our geometric scaling approach, DSM computation is conducted at two wavelengths of L-band and X-band for an actual forest model, and for a scaled forest model geometry, respectively. Table 4.1 lists the two set of simulation parameters. Model-L is a typical forest geometry for L-band observation, and Model-X is the scaled version of the Model-L geometry for the X-band experimental validation. Although the simulation model accepts ground and trunk moisture contents as independent parameters, it has been reported that we can assume a correlation between them as discussed in [35]. Therefore, we simply assume a linear relationship, and each volumetric moisture content is given by the following parametric form in terms of a variable "wetness" $w \in [0, 1]$:

$$m_\alpha = \left(w_\alpha^{\text{wet}} - w_\alpha^{\text{dry}}\right) w + w_\alpha^{\text{dry}}, \tag{4.22}$$

where $\alpha \in \{g, t\}$ accounts for ground or trunk, $w_\alpha^{\text{wet}}, w_\alpha^{\text{dry}}$ is the volumetric moisture contents at the wettest and the driest conditions. According to Table 4.1, these parameters are set to $w_g^{\text{wet}} = 0.58$, $w_g^{\text{dry}} = 0.015$, $w_t^{\text{wet}} = 0.46$, and $w_t^{\text{dry}} = 0.045$.

To adopt a flat soil surface model, the surface roughness is selected to a numerically small value compared to the wavelength, and a typical correlation length of a soil surface is selected here. The effect of the correlation length is not significant in this case because the surface roughness is negligibly small.

4.4.3 Numerical Result and Discussion

Figure 4.12 shows simulated backscattering coefficient for Model-L, and Figure 4.13 is for Model-X as well. Two types of wetness are shown in these figures to examine the effects of the moisture variation. Although the scaling of the permittivities cannot be taken into account, the following characteristics can be recognized in both models. The curves of the vv backscatter have the dips at certain incident angles due to the Brewster angle effects, and the co-polarized phase difference, that is, the phase difference between hh and vv polarization channels, flips at the dips, whereas hh relatively slowly fluctuates except for a large angle at the vicinity of 80° where both polarization curves touch a bottom simultaneously. Note that as all the phase values are constrained to the range from −180° to 180°, the phase values beyond this range are put on the opposite side of the figure. The dip at 80° appears because the incident wave propagates a longer distance within the trunk layer at a grazing angle and experiences greater attenuation. After exceeding 80° incidence, an incident wave strikes the cylinder surface almost perpendicularly, and

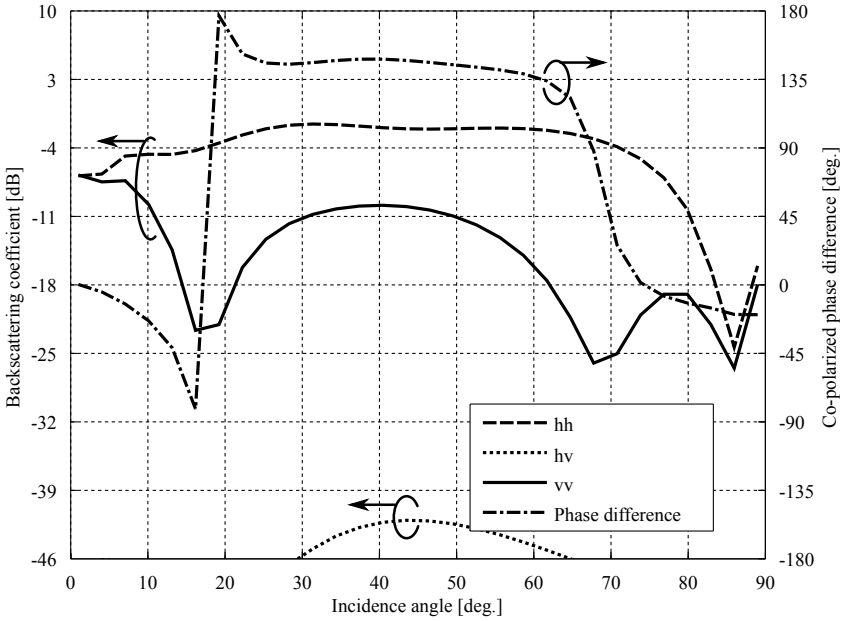

(a) Wetness $w = 0.25$.

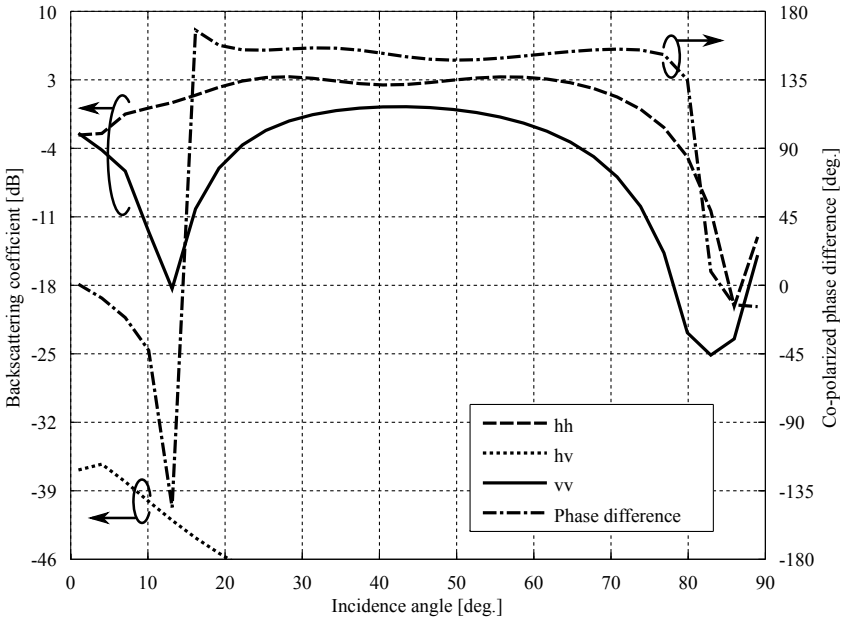

(b) Wetness $w = 1.0$.

Figure 4.12: DSM simulation result (Model-L).

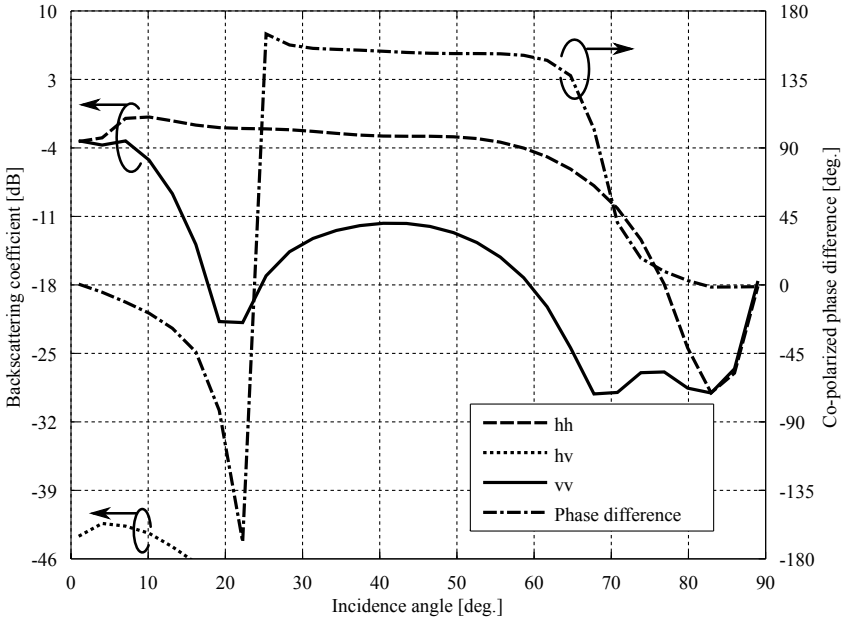

(a) Wetness $w = 0.25$.

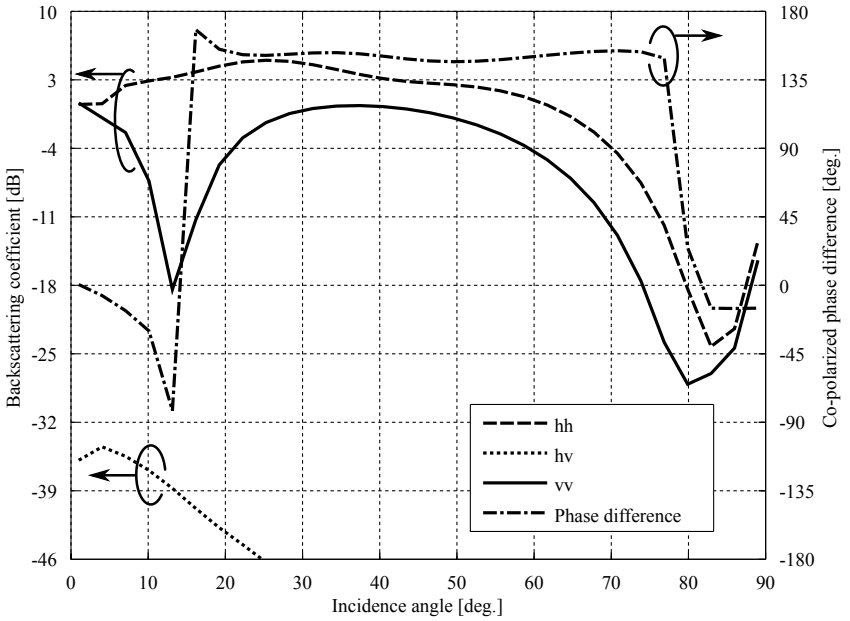

(b) Wetness $w = 1.0$.

Figure 4.13: DSM simulation result (Model-X).

the direct backscattering from the trunks increases the total backscattering coefficient. Brewster angle is a function of surface permittivity, and the dips move away from 45° with an increase in the permittivity, which corresponds to an increase in the moisture content. Therefore, we can emulate L-band observation using the X-band model without appropriate permittivity scaling. One can invert real-valued permittivity from the direct measurement of the dips, however, such measurement is unavailable in practice because the requirement of multiple angle observation. In addition, Brewster angle is correlated by other parameters such as surface roughness [36] and the randomness in the trunk angular distribution [37], and Brewster angle no longer has an one-to-one correspondence to permittivity in such a situation.

From a comparison of the backscattering coefficient at the drier and the wetter conditions, the difference between each polarization channel, that is referred to as co-polarization ratio, becomes small when an incident angle is around 45° as the wetness increases. Since the dips at the Brewster angles move away from 45° for a higher wetness, the co-polarization ratio at the angles except for 45° can be influenced by the dips, but the ratio still has a relationship to the variation of the moisture content. These facts imply that the co-polarization ratio can be an index to estimate the moisture content of the forested terrain without requiring multiple angle observation. Figure 4.14 and 4.15 show the co-polarization ratio and the co-polarized phase difference at 20°, 45°, and 70° incidence in terms of wetness. Note that 70° incidence is selected as the largest incident angle for spaceborne SAR systems, as it has been reported that JAXA ALOS-2 has the maximum incident angle of 70° [38], for example.

At 45° incidence, the ratio almost monotonically decreases with an increase in the wetness. Thus, the ratio can be an indicator of the relative variation in the moisture content. Apart from the 45° incidence, the ratio at 70° incidence is influenced by the dip at a Brewster angle which cross over the incident angle at a certain wetness. When the phase difference is near 0°, the ratio becomes larger with an increase in the wetness. Conversely, the ratio becomes smaller when the phase difference is near 180°. In Figures 4.14 and 4.15 at 70° incidence, we can interpret the variation of the co-polarization ratio as follows. When the co-polarized phase difference is near 0°, which means that the dip at the Brewster angle sits on the angle less than 70°, the ratio becomes larger because the dip approaches 70° with an increase in wetness. Conversely, the ratio becomes smaller when the phase difference is near 180°, because the dip moves away from 70°. In the region of extremely small wetness around 0 through 0.1 where an incident wave well penetrates the layer of the trunks, these tendency cannot be observed because of the weak double-bounce scattering contribution.

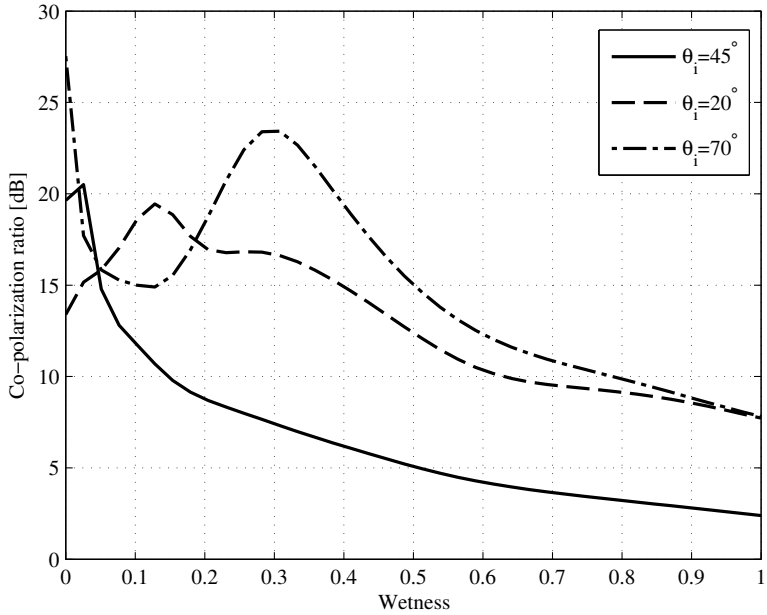

(a) Co-polarization ratio.

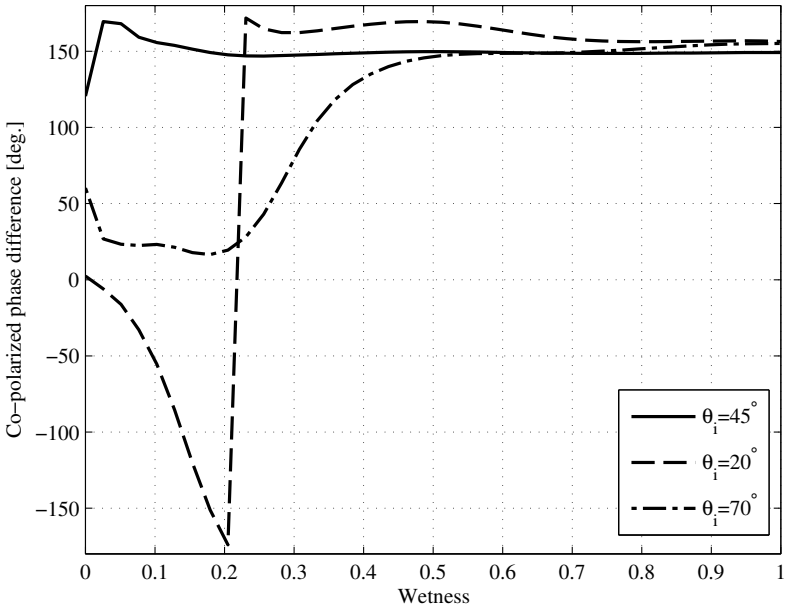

(b) Phase difference.

Figure 4.14: DSM simulation result (Model-L).

The fact that the co-polarized phase difference at the 45° incidence is near 180° indicates that the incidence angle is always between the dips at the two Brewster angles, as it is previously

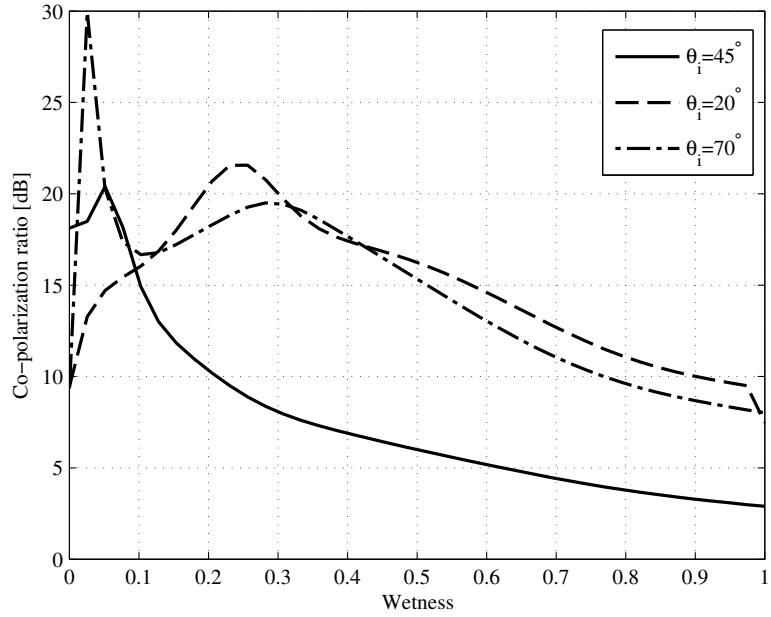

(a) Co-polarization ratio.

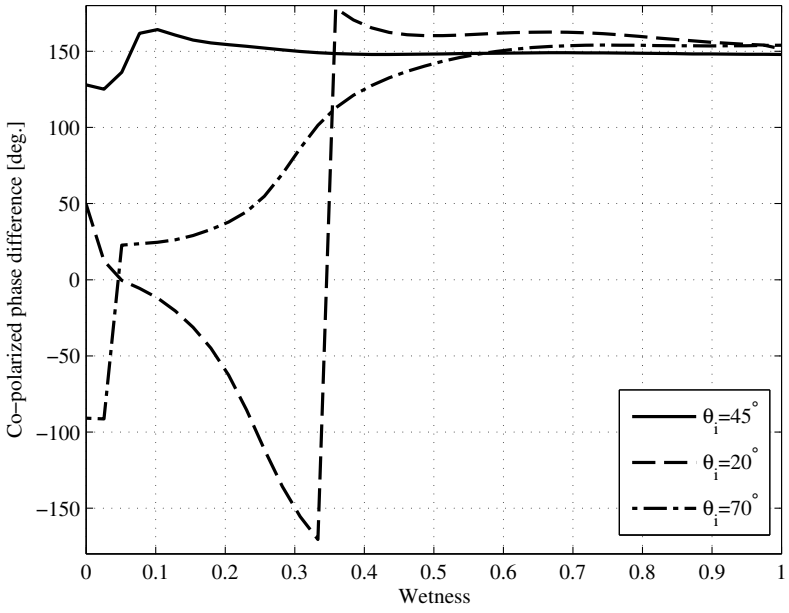

(b) Phase difference.

Figure 4.15: DSM simulation result (Model-X).

mentioned in the model description. In conclusion, both the co-polarization ratio and the phase difference are important parameters to characterize the relative variation of the forest moisture

content. The ratio at 45° incidence is moderate for monitoring the moisture because the magnitude of the ratio is directly related to the variation in the moisture content. More general situations in which the trunks have a certain randomness in their inclination is discussed in [37], and the similar conclusion can be derived for a small randomness.

4.5 Experimental Validation

A laboratory experiment in an anechoic chamber under well-controlled conditions is carried out to validate the DSM simulation results. As discussed in the previous section, we employ a scaled forest model due to the spatial limitation of the chamber. The details of this experiment is summarized in Chapter 2.

4.5.1 Experimental Results

Figure 4.16 shows the measured average RCS calculated from each SAR image for Wet-4 and Wet-8 conditions. Similar to the simulation results, the *hh*- and *vv*-polarized RCS around 45° incidence approach each other with an increase in the moisture content. In the Wet-8 condition, the two dips at the Brewster angles, as well as phase flipping at the dips are clearly recognized, whereas the dip at a smaller incidence angle cannot be recognized in the Wet-4 condition. Because an incident wave tends to well penetrate the layer of the wooden structure as the test pieces get drier, the reflection from the supporting structure of the ground plate may strongly contribute to the resultant backscattering, overlaying the weak reflection from the trunks. Although the dip at the Brewster angle collapses, the co-polarization ratio can still indicate the relative variation of the moisture content.

Figure 4.17 shows the measured co-polarization ratio and the co-polarized phase differences in terms of Wet-number. At 45° incidence, the ratio simply decreases with an increase in Wet-number. As mentioned in the previous simulation, this is because the dip at a Brewster angle does not cross over the incident angle, and 45° incidence is moderate for estimating moisture conditions. The ratio measured at 70° incidence has a spike at the Wet-2 condition in which the dip at a Brewster angle crosses over the incident angle, and also this can be clearly recognized in the phase difference variation. The phase difference at 70° drastically goes away from 180° and approaches 0° incidence when the Wet-number becomes small, while the phase difference at 45° incidence stays above 90°. The tendency of these experimental results agrees well with DSM simulation, and therefore, it is shown that both the ratio and the phase difference are important

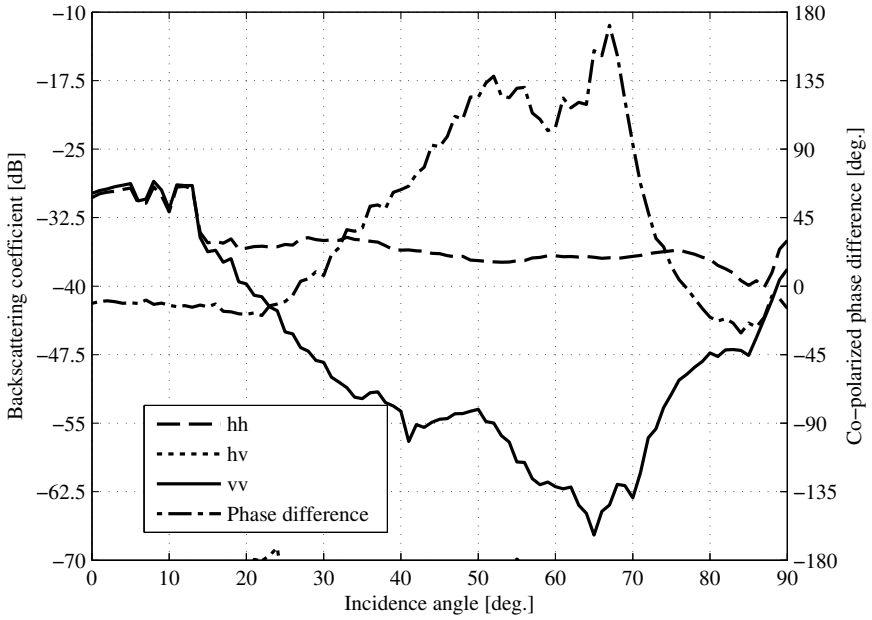

(a) Wet-4.

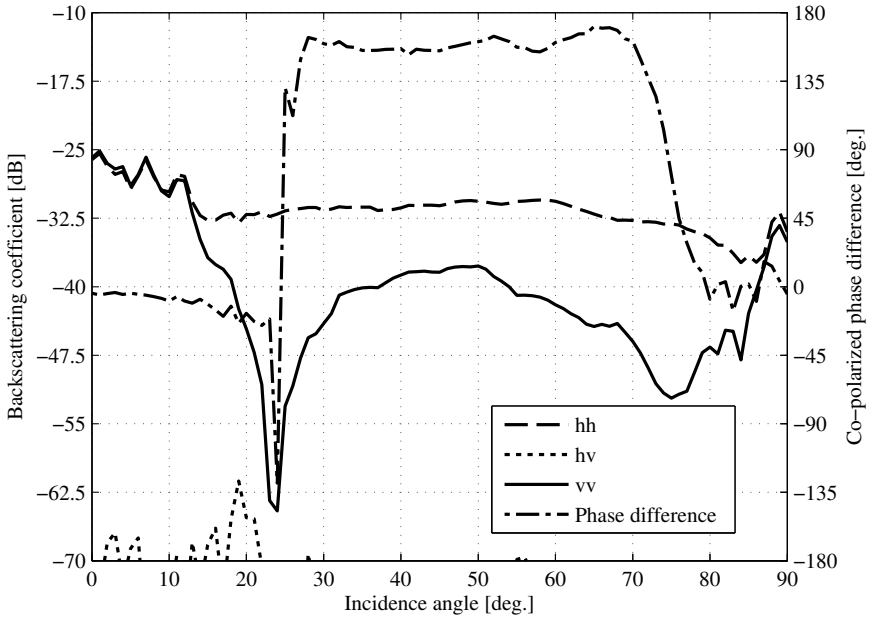

(b) Wet-8.

Figure 4.16: Measured average radar cross section and co-polarized phase difference.

parameters to monitor the relative variation of the forest moisture conditions.

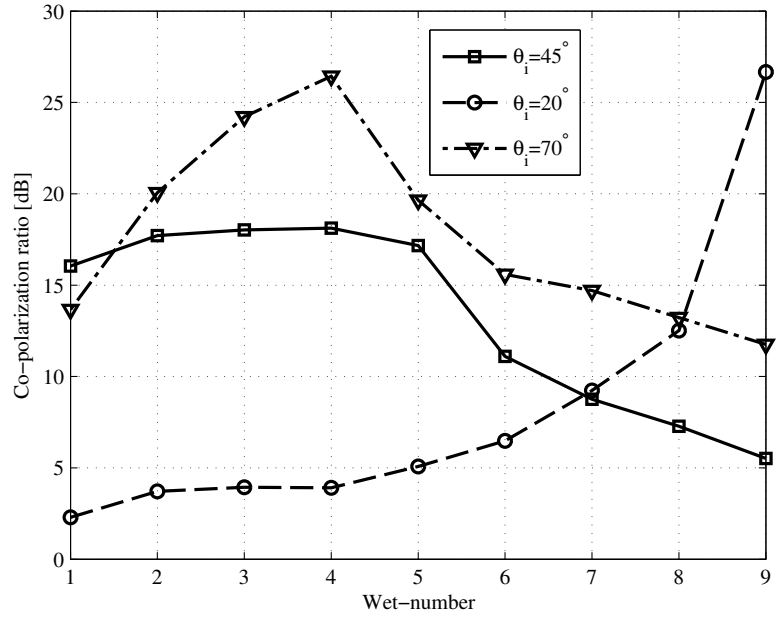

(a) Co-polarization ratio.

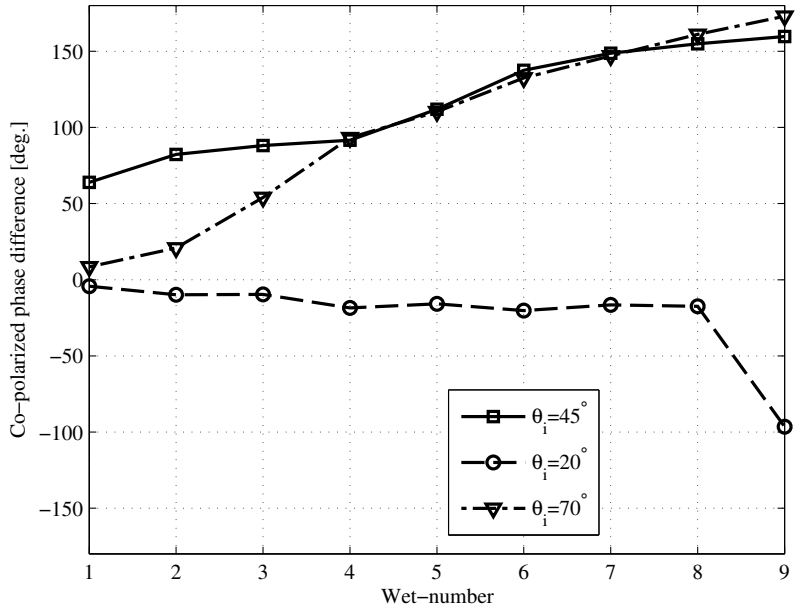

(b) Phase difference.

Figure 4.17: Measured co-polarization ratio and co-polarized phase difference.

4.6 Summary of This Chapter

This chapter have presented the multiple angle SAR image analysis. As an example of the multiple angle measurement, the estimation of the moisture condition of forested terrain is dis-

cussed, and we have shown that the co-polarization ratio can be used to infer the forest moisture condition.

Chapter 5

Tomographic SAR

Introduction

If only a single path image is given, all we are able to reconstruct is an image of virtual scatterers. To decompose these virtual scatterers into the distribution of actual scatterers, one has to perform additional processing such as SAR interferometry or SAR tomographic reconstruction. SAR interferometry is widely recognized as a tool to extract topographic information of a terrain surface, however, only two scattering points can be resolved due to the limitation that the system has only two distinct flight paths. TomoSAR, the rapidly developing technology which exploits multiple flight path information, can resolve the difficulties of SAR interferometry. TomoSAR uses array signal processing to extract the actual scatterer location, i.e. height information, from the images of virtual scatterers observed from slightly different radar altitude. Thus, TomoSAR can be considered as an extension of SAR interferometry. Because the variety of array signal processing algorithms, TomoSAR reconstruction can be expected as a high resolution and high-precision topographic mapper.

The introduction of the high-resolution spectrum estimators which have developed for direction finding problem of array antenna opened a new branch in SAR three-dimensional reconstruction problem.

Outline

This chapter provides the groundwork for polarimetric TomoSAR reconstruction problem. First, Section 5.2 redefines the slant plane SAR image reconstruction described in Chapter 2 so that

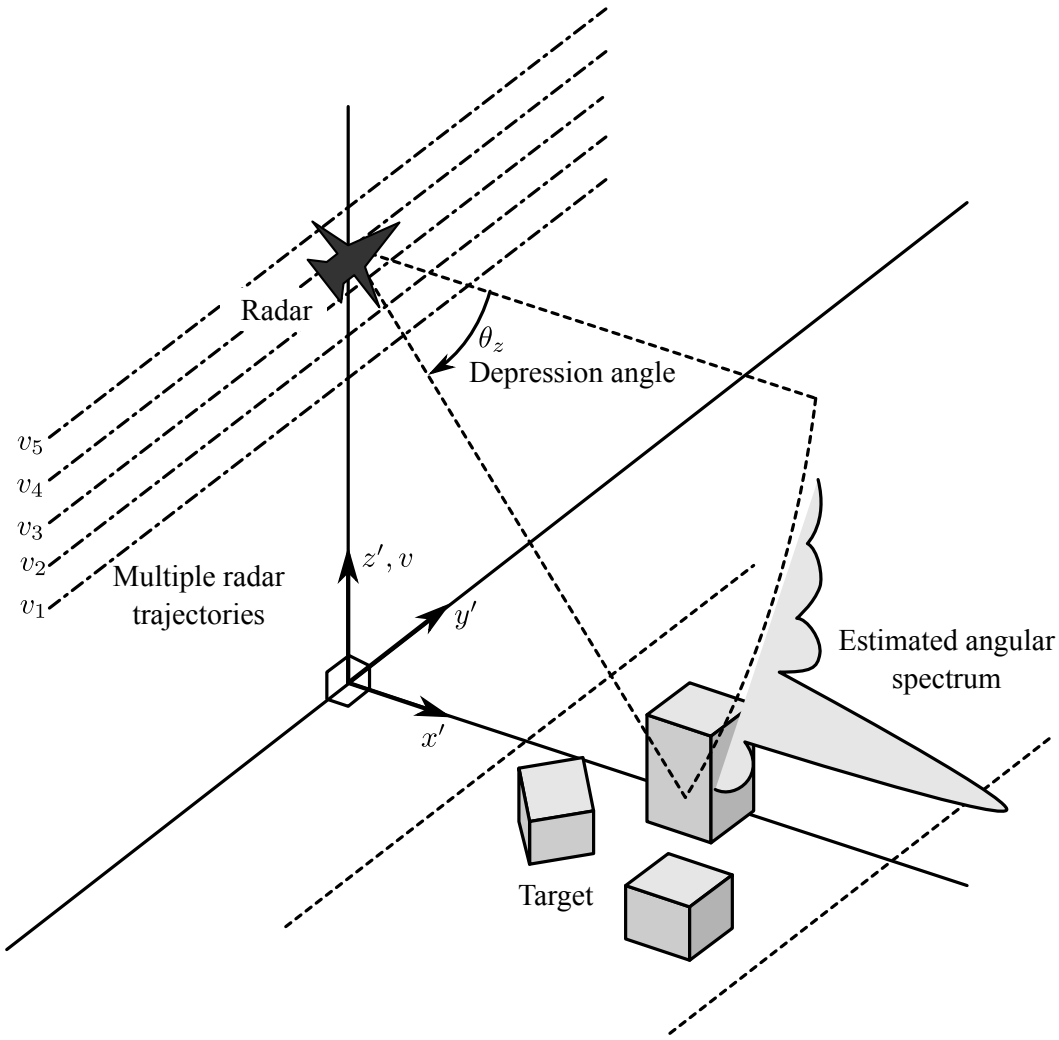

Figure 5.1: SAR observation scenario.

the system model is appropriate for tomographic reconstruction problem. In Section , we first present the observation scenario of TomoSAR system.

5.1 Observation Scenario

The well-known height information recovering is the interferometric SAR (InSAR) [39] of which the radar has two receiving antenna at different locations, or two repeat-path measurement data could be used for InSAR analysis. However, image reconstructed from InSAR image is *pseudo* three-dimensional image in the sense that only a single height can be estimated for each image

pixel.

The TomoSAR is an extension of the conventional InSAR measurement, utilizing the multiple path observation. TomoSAR observation scenario is depicted in Figure 5.1. The radar carrying aircraft flies over the observing terrain repeatedly. Then, the standard slant-plane SAR image is formed by the algorithm given in Chapter 2. As discussed in the beginning of Chapter 2, the height information cannot be recovered from a single slant-plane SAR image because all the three-dimensional target locations are projected onto a two-dimensional image plane.

Once multiple images are reconstructed, several spectrum estimation algorithms developed for array antenna, that is, DOA estimation methods, is applied on each image pixel to estimate the angular or height spectrum.

5.2 System Model

This section redevelops SAR signal model presented in Chapter 2. The reconstruction is quite similar to those developed for conventional single-path SAR.

5.2.1 Signal Model

The radial distance to the radar to the nth target is

$$r'_n = \sqrt{x'^2_n + (y_n - u)^2 + (z_n - v)^2}. \tag{5.1}$$

The echoed signal is then represented by

$$s(t, u, v) = \sum_n \sigma_n p\left(t - \frac{2r'_n}{c}\right). \tag{5.2}$$

The Fourier transform of the SAR signal with respect to the fast-time variable t is

$$s(\omega, u, v) = P(\omega) \sum_n \sigma_n \exp\left(-j2kr'_n\right). \tag{5.3}$$

Using the above signal model, we can formulate a three-dimensional reconstruction algorithm via matched filtering like two-dimensional reconstruction described in Chapter 2, provided that the linear synthetic aperture in the elevation domain v is available. However, it is difficult to form an elevation synthetic aperture in the airborne or spaceborne observation, requiring precise

control of the platform attitude and paths. Thus, we do not utilize matched filtering operation in the elevation domain, and we recover three-dimensional scatterer location via multiple two-dimensional slant plane SAR images.

The two-dimensional slant plane SAR reconstruction procedure is described in Chapter 2. In the slant plane reconstruction, the scatterer altitude is *transparent* to the user because all the scatterers which have the same slant range are projected on the (x, y) plane in Figure X. The slant range of the nth target can be calculated by

$$x_n = \sqrt{x_n'^2 + (Z_c - z_n)^2}. \tag{5.4}$$

Then, the radial distance to the radar to the nth target is

$$r_n = \sqrt{x_n^2 + (y_n - u)^2}, \tag{5.5}$$

and the signal model becomes

$$s(t, u) = \sum_n \sigma_n p\left(t - \frac{2r_n}{c}\right). \tag{5.6}$$

Or, its fast-time frequency domain representation is

$$s(\omega, u) = P(\omega) \sum_n \sigma_n \exp\left(-j2kr_n\right). \tag{5.7}$$

The above two-dimensional signal model is exactly same as the model described in Chapter 2, and similar reconstruction procedure can be utilized.

5.3 Basics of DOA Estimation

Before moving on to the discussion on tomographic reconstruction problems, this section a brief introduction to the direction-of-arrival (DOA) estimation methods which have been used in array antenna signal processing.

5.3.1 System Model

Figure 5.2 (a) and (b) show the system models of array DOA estimation problem for active and passive case, respectively. In the former case, our problem is to identify the location of the

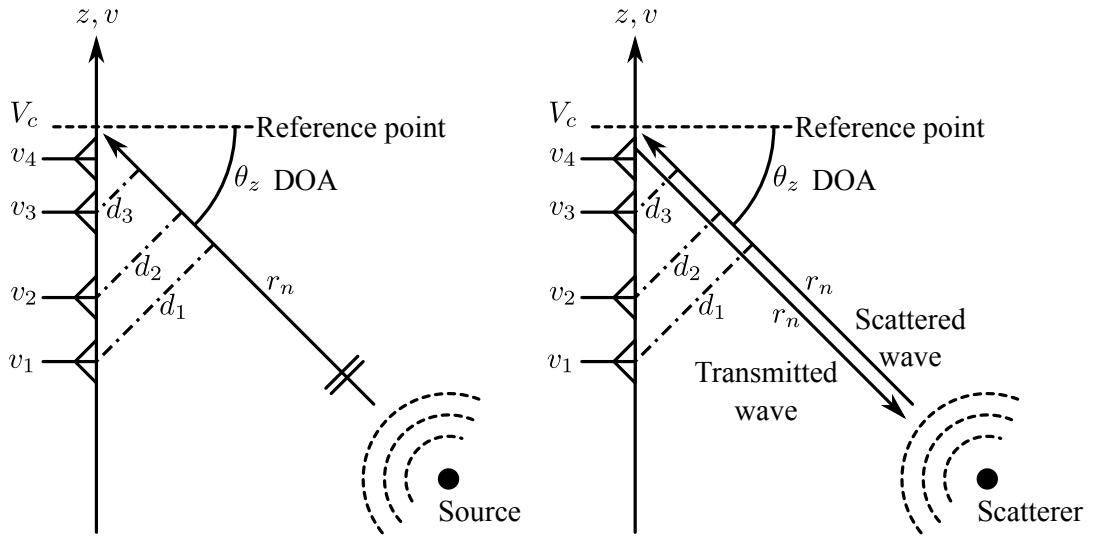

(a) Passive array imaging.

(b) Active array imaging.

Figure 5.2: DOA estimation using an array antenna for (a) passive and (b) active case.

source in terms of *depression angle* or *angle of arrival* (AOA) θ_z. Thus, all the antenna elements works as receivers. The latter case has the similar geometry of the passive case, however, the antenna elements transmit an electromagnetic wave and then receives the reflected wave from the scatterer.

5.3.2 Signal Model

We denote the location of nth array element by v_n, and arbitrary chosen reference point on the v-axis by V_c. The radial distance from the reference point to the nth source or scatterer is represented by r_n, and AOA for this source or scatterer is denoted by θ_z^n. Although general three-dimensional formulation is possible, however, the two-dimensional treatment is sufficient for our TomoSAR reconstruction problem as discussed later.

Let $s(t)$ be the complex amplitude of the received signal at time t, and n_i be the additive noise imposed on the ith array element. The received signal for an array antenna can be modeled via

$$\boldsymbol{x}(t) = \boldsymbol{a}(\theta_z)s + \boldsymbol{n}(t), \tag{5.8}$$

where $\boldsymbol{a}(\theta_z)$ is called the *array steering vector* which represents the phase difference between a reference point and each array element. For linear array configuration, the array steering vector

becomes

$$\boldsymbol{a}(\theta_z) = \Big[\exp(-jk_z v_1) \quad \exp(-jk_z v_2) \quad \cdots \quad \exp(-jk_z v_K),\Big]^T \tag{5.9}$$

where k_z is spatial frequency for the z domain defined via

$$k_z = \begin{cases} \dfrac{2\pi}{\lambda}\sin\theta_z & \text{for passive problem,} \\ \dfrac{4\pi}{\lambda}\sin\theta_z & \text{for active problem,} \end{cases} \tag{5.10}$$

where λ is wavelength. The difference of the above spatial frequency definition dictates the spatial sampling constraints in the z-direction. Theory of classical array signal processing states that, for source estimation (passive sensing) using a uniform linear array (ULA), the element spacing Δ_v must satisfy

$$\Delta_v \leq \frac{\lambda}{2} \tag{5.11}$$

to arias-free (i.e. without grating robe) spectrum estimation. However, as shown in Equation (5.10), active sensing problem has equivalently twice as higher frequency as that of the passive sensing problem. Therefore, for an active sensing problem such as TomoSAR requires the following spatial sampling criteria to achieve alias-free reconstruction.

$$\Delta_v \leq \frac{\lambda}{4}. \tag{5.12}$$

Note that this is the worst case that the antenna has an omni-directional beam pattern and the target area extends infinitely in the altitude direction.

Obviously, Equation (5.12) is difficult to satisfy in the case of airborne or spaceborne SAR observation because the requirement of sub-wavelength control of the platform flight paths. However, in TomoSAR reconstruction problem, we have *a priori* knowledge or estimate about the scatterer location. Thus, we can tolerate the existence of aliasing or grating-robe at a target-free region, and the arias-free condition of Equation (5.12) is unnecessary to satisfy.

Assuming that the array reference point is located at the first array element at v_1 (i.e. master path), the array steering vector can be further simplified as

$$\boldsymbol{a}(\theta_z) = \Big[1 \quad \exp(-jk_z\Delta_v) \quad \exp(-jk_z 2\Delta_v) \quad \cdots \quad \exp[-jk_z(K-1)\Delta_v]\Big]^T. \tag{5.13}$$

5.3.3 Correlation Matrix

The data correlation matrix is defined via

$$\boldsymbol{R}_{xx} = \left\langle \boldsymbol{x}(t)\boldsymbol{x}(t)^{\dagger} \right\rangle, \tag{5.14}$$

where $[\cdot]^{\dagger}$ represents conjugate (Hermitian) transpose operation, and $\langle\cdot\rangle$ denotes ensemble average. Provided that the additive noise is incoherent to the arriving wave, the data correlation matrix can be represented as

$$\begin{aligned} \boldsymbol{R}_{xx} &= \boldsymbol{R}_S + \boldsymbol{R}_N \\ &= \boldsymbol{A}\boldsymbol{S}\boldsymbol{A}^{\dagger} + \boldsymbol{R}_N, \end{aligned} \tag{5.15}$$

where $\boldsymbol{R}_s$, $\boldsymbol{R}_N$, and $\boldsymbol{S}$ are the signal, noise, and source correlation matrix, respectively, and they are defined as

$$\boldsymbol{R}_S = \boldsymbol{A}\boldsymbol{S}\boldsymbol{A}^{\dagger}, \tag{5.16a}$$

$$\boldsymbol{R}_N = \langle \boldsymbol{n}(t)\boldsymbol{n}(t)^{\dagger} \rangle, \tag{5.16b}$$

$$\boldsymbol{S} = \langle \boldsymbol{s}(t)\boldsymbol{s}^{\dagger} \rangle. \tag{5.16c}$$

In addition, these are Hermitian matrices which satisfy

$$\boldsymbol{R}_{xx} = \boldsymbol{R}_{xx}^{\dagger}. \tag{5.17}$$

Assuming that the additive noise is white Gaussian noise, the noise correlation matrix can be expressed as

$$\begin{aligned} \boldsymbol{R}_N &= \langle \boldsymbol{n}(t)\boldsymbol{n}^{\dagger}(t) \rangle \\ &= \sigma^2 \boldsymbol{I}, \end{aligned} \tag{5.18}$$

where I is an unit matrix. One may recall that the noise components of the polarimetric covariance matrix of Equation (3.8) in Chapter 3 only remain in the diagonal term.

Practically, the following estimates of the data correlation matrix is used for DOA estimation

problem.

$$\hat{\boldsymbol{R}}_{xx} = \frac{1}{N_s}\sum_{i}^{N_s} \boldsymbol{x}(t_i)\boldsymbol{x}(t_i)^{\dagger} \tag{5.19}$$

5.3.4 Classical Beamformer

The classical beamformer is the simplest DOA estimator which is defined as the problem of maximizing the array output power by scanning the array main beam in entire angular domain. The beamformer is equivalent to the Fourier transform, and the angular resolution is restricted to the array aperture length.

The maximization problem is defined by

$$\max_{\boldsymbol{w}} E\left[\boldsymbol{w}^{\dagger}\boldsymbol{x}(t)\boldsymbol{x}(t)^{\dagger}\boldsymbol{w}\right] \tag{5.20}$$

$$\max_{\boldsymbol{w}} \boldsymbol{w}^{\dagger}\boldsymbol{R}_{xx}\boldsymbol{w} = \max_{\boldsymbol{w}} \left(P_1 \left|\boldsymbol{w}^{\dagger}\boldsymbol{a}(\theta)\right|^2 + \sigma^2 \left|\boldsymbol{w}\right|^2\right) \tag{5.21}$$

In this condition, the optimum weight is

$$\boldsymbol{w}_B = \frac{\boldsymbol{a}(\theta)}{\sqrt{\boldsymbol{a}(\theta)^{\dagger}\boldsymbol{a}(\theta)}}. \tag{5.22}$$

Therefore, the beamformer spectrum estimator is defined via

$$P_B(\theta) = \frac{\boldsymbol{a}(\theta)^{\dagger}\boldsymbol{R}_{xx}\boldsymbol{a}(\theta)}{\boldsymbol{a}(\theta)^{\dagger}\boldsymbol{a}(\theta)}. \tag{5.23}$$

The example of the beamformer spectrum is described below.

$$P_B(\theta) = \frac{1}{K}\left(P_1 \left|\boldsymbol{a}(\theta)^{\dagger}\boldsymbol{a}(\theta_1)\right|^2 + K\sigma^2\right) \tag{5.24}$$

$$= LP_1 \left\{ \frac{\sin\left[\frac{\pi}{\lambda_c} L\Delta_v(\sin\theta - \sin\theta_1)\right]}{K\sin\left[\frac{\pi}{\lambda_c} L\Delta_v(\sin\theta - \sin\theta_1)\right]} \right\}^2 + \sigma^2 \tag{5.25}$$

The maximum (or maxima) of the sinc-like function in the above equation dictates the direction of arrival.

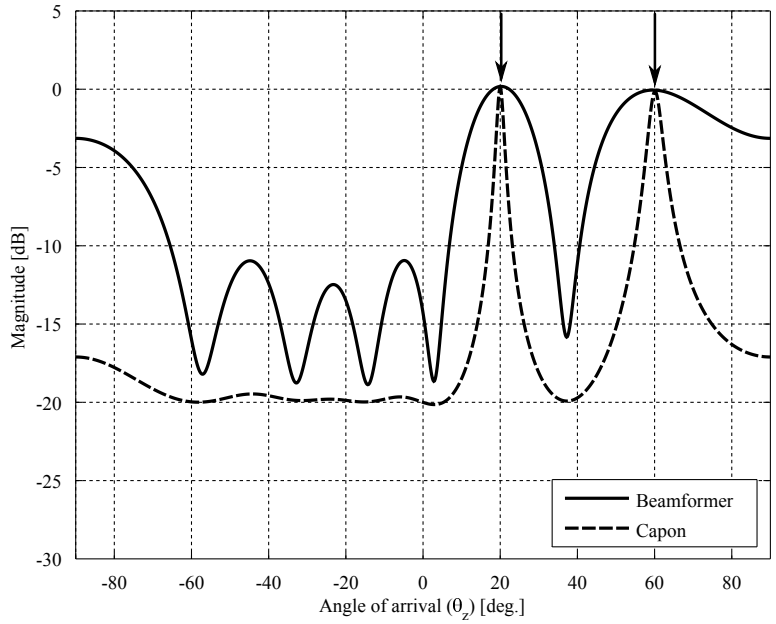

Figure 5.3: Beamformer and Capon spectrum for passive case ($K = 7$, $\Delta_z = \lambda/2$, $\theta_{z1} = 20°$, $\theta_{z2} = 60°$, SNR=30 dB).

5.3.5 Capon Estimator

The optimization problem of the Capon estimator is defined via

$$\min_{\boldsymbol{w}} \boldsymbol{w}^\dagger \boldsymbol{R}_{xx} \boldsymbol{w}, \quad \text{subject to} \quad \boldsymbol{w}^\dagger \boldsymbol{a}(\theta) = 1. \tag{5.26}$$

The optimum weight for the Capon estimator can be derived using the *method of Lagrange multiplier* (MLM) as follows:

$$\boldsymbol{w}_C = \frac{\boldsymbol{R}_{xx}^{-1} \boldsymbol{a}(\theta_z)}{\boldsymbol{a}(\theta)^\dagger \boldsymbol{R}_{xx}^{-1} \boldsymbol{a}(\theta)}. \tag{5.27}$$

Then, the Capon angular spectrum is defined by

$$P_C(\theta_z) = \frac{\boldsymbol{a}(\theta_z)^\dagger \boldsymbol{a}(\theta_z)}{\boldsymbol{a}(\theta)^\dagger \boldsymbol{R}_{xx}^{-1} \boldsymbol{a}(\theta)}. \tag{5.28}$$

5.3.6 Numerical Examples

The numerical examples of the beamformer and Capon spectrum estimators are shown here.

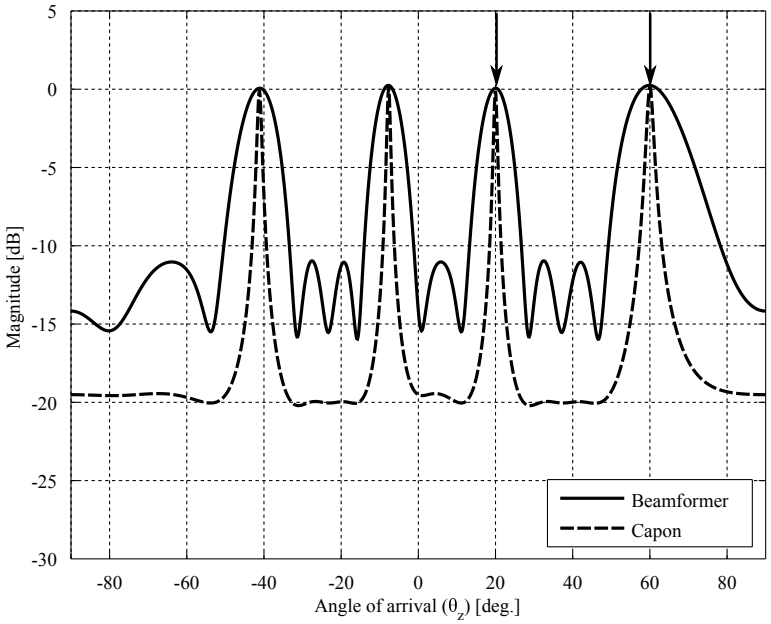

Figure 5.4: Beamformer and Capon spectrum for passive case ($K = 7$, $\Delta_z = \lambda/2$, $\theta_{z1} = 20°$, $\theta_{z2} = 60°$, SNR=30 dB).

5.4 TomoSAR Reconstruction

In this section, we extend DOA estimation concepts presented in Section 5.3. The concept of DOA estimator based TomoSAR reconstruction problem is depicted in 5.5. As mentioned in Chapter 2, three-dimensional scatterer location is projected onto the two-dimensional image plane. In Figure 5.5, the projected scatter location is identified by *virtual scatter* which is composition of the actual scatterers having three-dimensional location. Our task is to decompose the virtual scatterers into the individual actual scatterers. From Figure 5.5, we must identify the target range x_n and the depression angle of an actual scatterer $\theta_z^{m,n}$ to recover the three-dimensional location of the actual scatterer. We already have the target range x_n in the image plane by the synthetic aperture reconstruction presented in 2. And now, we can utilize DOA estimator to determine the depression angle $\theta_z^{m,n}$.

5.4.1 Array Steering Vector

Although one can employ the array steering vector of Equation (5.9), we present more accurate form of the *near-field* array steering vector. Consider that the situation depicted in Figure x.

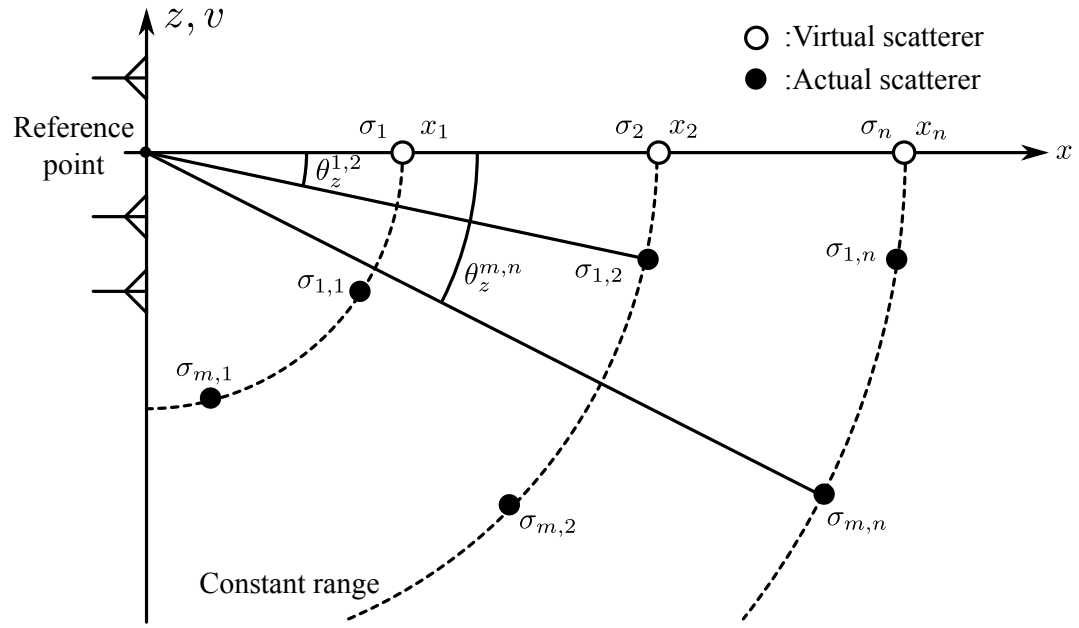

Figure 5.5: Virtual scatterers and actual scatterers

We denote the range of the nth scatterer by x_n, and the depression angle by θ_z which is to be scanned by the DOA estimators. Then, the distance from the radar at an altitude z_i to the actual scatterer can be represented by

$$r_s(z_i, \theta_z) = \sqrt{z_i^2 + x_n^2 + 2z_i x_n \sin\theta_z}. \tag{5.29}$$

Then, the array steering vector is denoted by

$$\boldsymbol{a}(\theta_z) = \Big[\exp\left[-jk_z r_s(z_1, \theta_z)\right] \quad \exp\left[-jk_z r_s(z_2, \theta_z)\right] \quad \dots \quad \exp\left[-jk_z r_s(z_K, \theta_z)\right]\Big]^T, \tag{5.30}$$

where we use the spatial frequency k_z for active sensing case. Also far-field array steering vector can be written by

$$\boldsymbol{a}(\theta_z) = \Big[\exp\left(-jk_z z_1\right) \quad \exp\left(-jk_z z_2\right) \quad \dots \quad \exp\left(-jk_z z_K\right)\Big]^T. \tag{5.31}$$

5.4.2 Reconstruction

Once the appropriate array steering vector is determined, we can apply DOA estimator to the slant-plane SAR images. We denote the discrete SAR image pixel by $f_{z_m}(x_i, y_j)$, where z_m is

radar location in the altitude domain z, and (x_i, y_j) represent discrete spatial variables in the image plane. The TomoSAR reconstruction algorithm is summarized below:

Step 1. *For each image pixel at (x_i, y_j), form a received signal vector $\boldsymbol{x}(x_i, y_j)$ by*

$$\boldsymbol{x}(x_i, y_j) = \begin{bmatrix} f_{z_1}(x_i, y_j) & f_{z_2}(x_i, y_j) & \dots & f_{z_K}(x_i, y_j) \end{bmatrix}^T. \tag{5.32}$$

Step 2. *Determine the depression angle θ_z to be reconstructed.*

Step 3. *Form array steering vector defined in Equation (5.30) for a near-field problem and Equation (5.31) for a far-field problem.*

Step 4. *Compute the angular spectrum at the specified depression angle θ_z as discussed in Section 5.3.*

Step 5. *Repeat **Step 2.** to **Step 4.** for all the image pixel at (x_i, y_j).*

Step 6. *The resultant samples are within polar coordinate (x_i, θ_z), so one might assign the polar sample to the rectangular sample in the (x, z) plane via*

$$(x, z) = (x_i \cos\theta_z, -x_i \sin\theta_z). \tag{5.33}$$

5.4.3 Experimental Validation

The experimental validation is done by using the linear SAR images presented in Chapter 2.

Figure 5.6 shows the tomographic reconstruction using the beamformer for building model. The image shows the three-dimensional rendering of the isosurface at -10 dB, and hh-polarized SAR images are used for this tomographic reconstruction. The scattering from the ground plate edge, stack of concrete cubes, concrete cylinder, and an array of concrete cubes are properly imaged.

Figure 5.8 shows the tomographic reconstruction using the Capon estimator. Because the radiometric accuracy of the Capon estimator is worse compared to the beamformer spectrum, the estimated three-dimensional spectrum is normalized by its maximum value for displaying purpose. Although the spatial resolution seems to be improved, one can hardly recognize the structure of the target from the three-dimensional rendering image of Capon spectrum.

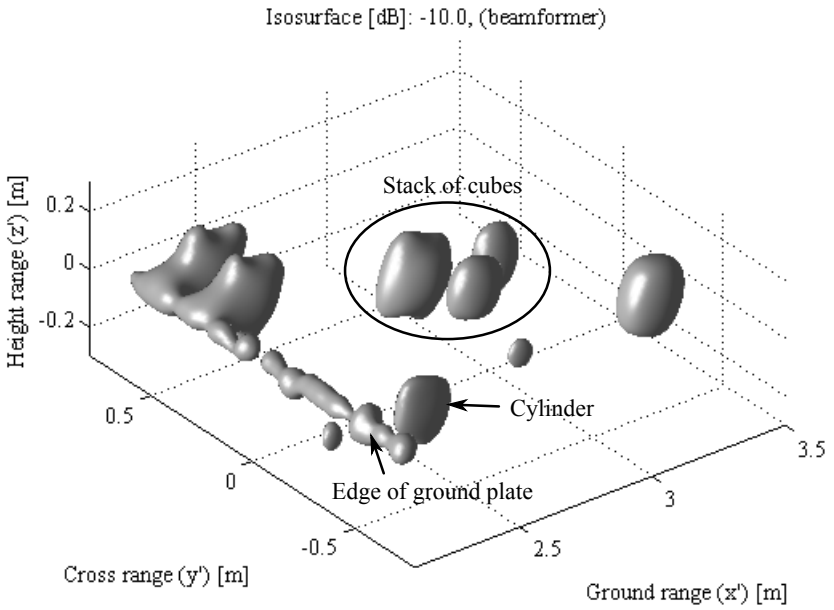

Figure 5.6: Three-dimensional rendering image (building model, beamformer, *hh*-polarization)

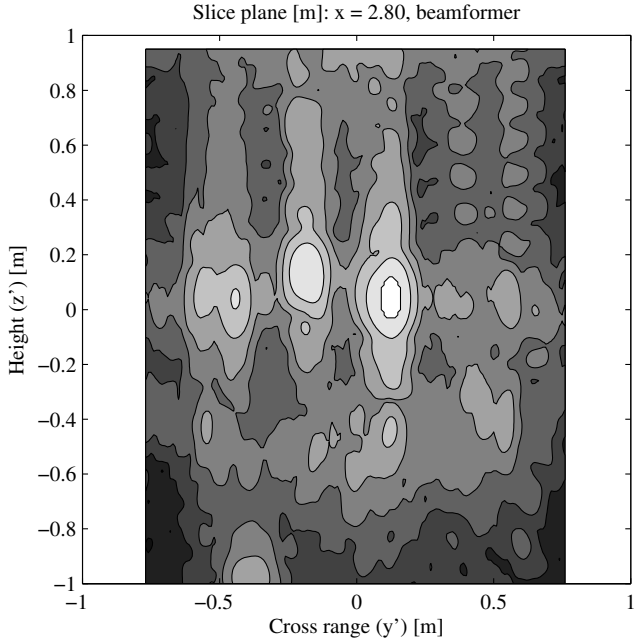

Figure 5.7: Slice image at $x' = 2.8$ m plane (building model, beamformer, *hh*-polarization).

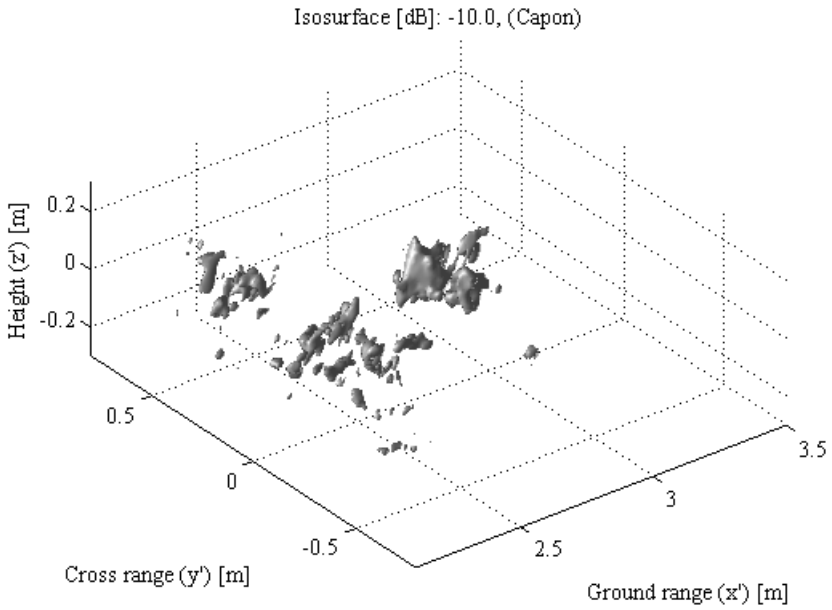

Figure 5.8: Three-dimensional rendering image (building model, Capon, hh-polarization)

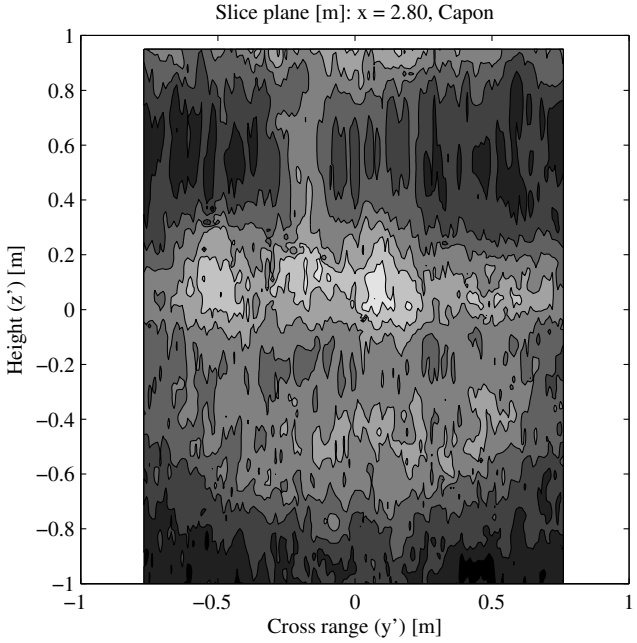

Figure 5.9: Slice image at $x' = 2.8$ m plane (building model, Capon, hh-polarization).

5.5 Polarimetric TomoSAR

Once a single-polarization TomoSAR reconstruction algorithms is developed, one can readily extend to the fully polarimetric case. To conclude this chapter, we examine the fully polarimetric TomoSAR reconstruction using classical Pauli decomposition which is described in Chapter 3.

5.5.1 Three-Dimensional Pauli Decomposition

We can readily introduce the Pauli decomposition described in 3 into the TomoSAR reconstruction. This can be simply achieved via the following steps:

Step 1 *Reconstruct slant-plane SAR image via the algorithm presented in Chapter 2 for each polarization and radar altitude.*

Step 2 *Compute the Pauli Decomposed image as described in Equation x in Chapter 3.*

Step 3 *Applying the DOA estimator based TomoSAR reconstruction algorithms given in Section 5.4*

5.5.2 DFT-Based Tomographic Reconstruction

The tomographic reconstruction using the conventional DOA estimators which are described in Section 5.4 is impossible to preserve the coherent information of the SAR image. Although Pauli decomposition can be simply extended to the tomographic case, this is not the case for other advanced polarimetric concepts such as the model-based decomposition described in Chapter 3. Therefore, the phase-preserving formulation of DOA estimation problem is necessary. This is readily done by employing the following alternate form of the beamformer spectrum:

$$P_D(\theta) = \frac{\boldsymbol{a}(\theta)^\dagger \boldsymbol{x}}{\sqrt{K}}. \tag{5.34}$$

The above equation is equivalent to the DFT, and the phase information is preserved. Then, we can construct the polarimetric covariance or coherency matrix at each three-dimensional pixel for the model-based decomposition algorithms in Chapter 3.

5.5.3 Experimental Validation

We now present the experimental validation of the polarimetric TomoSAR reconstruction. Figure 5.10, 5.11, and 5.12 show the three-dimensional version of model-based decomposition algorithms

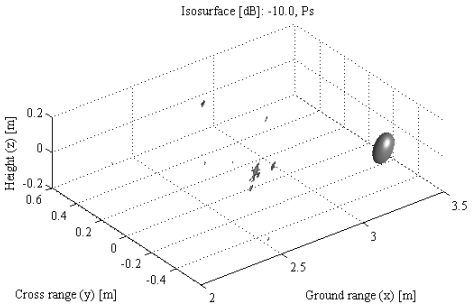

(a) Surface scattering.

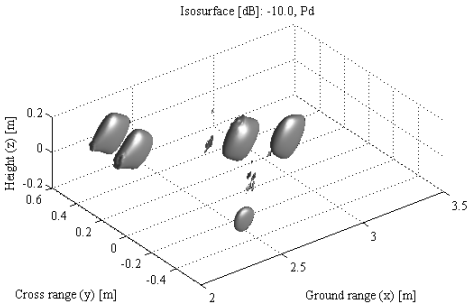

(b) Double-bounce.

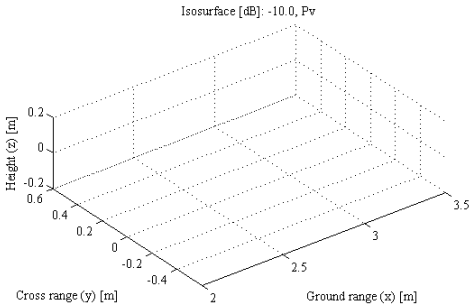

(c) Volume scattering.

Figure 5.10: Three-dimensional polarimetric decomposition (FDD).

for FDD, Yamaguchi decomposition, and AMBD, respectively. The angular spectrum estimator defined in Equation (5.34) is used for three-dimensional tomographic reconstruction. As it is expected from the result presented in Chapter 3, all the decomposition algorithms provide similar results. We can see that the double-bounce scattering occurred between the ground surface and building blocks is dominated. From these results, the combination of the model-based decomposition algorithms and tomographic SAR is able to provide the three-dimensional scattering mechanisms of the observing targets.

5.6 Summay of This Chapter

In this chapter, tomographic reconstruction algorithm using DOA spectrum estimators is provided. We have shown a simple extension of TomoSAR to the fully polarized case, and it has shown that the polarimetric analysis provides us an additional information to understand the

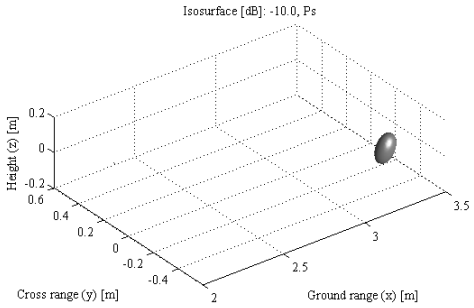

(a) Surface scattering.

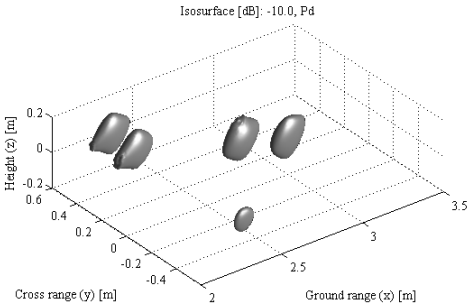

(b) Double-bounce.

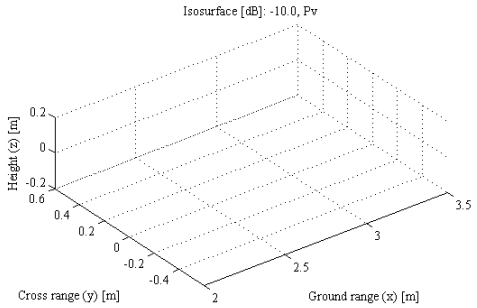

(c) Volume scattering.

Figure 5.11: Three-dimensional polarimetric decomposition (Yamaguchi).

observing scene in three-dimensional fashion.

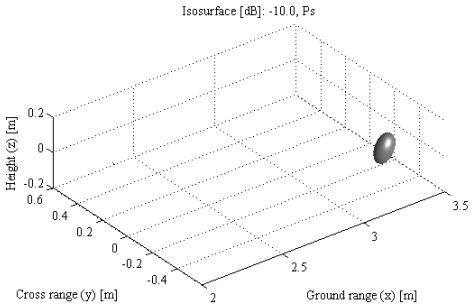

(a) Surface scattering.

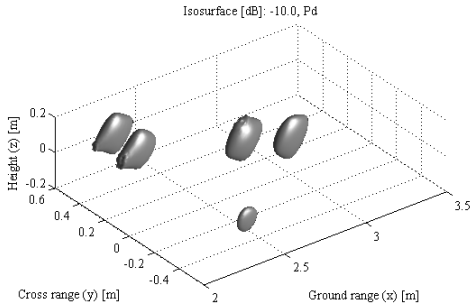

(b) Double-bounce.

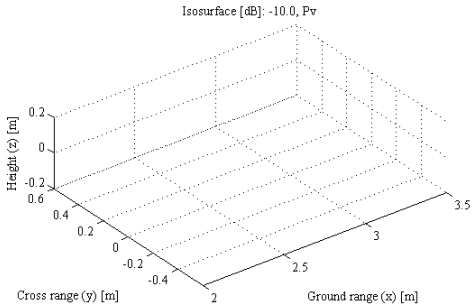

(c) Volume scattering.

Figure 5.12: Three-dimensional polarimetric decomposition (AMBD).

Chapter 6

Circular SAR

Introduction

This chapter is dedicated to the analysis of polarimetric circular SAR (CSAR) image analysis. CSAR is an imaging technique of which the radar trajectory takes a circular form, and the antenna beam illuminates the center of the circular path to acquire the backscattering of targets. Comparing to the conventional SAR systems which have a linear trajectory such as stripmap SAR or spotlight SAR, CSAR has an advantage of being able to image the radar cross section (RCS) of the targets from various azimuthal angles to obtain the high-resolution image.

Once a CSAR image is reconstructed, one can apply several SAR image processing schemes on the image to extract desired information. Theory of radar polarimetry such as polarimetric target decomposition algorithms [10, 5], introduced in Chapter 3, is a potential candidate for this purpose. Although a number of polarimetric decomposition algorithms have been proposed and applied to linear SAR images, only a few researches on the polarimetric characteristics of the CSAR image can be found.

Because CSAR takes advantage of the wide azimuthal angle measurement over full rotation (360°) synthetic aperture, the resultant polarimetric CSAR image is composed of a mixture of the scattering from the targets observed in various polarization basis. This fact makes the polarimetric CSAR image analysis challenging, but gives a new insight in polarimetric radar image analysis simultaneously. To deal with this problem, we propose a novel CSAR image processing method designed to enhance a wire-like target within the spotlighted area via transforming the polarization basis as a function of the slow-time synthetic aperture prior to reconstruct CSAR images.

Outline

This chapter is organized as follows. In Section 6.1, CSAR observation scenario is introduced. Section 6.2 defines the CSAR coordinate system and several quantities used for the CSAR signal modeling and reconstruction. The CSAR signal model and reconstruction algorithms are given in Section 6.3 and 6.5, respectively. We present two CSAR reconstruction algorithm, namely, wavefront reconstruction and direct correlation. In Section 6.6, polarimetric extension of CSAR image is presented, and the effects of polarization basis transformation is discussed. Finally, Section 6.8 concludes the chapter.

6.1 Observation Scenario

The CSAR observation scenario is shown in Figure 6.1. In the CSAR observation, the radar carrying aircraft travels along a circular trajectory to form slow-time synthetic aperture. The antenna beam is maintained so that it points toward the center of the circular trajectory. The observable target area is restricted to the antenna beamwidth or footprint.

In linear SAR systems, reconstructed image depends on the target orientation viewed from the radar, especially for highly-directive targets such as buildings or ships. In addition, the linear SAR image could be subjected to so-called the shadowing effect in which the radar beam could not illuminate the small objects masked by the other larger targets. The CSAR system is able to circumvent these problems, utilizing full-rotation aspect angle measurement.

As discussed in Chapter 3, one can simply extend this observation scenario to the fully polarimetric case. A straightforward extension is achieved by just forming the Sinclair scattering matrix for reconstructed polarimetric CSAR image pixels. However, one should keep in mind that the polarization basis is significantly changed during the data acquisition. For polarimetric CSAR image analysis, we must compensate for this effect to better understand the reconstructed CSAR images. Or one can use small subaperture CSAR data which can be approximated as linear spotlight SAR measurement to ignore the polarization basis variation.

6.2 System Model

The CSAR system geometry is shown in Fig. 6.2. The radar carrying aircraft moves along a circular path of radius R_g to form a slow-time aspect angle (synthetic aperture) θ domain. The antenna main beam is pointed at the center of the circular path during the overall data

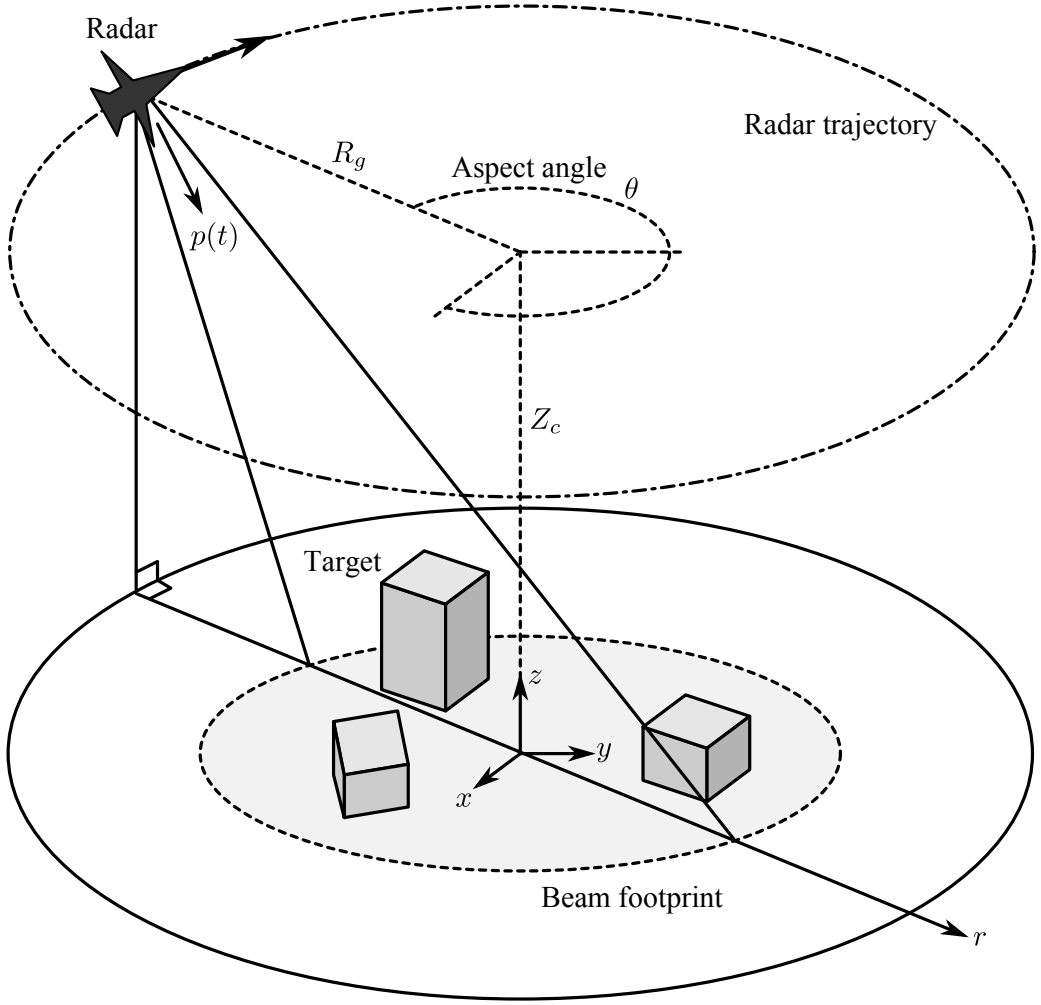

Figure 6.1: CSAR observation scenario.

acquisition. The aircraft altitude is considered to be fixed at $z = Z_c$ in the current discussion. The radar coordinate in the spatial domain can be represented in terms of the slow-time aspect angle variable $\theta \in [0, 2\pi)$ via

$$(x, y, z) = (R_g \cos\theta, R_g \sin\theta, Z_c). \tag{6.1}$$

The slant-range of the scnene center, that is, the distance from the radar to the spatial coordinate $(x, y, z) = (0, 0, 0)$ is written by

$$R_c = \sqrt{R_g^2 + Z_c^2}, \tag{6.2}$$

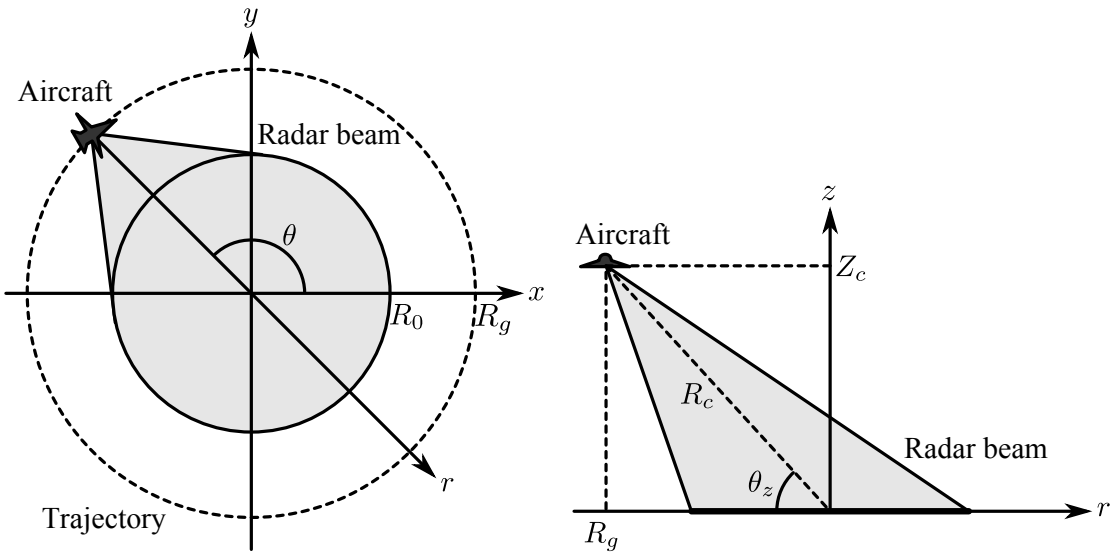

(a) Top view. (b) Side view.

Figure 6.2: CSAR imaging system geometry.

and the slant *depression* or *grazing* angle is defined by

$$\theta_z = \tan^{-1} \frac{Z_c}{R_g}. \tag{6.3}$$

If the antenna beamwidth is ϕ_d, the radius of the spotlighted target area can be described by

$$R_0 = \frac{R_c \tan \phi_d}{\sin \theta_z}. \tag{6.4}$$

Besides this actual spotlighted area, one can arbitrarily select a desired radius for imaging purpose. Also we define the following *along-track target angle* via

$$\theta_x = \sin^{-1} \frac{R_0}{R_g}. \tag{6.5}$$

6.3 Signal Model

The echoed signal model for the CSAR system can be developed in a similar fashion of the linear SAR. We can write the radial distance from the radar to the location (x, y) via

$$r(x, y) = \sqrt{(x - R_g \cos\theta)^2 + (y - R_g \sin\theta)^2 + Z_c}, \tag{6.6}$$

and the corresponding round-trip time via

$$t_r(x,y) = \frac{2r(x,y)}{c}. \tag{6.7}$$

Let $p(t)$ be the transmitted radar signal, where t represent fast-time, and $f(x,y)$ be the continuous reflectivity function at the location (x,y).

$$s(t,\theta) = \int_y \int_x f(x,y) p\left[t - t_r(x,y)\right] dxdy. \tag{6.8}$$

Also a discretized model can be constructed by letting

$$f(x,y) = \sum_n \sigma_n \delta(x - x_n)\delta(y - y_n), \tag{6.9}$$

where σ_n is the reflectivity of the nth point target, and x_n and y_n are the location of this target, respectively. Then plugging Equation (6.9) into Equation (6.8), the signal model becomes

$$s(t,\theta) = \sum_n \sigma_n p\left[t - t_r(x_n,y_n)\right]. \tag{6.10}$$

The continuous signal model of Equation 6.8 is convenient for the subsequent analysis, while the discretized signal model of Equation (6.10) is used for numerical simulations.

The Fourier transform of Equation (6.8) with respect to the fast-time t is

$$\begin{aligned} s(\omega,\theta) &= P(\omega) \int_x \int_y f(x,y) \exp[-j2kr(x,y)] dxdy \\ &= P(\omega) \int_x \int_y f(x,y) g_\theta^*(\omega,x,y) dxdy, \end{aligned} \tag{6.11}$$

where

$$g_\theta = \begin{cases} \exp[j2kr(x,y)], & \text{for } \sqrt{x^2+y^2} \le R_0 \\ 0 & \text{otherwise} \end{cases} \tag{6.12}$$

is called the slant plane Green's function of the CSAR system at the slow-time variable θ and the fast-time frequency ω. As discussed in Chapter 2, the fast-time frequency domain representation of Equation (6.11) is a common signal model for pulsed, FMCW, and stepped frequency radar.

For the FMCW and the stepped frequency radar, one can assume that the following model.

$$P(\omega) = \begin{cases} 1 & \text{for } \omega \in [\omega_c - \omega_0, \omega_c + \omega_0], \\ 0 & \text{otherwise,} \end{cases} \tag{6.13}$$

where ω_c and ω_0 are the center (carrier) frequency and the half size of bandwidth, respectively.

6.4 Fourier Transform of Slant Plane Green's Function

For the matched-filter operation in CSAR image reconstruction, we need the Fourier transform of the slant plane Green's function which is given in Equation (6.12). In this section, we present the result derived in [3, 1].

To begin with, we define the following notational conventions. The rectilinear spatial frequency domain (k_x, k_y) has its polar form representation (ϕ, ρ) as follows:

$$\phi = \tan^{-1} \frac{k_y}{k_x}, \tag{6.14a}$$

$$\rho = \sqrt{k_x^2 + k_y^2}. \tag{6.14b}$$

We denote the two-dimensional Fourier transforms of the target function and the slant plane Green's function with respect to the spatial variable (x, y) by

$$F(k_x, k_y) = \mathcal{F}_{(x,y)}[f(x, y)], \tag{6.15}$$

and

$$G_\theta(\omega, k_x, k_y) = \mathcal{F}_{(x,y)}[g_\theta(\omega, x, y)]. \tag{6.16}$$

The polar coordinate transformation of Equation (6.15) and (6.16) in the spatial frequency domain are defined as

$$F_p(\rho, \phi) = F(k_x, k_y), \tag{6.17}$$

and

$$G_{\theta p}(\omega, \rho, \phi) = G_\theta(\omega, k_x, k_y). \tag{6.18}$$

Using the above notation, one can show that the Green's function in the polar spatial fre-

quency (ρ, ϕ) has the following form [3, 1]:

$$G_{\theta p}(\omega, \rho, \phi) = W_1(\theta - \phi) W_2(\omega, \rho) \exp\left[-j\sqrt{4k^2 - \rho^2} Z_c - j\rho R_g \cos(\theta - \phi)\right], \tag{6.19}$$

where the window functions $W_1(\phi)$ and $W_2(\omega, \rho)$ are defined by

$$W_1(\phi) = \begin{cases} 1 & \text{for } |\phi| \leq \theta_x, \\ 0 & \text{otherwise,} \end{cases} \tag{6.20}$$

and

$$W_2(\omega, \rho) = \begin{cases} 1 & \text{for } |\rho - 2k\cos\theta_z| \leq 2k \sin^2\theta_z \sin\theta_x, \\ 0 & \text{otherwise.} \end{cases} \tag{6.21}$$

6.5 Reconstruction

The CSAR image formation algorithm based on the wavefront reconstruction given in [3, 1] consists of the two steps, namely, the slant plane to *ground plane* transformation and the matched filtering operation for the ground plane CSAR signal. In this section, we firstly present the slant plane to ground plane transformation of CSAR data, and then we develop the ground plane CSAR reconstruction algorithm using matched filtering.

The CSAR signal model of Equation (6.8) can be rewritten using the generalized Parseval's theorem as follows:

$$s(\omega, \theta) = P(\omega) \int_{k_y} \int_{k_x} F(k_x, k_y) G^*_\theta(k_x, k_y, \omega) dk_x \, dk_y. \tag{6.22}$$

The variable transformation of the above Equation (6.22) yields

$$s(\omega, \theta) = P(\omega) \int_{\phi} \int_{\rho} \rho F_p(\rho, \phi) G^*_{\theta p}(\omega, \rho, \phi) d\rho \, d\phi. \tag{6.23}$$

Substituting the Fourier transform of the slant plane Green's function given in Section 6.4, the CSAR signal model of Equation (6.22) can be expressed as the following form:

$$\begin{aligned} s(\omega, \theta) =& P(\omega) \int_{\phi} \int_{\rho} \rho F_p(\rho, \phi) W_1(\theta - \phi) W_2(\omega, \rho) \\ & \cdot \exp\left[-j\sqrt{4k^2 - \rho^2} Z_c - j\rho R_g \cos(\theta - \phi)\right] d\rho \, d\phi. \end{aligned} \tag{6.24}$$

Our objective is to recover $F_p(\rho, \phi)$ from the inversion of the above Equation (6.24).

6.5.1 Slant Plane to Ground Plane Transformation

The first step, the ground plane transformation, is the operation in which slant plane CSAR data is converted to a CSAR data of the target area which is measured at the ground plane (Z_c=0).

For this purpose, we rewire the CSAR signal model in Equation (6.24) as

$$s(\omega, \theta) = \int_{\omega} \Lambda(\omega, \rho) s_g(\rho, \theta) d\omega, \tag{6.25}$$

where

$$\Lambda(\omega, \rho) = P(\omega) W_2(\omega, \rho) \exp\left(-j\sqrt{4k^2 - \rho^2} Z_c\right), \tag{6.26}$$

and

$$s_g(\omega, \theta) = \rho \int_{\phi} F_p(\rho, \phi) W_1(\theta - \phi) \exp\left[-j\rho R_g \cos(\theta - \phi)\right] d\phi. \tag{6.27}$$

The signal $s_g(\omega, \theta)$ is referred to as the ground plane CSAR signal. In fact, the above Equation (6.27) is identical to letting the radar altitude $Z_c = 0$ in the general CSAR signal model given by Equation (6.8).

One can interpret the slant plane CSAR echoed signal in Equation (6.25) result from the transformation of the ground plane CSAR signal by integral kernel defined in Equation (6.26). Thus, the ground plane transformation is the operation in which the measured signal in (6.25) is transformed back to the ground plane CSAR signal of Equation (6.27). Therefore, the slant plane to ground plane transformation is defined via

$$s_g(\omega, \theta) = \int_{\omega} \Lambda^{-1}(\omega, \rho) s(\omega, \theta) d\omega. \tag{6.28}$$

For the digital implementation, the above integral equation is replaced by a matrix product. Let us assume that we have M discrete samples in the fast-time frequency ω domain, that is,

$$\omega_m = \omega_c - \omega_0 + (m-1)\Delta_\omega \quad \text{for } m \in [1, 2, \ldots, M], \tag{6.29}$$

where ω_c, ω_0, and Δ_ω are the center frequency, baseband bandwidth, and sampling interval, respectively. Similarly, assuming that we have N discrete samples in the slow-time θ domain,

these samples are represented by

$$\theta_n = \theta_c - \theta_0 + (n-1)\Delta_\theta \quad \text{for } n \in [1, 2, , \dots N]\,, \tag{6.30}$$

where θ_c, θ_0, and Δ_θ are the center aspect angle, the half width of aspect angle, and slow-time sampling interval, respectively. Using these notation, we can define the following matrices:

$$\boldsymbol{S}_{(\omega,\theta)} = \Big[s(\omega_m, \theta_n)\Big]\,, \tag{6.31a}$$

$$\boldsymbol{\Lambda}_{(\omega,\rho)} = \Big[\Lambda(\omega_m, \rho_n)\Big]\,, \tag{6.31b}$$

$$\boldsymbol{s}_{g(\theta,\rho)} = \Big[s_g(\rho_n, \theta_n)\Big]\,. \tag{6.31c}$$

Using the above matrices, we can express the discretized system model via

$$\boldsymbol{S}_{(\omega,\theta)} = \boldsymbol{\Lambda}_{(\omega,\rho)} \boldsymbol{s}_{g(\theta,\rho)}. \tag{6.32}$$

Thus, our inversion can be done by the following:

$$\boldsymbol{s}_{g(\theta,\rho)} = \boldsymbol{\Lambda}^{-1}_{(\omega,\rho)} \boldsymbol{S}_{(\omega,\theta)}. \tag{6.33}$$

The inverse system kernel $\boldsymbol{\Lambda}^{-1}$ can be computed by pseudo-inverse matrix. However, we can use the following useful approximation to avoid the computation of inverse matrix [3].

$$\boldsymbol{\Lambda}^{-1} \approx \boldsymbol{\Lambda}^{H}, \tag{6.34}$$

where $[\cdot]^H$ represents the conjugate transpose (Hermitian transpose) operation. The slant plane to ground plane conversion is finally expressed via

$$\boldsymbol{s}_{g(\theta,\rho)} = \boldsymbol{\Lambda}^{H}_{(\omega,\rho)} \boldsymbol{S}_{(\omega,\theta)}. \tag{6.35}$$

6.5.2 Ground Plane CSAR Reconstruction

Once the ground plane CSAR signal is derived, one can formulate the matched filtering operation to recover the target function. We begin with the ground plane CSAR signal defined in Equation (6.27) by expressing it as

$$s_g(\omega, \theta) = F_p(\rho, \theta) * s_{g0}(\omega, \theta), \tag{6.36}$$

where the ground plane reference function $s_{g0}(\omega, \theta)$ is

$$s_{g0}(\omega, \theta) = W_1(\theta) \exp(-j\rho R_g \cos\theta). \tag{6.37}$$

We denote the Fourier transform of the polar formatted target function with respect to the slow-time variable θ by

$$F_p(\rho, \xi) = \mathcal{F}_{(\theta)}[F_p(\rho, \theta)], \tag{6.38}$$

where ξ is the Fourier counterpart domain of θ, and Fourier transform of the ground plane CSAR reference signal in Equation (6.37) can be expressed as

$$S_{g0}(\omega, \xi) = \mathcal{F}_{(\theta)}[s_{g0}(\omega, \theta)] \tag{6.39}$$

$$= \begin{cases} H_{\xi}^{(2)}(2kR_g \cos\theta_z) \exp\left(-j\frac{\pi\xi}{2}\right) & \text{for } |\xi| \leq 2kR_0 \cos\theta_z \\ ,0 & \text{otherwise,} \end{cases} \tag{6.40}$$

where $H_{\xi}^{(2)}(\cdot)$ is the Hankel function of the second kind, ξ order. Then, the matched-filter reconstruction is

$$\mathcal{F}_{(\theta)} = \mathcal{F}_{(\theta)}[s_1(\theta, \omega)] H_{\xi}^{(1)}(2kR \cos\theta_z) \exp\left(j\frac{\pi\xi}{2}\right). \tag{6.41}$$

Similar to the linear SAR discussed in Chapter 2, CSAR reconstruction requires spatial frequency interpolation. The concept is illustrated in Figure 6.3, and the mapping is defined via

$$k_x(\theta, \omega) = \rho \cos\theta, \tag{6.42a}$$

$$k_x(\theta, \omega) = \rho \sin\theta. \tag{6.42b}$$

6.5.3 Digital Implementation

Based on the discussion thus far, we can summarize the digital implementation of the CSAR image reconstruction as follows.

Step 1. *As presented in Chapter 2, form the fast-time frequency domain representation of the CSAR received signal.*

Step 2. *Compute the discrete samples of the CSAR system kernel Λ in Equation (6.31b). The result is $M \times N$ matrix, and calculate pseudo-inverse of the system kernel as Equation (6.34).*

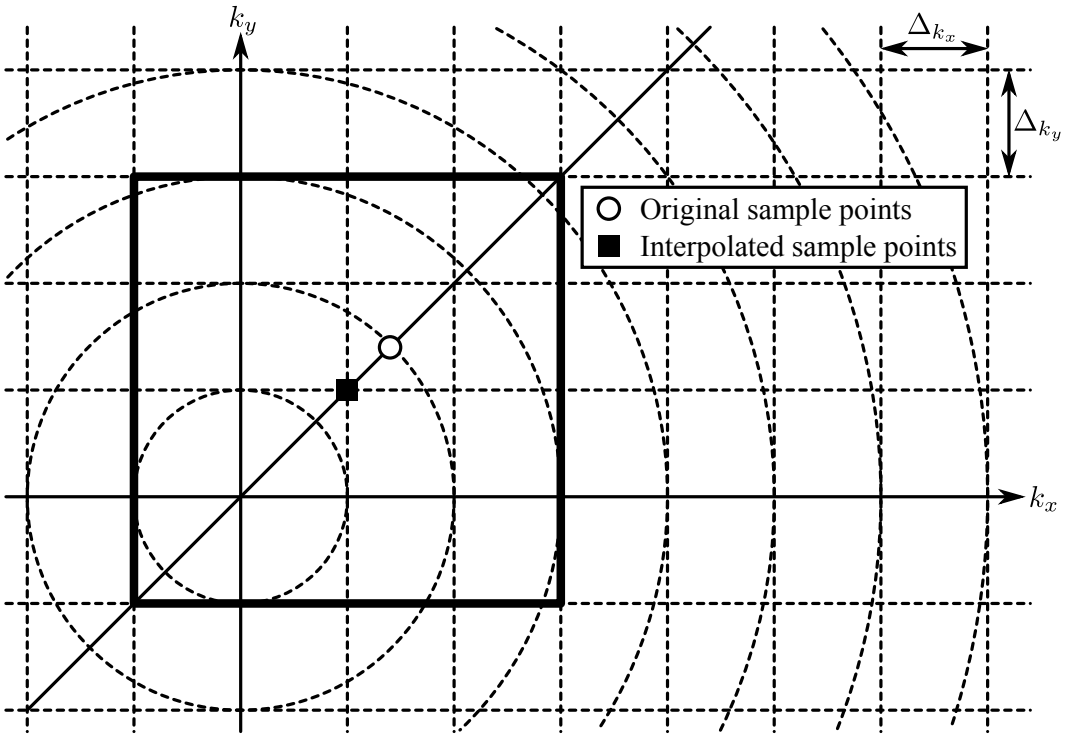

Figure 6.3: CSAR spatial frequency interpolation.

Step 3. *From Equation (6.35), compute* $s_g(\theta, 2k\cos\theta_z)$ *(slant plane to ground-plane transformation).*

Step 4. *Compute the one-dimensional Fourier transform of Equation (6.35) with respect to the slow-time variable* θ*, and perform the matched filtering operation as described in Equation (6.41).*

Step 5. *The inverse Fourier transform produces the polar samples of* $F_p(\rho, \xi)$*, and the two dimensional spatial frequency samples at the rectangular sample points are obtained via interpolation as shown in Figure 6.3.*

Step 6. *The two-dimensional inverse Fourier transform of the resultant samples is the desired target function.*

6.6 Polarimetric CSAR

We have described the polarimetric extension of linear SAR image in Chapter 3 by introducing the Sinclair scattering matrix for each image pixel. The similar extension can be employed for CSAR image, and this section shows the polarimetric model-based decomposition applied for reconstructed CSAR image.

Let $f_{\beta\alpha}(x_i, y_j)$ be the reconstructed CSAR image pixel at the index (x_i, y_j), where $\beta, \alpha \in \{h, v\}$ for lexicographic polarization basis. The Sinclair scattering matrix for this image pixel is defined via

$$\begin{aligned} \boldsymbol{S}_{(h,v)} &= \begin{bmatrix} S_{hh}(x_i, y_j) & S_{hv}(x_i, y_j) \\ S_{vh}(x_i, y_j) & S_{vv}(x_i, y_j) \end{bmatrix} \\ &= \begin{bmatrix} f_{hh}(x_i, y_j) & f_{hv}(x_i, y_j) \\ f_{vh}(x_i, y_j) & f_{vv}(x_i, y_j) \end{bmatrix}. \end{aligned} \tag{6.43}$$

Also we can form the several types of scattering vector or matrices defined in Chapter 3, and the polarimetric decomposition schemes can be applied as well.

Although this polarimetric extension is quite straightforward, however, the resultant decomposed image might differ from the linear SAR results. This is due to the variation of the polarization basis during the data acquisition; as the radar travels along a circular trajectory, the targets could be irradiated from a significantly different aspect angle. It is needless to say that the measured data of linear SAR also experiences the aspect angle variation, but the change of polarization basis can be considered as negligibly small.

6.6.1 Polarization Basis Transformation

Appearance of an Oriented Wire

We consider a simple polarization basis transformation to take the variation of polarization basis during the acquisition into account. Let us assume that a thin oriented wire is located at the center of the circular trajectory of CSAR as shown in Fig. 6.4. The wire orientation is described by the two angular parameters (ϕ_w, ψ_w). However, the wire orientation angle which only we can observe is the orientation angle γ_w in the (h, v) polarization plane that is perpendicular to the line of sight (i.e. n-direction). Apparently, the orientation angle γ is a function of the slow-time variable θ.

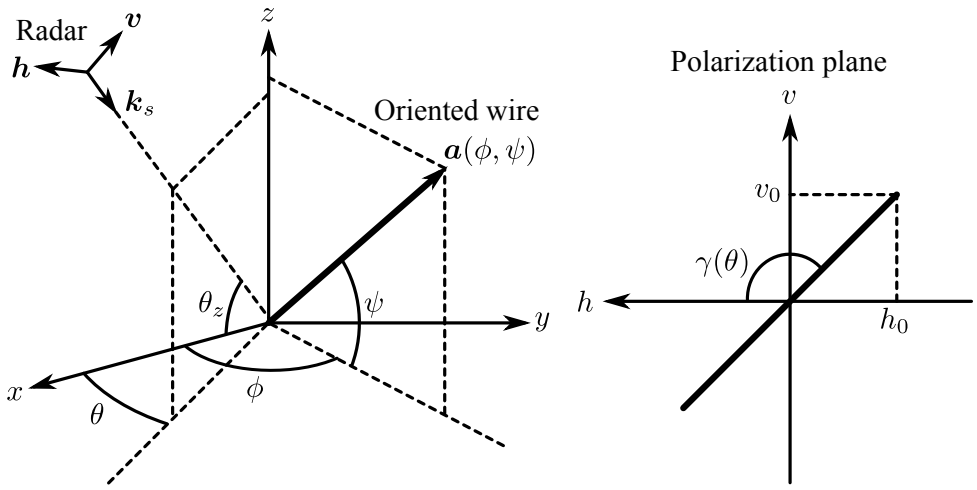

(a) Oriented wire.

(b) Wire orientation viewed in polarization plane.

Figure 6.4: An oriented wire located at the center of the circular trajectory, and the appearance of the orientation in the (h, v) basis polarization plane.

To show this, let $\boldsymbol{a}(\phi, \psi)$ be the unit vector along the oriented wire, that is,

$$\boldsymbol{a}(\phi_w, \psi_w) = \begin{bmatrix} \cos\psi_w \cos\phi_w & \cos\psi_w \sin\phi_w & \sin\psi_w \end{bmatrix}^T, \tag{6.44}$$

where $[\cdot]^T$ is the vector or matrix transpose operation. The transformation of the vector $\boldsymbol{a}(\phi, \psi)$ within the global (x, y, z) coordinate system into the local (n, h, v) coordinate system is expressed as

$$\begin{bmatrix} n \\ h \\ v \end{bmatrix} = \begin{bmatrix} \cos\theta_z & 0 & -\sin\theta_z \\ 0 & 1 & 0 \\ \sin\theta_z & 0 & \cos\theta_z \end{bmatrix} \begin{bmatrix} \cos\theta & -\sin\theta & 0 \\ \sin\theta & -\cos\theta & 0 \\ 0 & 0 & 1 \end{bmatrix} \boldsymbol{a}(\phi_w, \psi_w). \tag{6.45}$$

Then, the wire orientation in the (h, v) polatization plane can be calculated by

$$\gamma_w(\theta) = \mathrm{Tan}^{-1}(v, h), \tag{6.46}$$

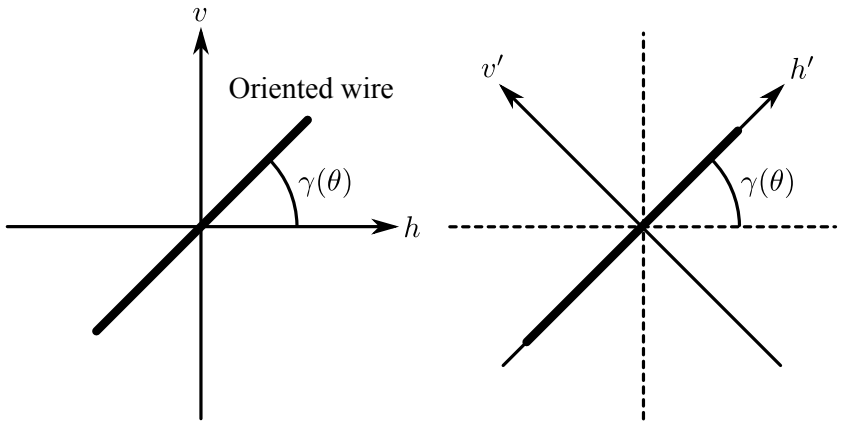

(a) Original (h, v) basis. (b) γ-rotated linear (h', v') basis.

Figure 6.5: Original (h, v) basis and γ-rotated linear (h', v') basis. Clearly, h'-polarized scattering is dominant in this situation.

where the function $\mathrm{Tan}^{-1}(v, h)$ is the four-quadrant inverse tangent defined as

$$\mathrm{Tan}^{-1}(v,h) = \begin{cases} \tan^{-1}\frac{v}{h} & \text{for} \quad h > 0, \\ \tan^{-1}\frac{v}{h} + \pi & \text{for} \quad v \geq 0,\ h < 0, \\ \tan^{-1}\frac{v}{h} - \pi & \text{for} \quad v < 0,\ h < 0, \\ +\frac{\pi}{2} & \text{for} \quad v > 0,\ h = 0, \\ -\frac{\pi}{2} & \text{for} \quad v < 0,\ h = 0, \\ 0 & \text{for} \quad v = 0,\ h = 0. \end{cases} \tag{6.47}$$

Polarization Basis Transformation

We use the angle $\gamma(\theta)$ to enhance the scattering from a wire which has a specific orientation (ϕ, ψ). At a fixed slow-time variable θ, the wire is appeared to be oriented within the (h, v) polarization plane as shown in Figure 6.5 (a). To enhance the reflection from this oriented wire, the original (h, v) polarization basis should be rotated around the line of sight (i.e. n-axis) by the angle $\gamma(\theta)$ as shown in Figure 6.5 (b). We refer to the rotated linear polarization basis as the linear (h', v') basis that is a function of the slow-time variable θ. In this situation, the v'-polarized scattering could be dominant. In other words, we can *intensify* the scattering from the oriented wire by this polarization basis transformation.

To do this, we consider the scattering matrix for the polarimetric CSAR received signal (i.e.

NOT for the reconstructed image) in the time domain representation as

$$\boldsymbol{s}(t,\theta) = \begin{bmatrix} s_{hh}(t,\theta) & s_{hv}(t,\theta) \\ s_{vh}(t,\theta) & s_{vv}(t,\theta) \end{bmatrix}. \tag{6.48}$$

The generic form of polarization basis transformation is given in Chapter 3 and [12]. Only we need here is the rotation of the linear (h,v) basis into the rotated linear (h',v') basis. Thus, the rotation of the scattering matrix $\boldsymbol{s}(t,\theta)$ by the angle $\gamma(\theta)$ can be expressed as

$$\begin{aligned} \boldsymbol{s}_R(\gamma;t,\theta) &= \begin{bmatrix} s_{h'h'}(t,\theta) & s_{h'v'}(t,\theta) \\ s_{v'h'}(t,\theta) & s_{v'v'}(t,\theta) \end{bmatrix} \\ &= \boldsymbol{R}(\gamma)\boldsymbol{s}(t,\theta)\boldsymbol{R}(\gamma)^T, \end{aligned} \tag{6.49}$$

with the rotation matrix $\boldsymbol{R}(\gamma)$ defined via

$$\boldsymbol{R}(\gamma) = \begin{bmatrix} \cos\gamma & -\sin\gamma \\ \sin\gamma & \cos\gamma \end{bmatrix}. \tag{6.50}$$

After making the rotated polarimetric CSAR signal $\boldsymbol{s}_R(\gamma;t,\theta)$ for all the available slow-time variable θ, the CSAR image reconstruction algorithm (e.g. wavefront reconstruction, backprojection, or DCA) can be used for each polarization channel $s_{\beta'\alpha'}(t,\theta)$ where $\alpha',\beta' \in \{h',v'\}$ to form the basis transformed CSAR image. We refer to this preprocessing as the *wire structure intensifier* (WSI).

The CSAR reconstruction algorithm with WSI preprocessing can be summarized as the following steps.

Step 1. *Specify the wire direction to be intensified by selecting the angular parameters* (ϕ,ψ).

Step 2. *For a fixed slow-time variable* θ*, compute the orientation angle* $\gamma(\theta)$.

Step 3. *Transform the CSAR received signal in the* (h,v) *linear polarization basis* $\boldsymbol{s}(t,\theta)$ *into* γ*-oriented linear* (h',v') *basis to derive* $\boldsymbol{s}_R(\gamma;t,\theta)$.

Step 4. *Reconstruct the CSAR target function in the spatial* (x,y) *domain from the basis-transformed signal* $s_{\beta'\alpha'}(t,\theta)$ *using the CSAR reconstruction algorithm (e.g. wavefront reconstruction, backprojection, or DCA). The wavefront reconstruction algorithm is used in this paper.*

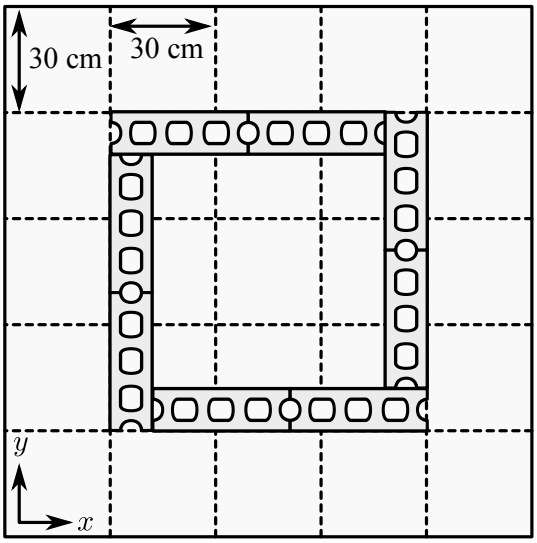

Figure 6.6: Building wall model.

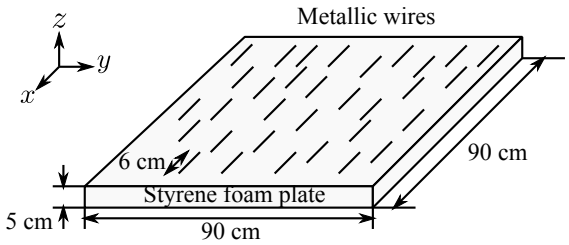

Figure 6.7: Distributed wire model.

6.7 Experimental Validation

We conduct X-band indoor CSAR experiments in an anechoic chamber to validate the effects of WSI preprocessing. The detail of the CSAR measurement system is given in Chapter 2.

6.7.1 Targets

In addition to the building model which is described in Chapter 2, we employ the other targets shown in Figure 6.6 and 6.7 are used to examine the effect of WSI preprocessing. Figure 6.6 is the building (man-made structure) model composed of a concrete ground plate and blocks. The center of the ground plate is adjusted to the center of the circular path. The dominant scattering from the building walls and edges is expected to be observed.

The another target, a distributed wire model, is depicted in Fig. 6.7. The wire diameter is 2 mm. This can be considered as a simple model of the vegetation components such as stems or

twigs. Positions of these wires are determined by computer-generated uniform random numbers. However, all the wire orientation angles are adjusted to be along the spatial x-axis. To enhance the scattering from these wires, WSI preprocessing should be imposed on the received CSAR signal $S_{\beta\alpha}(\omega, \theta)$ with the angular parameters $(\phi, \psi) = (0^\circ, 0^\circ)$.

Figure 6.8 (a) shows the reconstructed CSAR images in the original linear (h, v) basis for the building model. In this figure, the dominant scattering from the building walls and edges appears in the hh-polarized image. The intensity of the vv-polarized image is much weaker than that of the hh-polarized image. As mentioned in Chapter 4, when one observes a pair of orthogonal dielectric surfaces at vv-polarization, there exists the Brewster angle at which the vertically polarized reflection approaches to zero. Therefore, the weak vv-polarized reflection can be interpreted as the Brewster angle effect caused in the double-bounce interaction between the ground surface and the building walls.

Figure 6.8 (b) is the basis transformed image using WSI preprocessing for the same building model. To enhance the building walls or edges which are parallel to the spatial x-axis, we choose the angular parameters $(\phi, \psi) = (0^\circ, 0^\circ)$ (see Fig. 6.4). As it is expected, the building walls which are parallel to the x-axis are clearly shown in the $h'h'$-polarized image. Also we can observe that the building walls which are perpendicular to the x-axis are appeared in the $v'v'$-polarized image. Hence, WSI preprocessing can potentially be used to decompose the building walls facing toward the different directions. This is the unique feature of the CSAR image reconstruction with WSI preprocessing.

The similar images for the distributed wire target can be found in Fig. 6.9. Comparing to the hh-polarized image and the vv-polarized image in Fig. 6.9 (a), the hh image intensity is stronger than the vv intensity. The reason for this difference can be described by the effective length of the metallic wires viewed from the polarization planes. Except for the extreme case of the depression angle $\theta_z = 90^\circ$, the effective length of the wire becomes shorter than the actual wire length as the depression angle decreases. In the worst situation that $\theta_z = 0^\circ$ (i.e. the ground plane CSAR measurement), the scattering from the distributed wires positioned horizontally to the (x, y) plane like this experiment can not be observed at the vv-polarized channel.

The wire enhanced images are shown in Fig. 6.9 (b). Similar to the previous analysis for the building model, the distributed wires which are parallel to the x-axis are intensified and appeared as the $h'h'$-polarized image. Apart from the building model, the wires which are perpendicular to the x-axis does not exist in this wire model. Therefore, the $v'v'$-polarized image shows weaker intensity than that of the $h'h'$-polarized image.

Figure 6.8 shows the similar result for building model described in Chapter 2. The building wall paralleled x-axis are intensified as the $h'h'$-polarized image.

6.8 Summary of This Chapter

In this chapter, an analysis for the fully polarimetric CSAR images is given. Although CSAR provides the high-resolution image of the targets, however, conventional polarimetric analysis might not be directory applied on the CSAR image due to the diversity of the slow-time aspect (azimuthal) angle. To incorporate the variation of the polarization basis in the CSAR measurements, a preprocessing scheme called wire structure intensifier (WSI) is proposed.

We conduct the laboratory experiments using the simple man-made structure model and the distributed wire model, and it has shown by the laboratory experiments that the proposed method can successfully intensify the desired wire or edge structure of the targets.

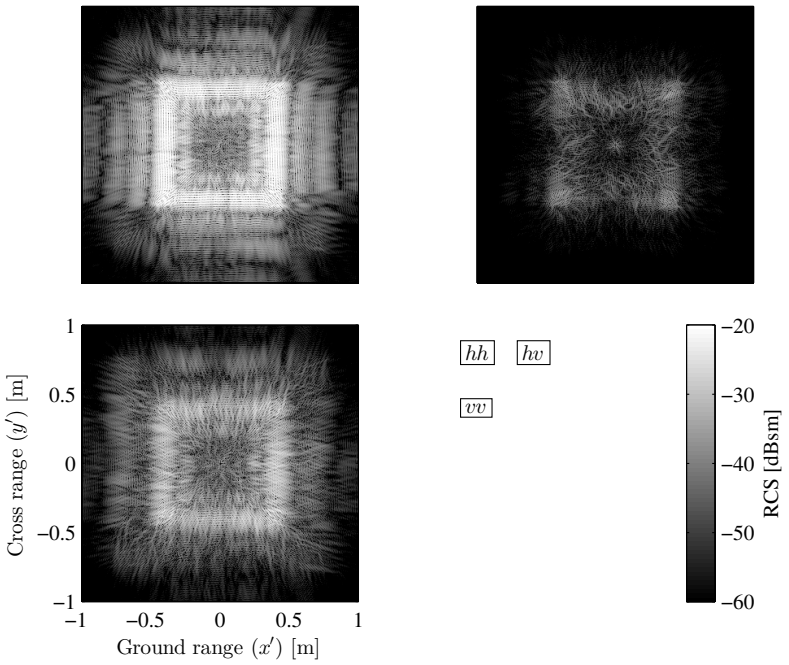

(a) Original linear (h, v) basis images.

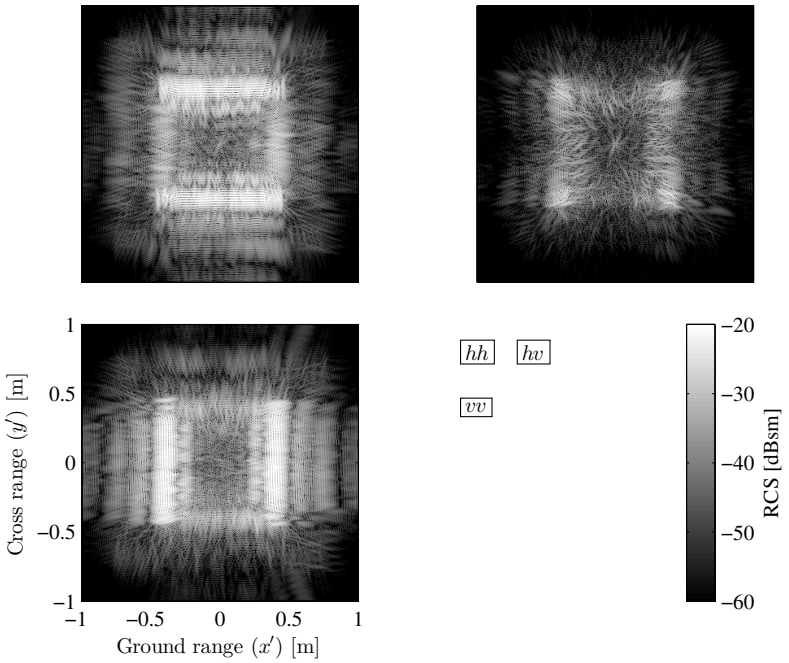

(b) Transformed linear $(h'v')$ basis images with the angular parameters $(\phi, \psi) = (0°, 0°)$.

Figure 6.8: Reconstructed CSAR target functions for the building wall model at each polarization channel.

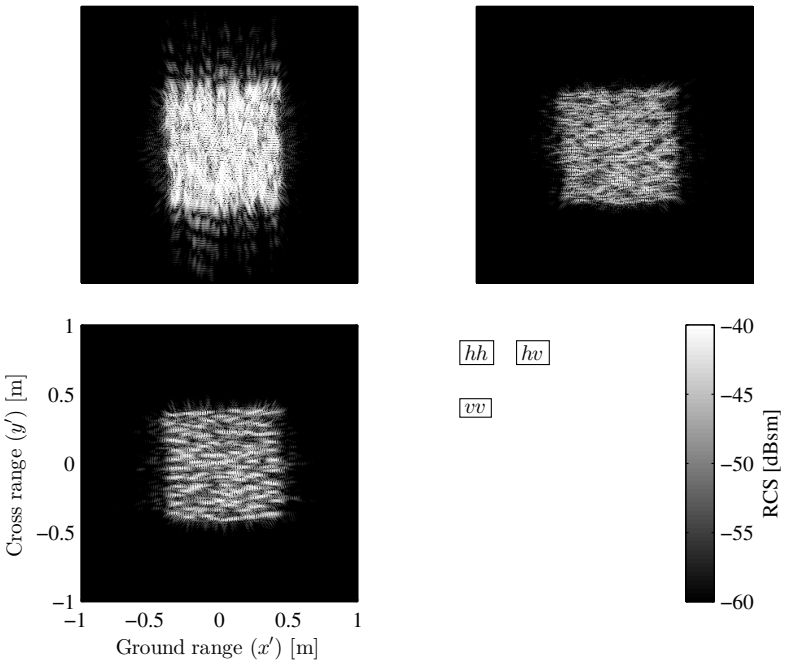

(a) Original linear (h, v) basis images.

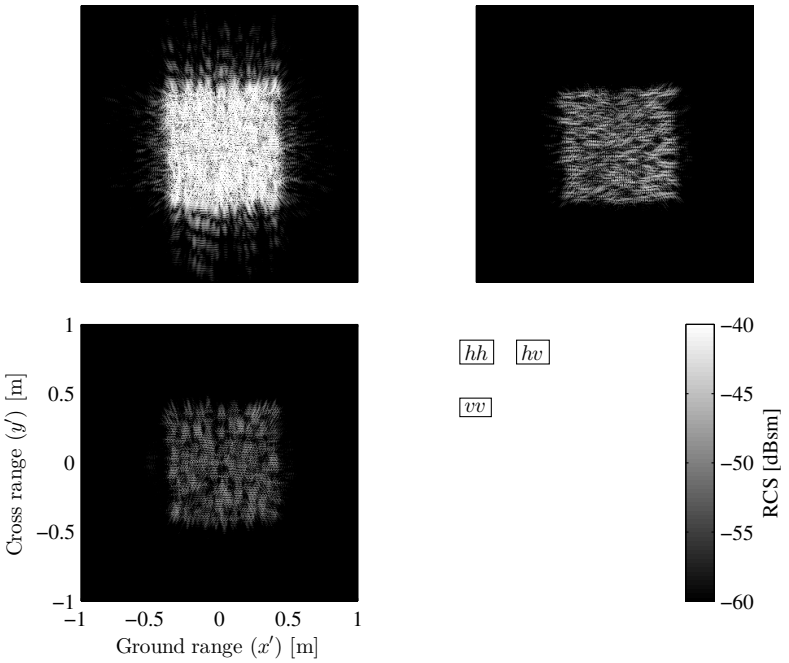

(b) Transformed linear $(h'v')$ basis images with the angular parameters $(\phi, \psi) = (0°, 0°)$.

Figure 6.9: Reconstructed CSAR target functions for the distributed wire model at each polarization channel.

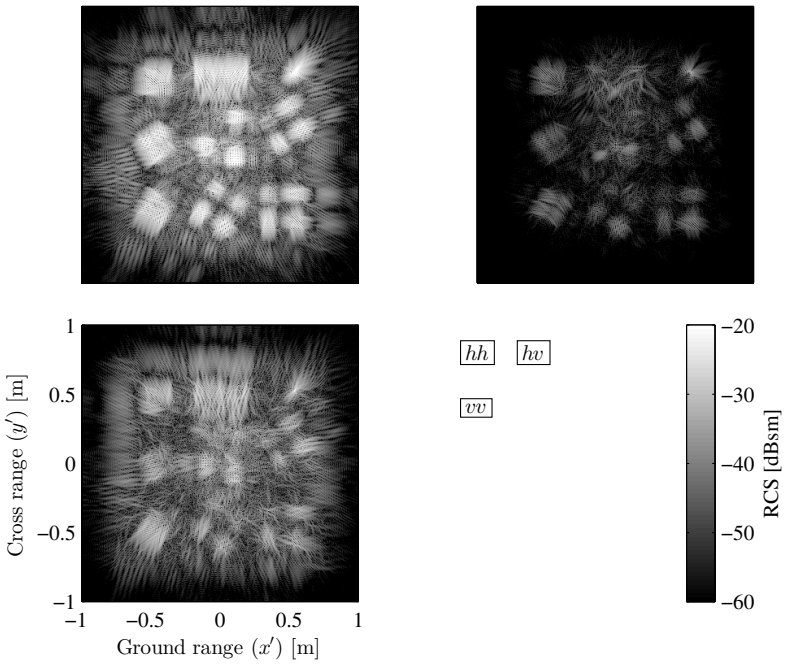

(a) Original linear (h, v) basis images.

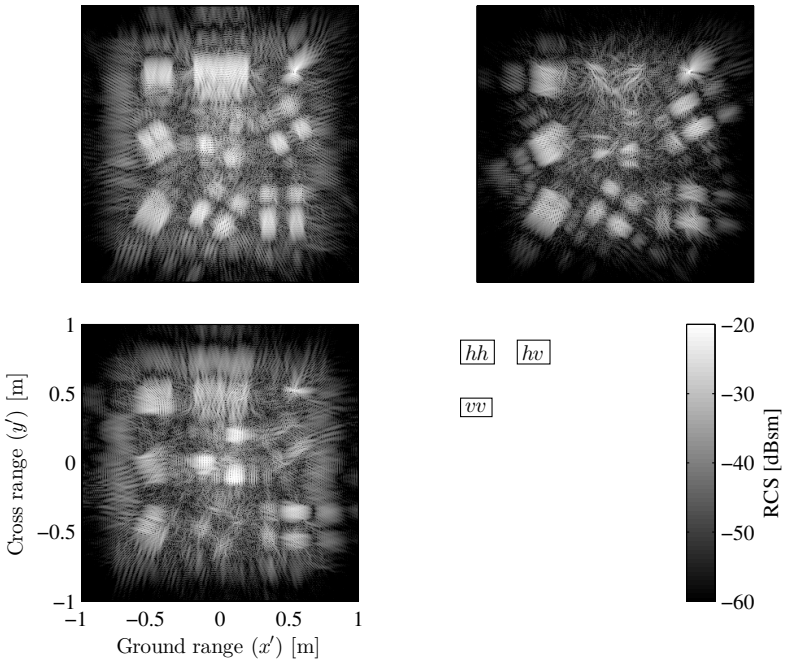

(b) Transformed linear $(h'v')$ basis images with the angular parameters $(\phi, \psi) = (0°, 0°)$.

Figure 6.10: Reconstructed CSAR target functions for the building model at each polarization channel.

Chapter 7

Conclusion and Suggestion

This thesis presented the analysis of multi angle synthetic aperture radar image. The multi angular observation reveals new insight to understand the observed scene which is unavailable in the single angle SAR image.

In Chapter 3, we compared model-based polarimetric decomposition algorithms qualitatively by using anechoic chamber measurement data. It has shown that the AMBD produces different decomposition result when one observes forested terrain. Chapter 4 extended conventional PolSAR images to the multiple angle observation, and it has shown that the co-polarization ratio can be used to estimate moisture condition of forested terrain. Chapter 5 described the basic concepts of TomoSAR three-dimensional reconstruction, and polarimetric decomposition algorithms described in Chapter 3 is used to recover three-dimensional scattering mechanisms of the observing targets. Finally in Chapter 6, polarimetric CSAR analysis is presented, and it has shown that the polarimetric basis transformation plays an important role to deal with the polarimetric CSAR image reconstruction and analysis.

For further analysis, the result presented in this thesis should be validated by airborne or spaceborne radar images.

Bibliography

[1] M. Soumekh, *Synthetic Aperture Radar Signal Processing with MATLAB Algorithms*, John Wiley & Sons, Inc., 1999.

[2] M. Soumekh, *Fourier Array Imaging*, Prentice-Hall, Inc., 1994.

[3] M. Soumekh, "Reconnaissance with slant plane circular SAR imaging," IEEE Transactions on Image Processing, vol. 5, no. 8, Aug. 1996.

[4] A. Papoulis, *Signal Analysis*, Mcgraw-Hill College, May 1977.

[5] A. Freeman and S. L. Durden, "A three-component scattering model for polarimetric SAR data ," IEEE Transactions on Geoscience and Remote Sensing, vol. 36, no. 3, pp. 963–973, May 1998.

[6] Y. Yamaguchi, "Four-Component Scattering Power Decomposition With Rotation of Coherency Matrix," IEEE Transactions on Geoscience and Remote Sensing, vol. 49, no. 6, pp. 2251–2258, June 2011.

[7] F. Xu and Y. Q. Jin, "Deorientation theory of polarimetric scattering targets and application to terrain surface classification," IEEE Transactions on Geoscience and Remote Sensing, vol. 43, no. 10.

[8] T. Watanabe, H. Yamada, R. Sato, and Y. Yamaguchi, "Preliminary Results of Polarimetric Circular SAR Image Analysis," IEICE Tech. Rep., vol. 114, no. 397, SANE2014-106, pp. 7-11, Jan. 2015.

[9] R. Stolt, "Migration by Fourier transform," Geophysics, vol. 43, no. 1, pp. 23–48, 1978.

[10] S. Cloude and E. Pottier, "A review of target decomposition theorems in radar polarimetry," IEEE Transactions on Geoscience and Remote Sensing, vol. 34, no. 2, pp. 498–518, Mar 1996.

[11] R. K. Raney, "A Free 3-dB in Cross-Polarized SAR Data," IEEE Transactions on Geoscience and Remote Sensing, vol. 26, pp.700–702, 1988.

[12] A. P. Agrawal, and W.-M Boerner, "Redevelopment of Kennaugh Target Characteristic Polarization State Theory Using the Polarization Transformation Ratio for the Coherent Case," IEEE Transaction on Geoscience and Remote Sensing, vol. GE-27, pp. 2–14, 1989.

[13] J. van Zyl, Y. Kim, Synthetic Aperture Radar Polarimetry, John Wiley & Sons, Inc., 2011.

[14] D. Entekhabi, E.G. Njoku, P.E. O'Neill, K.H. Kellogg, W.T. Crow, W.N. Edelstein, J.K. Entin, S.D. Goodman, T.J. Jackson, J. Johnson, J. Kimball, J.R. Piepmeier, R.D. Koster, N. Martin, K.C. McDonald, M. Moghaddam, S. Moran, R. Reichle, J. Shi, M.W. Spencer, S.W. Thurman, L. Tsang, and J.J. van Zyl, "The soil moisture active passive (SMAP) mission," Proc. IEEE, vol. 98, no. 5, pp. 704–716, May 2010.

[15] P. Silvestrin, M. Berger, Y.H. Kerr, and J. Font, "ESA's second earth explorer opportunity mission: the soil moisture and ocean salinity mission — SMOS," IEEE Geosci. Remote Sensing Newslett., vol. 118, pp. 11–14, Mar. 2001.

[16] D. Entekhabi, E.G. Njoku, P. Houser, M. Spencer, T. Doiron, Y. Kim, J. Smith, R. Girard, S. Belair, W. Crow, T.J. Jackson, Y.H. Kerr, J.S. Kimball, R. Koster, K.C. McDonald, P.E. O'Neill, T. Pultz, S.W. Running, J. Shi, E. Wood, and J.J. van Zyl, "The hydrosphere state (Hydros) satellite mission: an earth system pathfinder for global mapping of soil moisture and land freeze/thaw," IEEE Trans. Geosci. Remote Sens., vol. 42, no. 10, pp. 2184–2195, Oct. 2004.

[17] J.R. Wang, E.T. Engmen, J.C. Shiue, M. Rusek and C. Steinmeier, "The SIR-B observations of microwave backscatter dependence on soil moisture, surface roughness, and vegetation covers," IEEE Trans. Geosci. Remote Sens., vol. GE-24, no. 4, pp. 510–516, July 1986.

[18] M.C. Dobson and F.T. Ulaby, "Preliminary evaluation of the SIR-B response to soil moisture, surface roughness, and crop canopy cover," IEEE Trans. Geosci. Remote Sens., vol. GE-24, no. 4, pp. 517–526, July 1986.

[19] K. Schneider and N. Oppelt, "The determination of mesoscale soil moisture patterns with ERS data," Proc. 1998 IEEE International Geoscience and Remote Sensing Symposium (IGARSS1998), vol. 4, pp. 1831–1833, July 1998.

[20] A.S. Quesney, S. Le Hégarat-Mascle, O. Taconet, D. Vidal-Madjar, J.P. Wigneron, C. Loumagne, and M. Normand, "Estimation of watershed soil moisture index from ERS/SAR data," Remote Sensing of the Environment, vol. 72, no. 3, pp. 290–303, June 2000.

[21] P.C. Dubois, J.J. van Zyl, and T. Engman, "Measuring soil moisture with imaging radars," IEEE Trans. Geosci. Remote Sens., vol. 33, no. 4, pp. 915–926, July 1995.

[22] J. Shi, J. Wang, A.Y. Hsu, P.E. O'Neill, and E.T. Engman, "Estimation of bare surface soil moisture and surface roughness parameters using L-Band SAR image data," IEEE Trans. Geosci. Remote Sens., vol. 35, no. 5, pp. 1254–1266, Sep. 1997.

[23] Y. Oh, K. Sarabandi, and F.T. Ulaby, "An empirical model and an inversion technique for radar scattering from bare soil surfaces," IEEE Trans. Geosci. Remote Sens., vol. 30, no. 2, pp. 370–381, Mar. 1992.

[24] Food and Agriculture Organization of the United Nations (FAO), "Global forest resources assessment 2010," FAO Forestry Paper 163, Rome, 2010.

[25] R.T. Watson, I. R.Noble, B. Bolin, N.H. Ravindranath, D.J. Verardo, and D.J. Dokken, Land use, land-use change and forestry, Cambridge University Press, Cambridge, UK, 2000.

[26] E. Ezcurra, Global desserts outlook, Division of Early Warning and Assessment (DEWA), United Nations Environment Programme (UNEP), Nairobi, Kenya, 2006.

[27] M. Arii, "Retrieval of soil moisture under vegetation using polarimetric radar," Ph.D. dissertation California Institute of Technology, Pasadena, CA, pp. 68–101, May 2009.

[28] S.L. Durden, J.J. van Zyl, and H.A. Zebker, "Modeling and observation of the radar polarization signature of forested areas," IEEE Trans. Geosci. Remote Sens., vol. 27, no. 3, pp. 290–301, May 1989.

[29] F.T. Ulaby, K. Sarabandi, K. McDonald, M. Whitt, and M.C. Dobson, "Michigan microwave canopy scattering model (MIMICS)," Univ. Michigan, Ann Arbor, Tech. Rep. 022486-T-1, July 1988.

[30] F. Ulaby, R. Moore, and A. K. Fung, "Microwave Remote Sensing: Active and Passive," Norwood, MA: Artech House, 1982.

[31] L. Brocca, T. Moramarco, F. Melone, W. Wagner, S. Hasenauer, and S. Hahn, "Assimilation of surface- and root-zone ASCAT soil moisture products into rainfall-runoff modeling," IEEE Trans. Geosci. Remote Sens., vol. 50, no. 7, pp. 2542–2555, July 2012.

[32] M. Moghaddam and S. Saatchi, "Analysis of scattering mechanisms in SAR imagery over boreal forest: results from BOREAS'93," IEEE Trans. Geosci. Remote Sens., vol. 33, no. 5, pp. 1290–1296, Sep. 1995.

[33] F. T. Ulaby and M. A. El-Rayes, "Microwave Dielectric Spectrum of Vegetation – Part II: Dual-Dispersion Model," IEEE Trans. Geosci. Remote Sensing, vol. GE-25, no. 5, Sep. 1987.

[34] M. T. Hallikainen, F. T. Ulaby, M. C. Dobson, M. A. El-Rayes, and L. Wu, "Microwave Dielectric Behavior of Wet Soil–Part I: Empirical Models and Experimental Observations," IEEE Trans. Geosci. Remote Sensing, vol. 23, pp. 25–34, 1985.

[35] W. Wagner, G. Lemoine, M. Borgeaud, and H Rott, "A study of vegetation cover effects on ERS scatterometer data," IEEE Trans. Geosci. Remote Sens., vol. 37, no. 2, pp. 938–948, Mar. 1999.

[36] Y.-C. Lin and K. Sarabandi, "Electromagnetic scattering model for a tree trunk above a tilted ground plane," IEEE Trans. Geosci. Remote Sens., vol. 33, no. 4, pp. 1063–1070, July 1995.

[37] M. Arii, T. Watanabe, and H. Yamada, "Sensitivity study of radar backscatter from boreal forest using discrete scatterer model," Proc. 2012 IEEE International Geoscience and Remote Sensing Symposium (IGARSS2012), pp. 1425–1428, July 2012.

[38] Y. Okada, T. Hamasaki, M. Tsuji, M. Iwamoto, K. Hariu, Y. Kankaku, S. Suzuki, and Y. Osawa, "Hardware performance of L-band SAR system onboard ALOS-2," Proc. 2011 IEEE International Geoscience and Remote Sensing Symposium (IGARSS2011), pp. 894–897, July 2011.

[39] S. R. Cloude and K. P. Papathanassiou, "Polarimetric SAR interferometry," IEEE Trans. Geosci. Remote Sensing, vol. 23, pp. 25–34, 1985.